In-situ Grain Scale Strain Measurements using Digital Image Correlation

A Thesis

Submitted to the Faculty

of

Drexel University

by

Raghavendra Nataraj Saralaya

in partial fulfillment of the

requirements for the degree

of

Master of Science in Mechanical Engineering

June 2012

DEDICATIONS

ಈ ಪ್ರಮೇಯವನ್ನು ನನ್ನ ತಾಯಿ ಸುಮಿತ್ರರವರಿಗೆ, ತಂದೆ ನಟರಾಜ್ರವರಿಗೆ ಹಾಗು ಅನುಜ ಕ್ಷಿತೀಶನಿಗೆ ಅರ್ಪಿಸುತ್ತೇನೆ.

ACKNOWLEDGEMENTS

First and foremost, I would like to express the deepest of my gratitude to Dr. Antonios Kontsos for his patience and consistent motivation. He has been my mentor and guide for most part of my life at Drexel University, and is a person who I look up to in times of need and otherwise. Without his insight and timely guidance, I would be very lost in many aspects. Mere words are not sufficient to express my gratitude to him.

My life at Drexel University would not have possible without the unwavering emotional and financial support from my parents Sumithra K. and father Nataraj Saralaya. Thank you for mustering the courage to let me pick my path. Both of you are a blessing to me.

Eric Schwartz has been my Digital Image Correlation mentor. A good teacher and a better friend, his Digital Image Correlation lessons helped me build the foundations I needed to write this thesis. Kavan Hazeli has been like my elder brother. Without his invaluable help, none of the experiments mentioned in this thesis would have been possible. Prashanth Abraham has been a good friend and his words of wisdom are always helpful. I also thank Jefferson Cuadra, whose coding skills and common sense has been of immense help throughout the time of experimentation and putting together my thesis.

TABLE OF CONTENTS

LIST OF TABLES ..... **VIII**

LIST OF FIGURES ..... **IX**

ABSTRACT ..... **XIII**

CHAPTER 1: INTRODUCTION **1**

1.1 MOTIVATION 1

Fracture Mechanics *2*

Crystal Plasticity *3*

1.2 WHY DIGITAL IMAGE CORRELATION? 3

1.3 THESIS ARRANGEMENT 5

CHAPTER 2: DIGITAL IMAGE CORRELATION **6**

2.1 INTRODUCTION 6

2.2 DEVELOPMENT OF DIC 6

2.3 THEORY 8

2.3.1 2D Continuum Mechanics *8*

2.3.2 In-plane Displacement Mapping Estimation by Image Correlation *10*

2.3.3 3D Image Correlation *19*

2.4 EQUIPMENT & PROCEDURE 22

Hardware Components and Parameters *22*

Cameras 23

Lenses 24

Other Hardware Components *26*

Illumination: 26

Polarizers & Filters: 27

Camera Support: 27

Specimen Preparation *27*

What is a good surface pattern? 27

2.5 DIC Algorithms 31

2.5.1 Surface Patterning Methods 32

Macro Scale Methods 32

Micro Scale Methods 32

2.5.2 Displacement Mapping and Strain Calculations 33

Subset based displacement algorithms 33

Continuum based displacement mapping 42

A Discussion 45

CHAPTER 3: STRAIN HETEROGENETIES IN POLYCRYSTALLINE METALS 49

3.1 Approaches 49

Interferometry Methods 49

Speckle and Holographic Interferometry: 50

Moiré Interferometry 52

Discussion on Interferometric Methods 55

Diffraction Methods 55

X-Ray Diffraction 55

Neutron Diffraction 57

Electron Backscattered Diffraction 59

Discussion on diffraction methods 62

Photogrammetry Methods 63

Grid Methods 63

3.2 DIC in Polycrystalline Material Grain Strain 64

Surface Contrast 65

In-situ Versus Ex-situ 67

Grain Orientation Matching 68

CHAPTER 4: *IN-SITU* GRAIN–STRAIN MEASUREMENT OF MAGNESIUM ALLOY 69

4.1 Motivation 69

4.2 Feasibility Study 69

Sample Preparation: *69*

50 mm lenses with extension tubes: *70*

Setup and Image Acquisition *71*

4.3 Discussion and Conclusions 75

CHAPTER 5: *IN-SITU* GRAIN STRAIN MEASUREMENTS NEAR THE FRACTURE ZONE OF AN ALUMINUM ALLOY 76

5.1 Overview and Lens Considerations 76

Lens Considerations *76*

Lens Selection *77*

5.2 Experimental Procedure 78

Specimen preparation *78*

DIC Parameters *79*

Practical Considerations *80*

Loading Setup *82*

5.3 Results 83

Evolution of Strains *85*

Displacement in loading direction: *86*

Crack Opening Displacement vs. Load *87*

5.6 Discussion & Conclusions 88

Strain Heterogeneities: *88*

Comparison with macroscale DIC *90*

CHAPTER 6: SEM DIC 91

6.1 In-situ SEM testing motivation 91

6.2 Background and Development 92

6.3 Equipment Setup 93

Scanning Electron Microscope *93*

calibration: 95

Surface patterning:..... 95

MEMS loading device..... *95*

Loading and Image acquisition..... *96*

6.4 APPROACH IN THIS WORK..... 96

6.5 EX-SITU APPLICATION OF DIC..... 97

6.6 RESULTS..... 98

6.5 DISCUSSION..... 99

CHAPTER 7: CONCLUSIONS AND FUTURE WORK..... 101

LIST OF REFERENCES..... 103

LIST OF TABLES

Table 1: Salient developments in methods of DIC [10] 7

Table 2: PQ Coordinates 9

Table 3: Parameters to be estimated during camera calibration 21

Table 4: Steps in Calibration using a patterned calibration artifact [24] 30

Table 5: Displacement variables to be optimized in correlation process 34

Table 6: A study of effect of subset size on the strain noise 46

Table 7: Details of various work found in literature that employ DIC to find polycrystalline metal grain strains 65

Table 8: Strain noise based on facet size and step for ~ 1 mm x 1 mm field of view 79

Table 9: SEM settings for single line scans 95

LIST OF FIGURES

Figure 1: Schematic of grain formation during solidification of crystalline metals [2]; (a): Crystal nuclei (b) Growth of crystallites (c) grains formed (d) grains 'boundary' observed 2

Figure 2: Crack tip in Nickel based alloy [6]; Left – strain map overlay on grain boundary map. Right – zoomed in view of strain map at vicinty of crack tip and the corresponding grain orinetation map 4

Figure 3: 2D Deformation 8

Figure 4: Digital Image Correlation Procedure 11

Figure 5: Brazilian Disk test (Inset: Speckle pattern) [12] 12

Figure 6: Square of 25 pixels around a material point P 12

Figure 7 : Initial (A) and Deformed (B) Subset Fields assigned in DIC 12

Figure 8: 25 pixel subset 13

Figure 9: Corresponding Grayscale values; [0 – Black; 255 – White] 13

Figure 10: Subset Deformation 14

Figure 11: Correlation Field [13] 15

Figure 12: Correlation Procedure Schematic (yellow: subset) 16

Figure 13 Reference image; RED subsets; grid: centers of subsets [13] 16

Figure 14: Displacement vectors obtained by image correlation [13] 16

Figure 15:Sux-pixel level schematic 17

Figure 16: Bicubic spline subpixel grayscale interpolation in an 8 pixel subset [14] 17

Figure 17: Linear Strain Scheme 18

Figure 18: Spline Strain Scheme 18

Figure 19: Strain calculation window [13] 19

Figure 20: Coordinate systems in 3-D DIC setup [16] 20

Figure 21: A typical Calibration artifact [21] 21

Figure 22: A typical Digital Image Correlation System 22

Figure 23: The schematic of a CCD camera sensor. 23

Figure 24:Camera and LED Illumination 24

Figure 25:High speed cameras [23] 24

Figure 26: Lenses [24] 24

Figure 27: Focal length and measuring distance..... 25

Figure 28: Measuring volume in 3D DIC [24] 26

Figure 29: Ideal pattern density; 100 x 80 mm FOV [30] 28

Figure 30: Typical Calibration Artifacts [30] 29

Figure 31: B- Spline parameter space correlation [54] 45

Figure 32: Error comparison of field and subset based method [34] 47

Figure 33: The adaptive FEM - DIC method;(Left: Mesh on the specimen; Right: Nodal measurement points) 47

Figure 34: Basic framework of DIC displacement and strain computation algorithms..... 48

Figure 35: Holographic recording [56] 50

Figure 36: Holographic reconstruction [56] 50

Figure 37: Line gratings with ratio of the width of the transparent space to the distance between the center lines [59] 52

Figure 38: Moiré Interferometry applied to polycrystalline aluminum [61] 54

Figure 39: The mechanism of the X ray diffraction observed in a simple cubic lattice [62]..... 56

Figure 40: 2D Grain structure of pure Al wetted with Ga – XRD [63] 56

Figure 41: X ray tomography 3D construction - A357 alloy (right) & Entrapped liquid (left) [63] 56

Figure 42: Lattice orientation (A) and Stresses (B) measured at tip of notch on MgAz31 alloy (Applied load - 170 MPa)..... 57

Figure 43: Neutron diffraction equipment schematic [66] 58

Figure 44: Stress contours on Al 2024 alloy using neutron diffraction and XRD [65]..... 59

Figure 45: EBSD orientation determination procedure [68]..... 60

Figure 46: Grain orientation maps of stainless steel from an EBSD [70]..... 61

Figure 47: Strain maps on grains obtained by grid method [71] 63

Figure 48: Surface contrast methods 66

Figure 49: DIC strain maps (Left) with grain boundaries from EBSD (left, zoomed view) [6]..... 67

Figure 50: Mgaz31 sample preparation procedure 70

Figure 51: Left - Variable length extension tube; Right - 50 mm lenses..... 71

Figure 52: Stage with three axis motion control..... 71

Figure 53: MgAz31 ~500 µm grains; ~4 mm region of interest 73

Figure 54: Strain noise as seen in feasibility study 73

Figure 55: Cylindrical specimen - surface grain structure....74

Figure 56: Cylindrical sample - strain map....74

Figure 57: DIC camera augmented with the K2 long distance microscopy lens, both mounted on an optical table....77

Figure 58: Co-axial Illumination adapter and Zoom module....78

Figure 59: Surface contrast at the crack tip; Precrack visible; FOV: ~900 x 900 µm....78

Figure 60: Optimal DIC settings for post-processing....80

Figure 61: Close-up view of K2 lens viewing the crack tip, coaxial Illumination also seen....81

Figure 62: Schematic of experimental setup....82

Figure 63: DIC system setup with the long distance microscope; Inset: CT sample with AE sensors attached....83

Figure 64: Progression of surface grains....84

Figure 65: Strain concentration around crack tip at initiation....84

Figure 66 – Epsilon Y plots at 250 nm, 500 nm and 1 µm COD....85

Figure 67 – Epsilon Y plots at 1.5 1 µm, 2 1 µm and 2.5 1 µm COD....85

Figure 68: Average strain measured by DIC correlated with the amplitude of acoustic emissions....86

Figure 69 – Displacement Y plots show development of crack path among grains....86

Figure 70 – a) COD vs. Load b) Strain from Crack Opening vs. Load....87

Figure 71: (left top) Evolution of strains along points on the specimen (left bottom) Correlation with amplitude of acoustic emission (right) snapshot of strain (top) and displacement (bottom) field at 2728.72 N....88

Figure 72: Strain along a section and strain noise spots....89

Figure 73: Strain heterogeneity along a considered section....89

Figure 74: Left - Onset of stable cracking at ~7 kN; Right – Distribution of strain in the loading direction at crack initiation....90

Figure 75: Loading device with sample mounted inside the observation room of an SEM [89]....91

Figure 76: Schematic of a comb-drive load cell [90]....92

Figure 77: Structure of a scanning electron microscope [92]....94

Figure 78: Micro load actuators; Left – SEM stage containing the comb drive actuators and the specimen [90]; Right – Thermal micro load cell sensor actuator system [91]....96

Figure 79: SEM images acquired in-situ for steel specimen loading....97

Figure 80: (left) 75 pixel facet; (right) subset field at necking....97

Figure 81: Full field DIC displacement mapping at onset of necking in specimen....98

Figure 82: Evolution of strain on specimen..... 99

Abstract

In-Situ Grain Scale Strain Measurements using Digital Image Correlation
Raghavendra Nataraj Saralaya

Materials used in engineering structures fatigue and ultimately fail due to the various applied loads they are subject to, a process which compromises structural performance and potentially poses threats to society. Commonly employed theoretical models capable of describing and predicting deformation and failure are typically validated by relevant experimental results obtained from laboratory testing. However, such models are also often based on simplifying assumptions including for example homogeneous composition and isotropic behavior, since available experimental information relates primarily to bulk behavior.

Metals are crystalline in nature and their failure depends on several parameters that span a wide range of time and length scales. Therefore, significant efforts have been made over the past decades to investigate the mechanical behavior of polycrystalline metals by formulating important microstructure-properties relations. In this context, this thesis presents a framework to obtain reliable, non-destructive, non-contact, full field measurements of deformation and strain at the grain-scale of polycrystalline materials to assist the understanding of materials phenomena and contribute in the development of realistic mechanics models. To this aim, the method of Digital Image Correlation is used, adapted and expanded.

Digital Image Correlation relies on images of the surface of tested specimens, components or structures and the identification of surface contrast patterns which are tracked as a function of deformation and are subsequently used to define displacements and strains. To quantify stains at the grain-scale, three different approaches based on Digital Image Correlation are described. The first involves the use of a commercial system adapted to make grain-scale measurements at the meso-scale (~4mm). A magnesium AZ31alloy was observed for this purpose and full field strain maps are reported. The second employs the same commercial system augmented with a long distance optical microscope to *in-situ* quantify strains at the tip of a propagating crack in a Compact Tension specimen of an Al2024 aluminum alloy subjected to Mode I loading and using a field of view of ~870 x 730 µm. Finally, the third approach uses an image series acquired from loading a stainless steel sample inside a scanning electron microscope equipped with a micro-tensile stage. Such information was post processed *ex-situ* and strains were obtained. The advantages and limitations of

the proposed approaches are critically evaluated and future work is described to further enhance the reliability and repeatability of grain scale strain measurements using Digital Image Correlation.

Page intentionally left blank

CHAPTER 1: INTRODUCTION

1.1 MOTIVATION

Engineers build machines and structures to meet a myriad of ends. They maybe bridges, automobiles, computer processors, biological implants or paper clips. These structures consist of components that are often made of metallic materials. When in operation, they experience tensile, compressive, shear etc. loading, which over a period of time can cause mechanical damage such as cracks in the component, jeopardizing in this way structural integrity, compromising performance and in some cases endangering lives.

Civil engineers, material engineers, and mechanical engineers have a vested interest in failure prediction of such metallic materials used in the structures and machines they design. If failure can be monitored, identified and predicted, timely repair and maintenance that could ensure sustained operation would be possible [1]. To this end, the field of fracture mechanics for example, has provided modeling and analysis of material behavior under stress. Typical procedures followed to assess the accuracy of the derived mechanics models include laboratory sample testing by simulating the loading conditions that exist during actual operation, as well as validation and/or updating of the assumed models based on experimental observations. In principle the accuracy of the model determines the level of success in predicting the actual material behavior and its failure.

Most metallic materials are made of crystals. Depending on the arrangement of constituent element atoms, these crystals can be of various shapes and sizes. Large arrays of such crystals in varying orientations make up the bulk of the metal. Crystals with fairly similar orientation are found in clusters within the bulk. More crystals oriented in a different direction maybe found clustered in an adjacent neighborhood as depicted in Figure 1. Grain boundaries are said to exist in the interface of the two regions that contain crystals with different orientation. Though this is the case, theoretical models of metals used to predict failure often assume homogeneity, which practically means that the presence of crystals is neglected and uniform behavior is assumed for the entire bulk. This limits the use of these models to predict failure in real life scenarios in which progressive damage and ultimate failure appear to localize as a function of the materials' microstructure. In this context, there is a significant interest today to investigate and develop analytical, experimental and computation techniques capable to quantify information at the materials microstructure in order to form direct links between material behaviors at the grain scale with bulk mechanical behavior. This link is the motivation for the research presented in this thesis.

Figure 1: Schematic of grain formation during solidification of crystalline metals [2]; (a): Crystal nuclei (b) Growth of crystallites (c) grains formed (d) grains 'boundary' observed

FRACTURE MECHANICS

The work presented in this thesis is relevant to the field of Fracture Mechanics. Advances in this field rely on research and development of experimental techniques that could provide direct quantification of material behavior at significantly lower scales than the macroscale, at which the microstructure of the material can be seen. Such novel techniques could provide essential input to fundamental assumptions that have been formulated in the past related to deformation and fracture. For example, in one of the early initiatives to assess grain influence on the crack tip taken by Ritchie and Thompson [3], efforts to determine the criteria for fracture initiation in terms of grain mechanisms like intergranular cracking, transgranular cleavage, and microvoid coalescence were made. In both the linear-elastic and elastic-plastic fracture mechanics approaches, however, crack initiation models have stringent restrictions on the amount of plastic deformation that could exist for consistent application to various real life scenarios. Crack initiation and propagation are characterized for a given material configuration

from a macroscopic view point with an extremely simplified treatment of the plastic zone at the crack tip. Such characterizations often avoid addressing plasticity in a direct manner and depend on approximating the actual plastic zones

CRYSTAL PLASTICITY

The procedures and results presented in this thesis are also relevant to the field of crystal plasticity which approaches the bulk mechanical behavior of materials from the perspective of grain-scale effects at the microscale. Specifically, crystal plasticity relies on microstructural parameters such as grain misorientations, size and size distribution, as well as information about the material such as slip, dislocation motion, twinning etc. which affect plasticity and fracture. Reference [4] provides one of the first crystal plasticity models developed based on crystallographic shearing and the elastic-plastic framework for deformation analysis in single crystals. In recent studies, finite element methods are used to simulate plastic deformation based on crystal plasticity for polycrystalline materials [5].

The deformation gradient of the crystal geometry considered, **F**, is multiplicatively decomposed into elastic and plastic components $\mathbf{F_e}$ and $\mathbf{F_p}$. On a similar note, the velocity gradient, **L,** is additively decomposed into elastic and plastic components $\mathbf{F_e}$ and $\mathbf{F_e}$. The plastic part of the velocity gradient, $\mathbf{L_p}$ is computed from the slip rates of slip systems in the material considered using (1) [4, 5].

$$L_p = \sum_{\propto=1}^{N} \dot{\gamma}^{\propto} s^{\propto} \otimes m^{\propto} \tag{1}$$

WHERE:

$s^{\propto}$ Directions of slip systems $m^{\propto}$ Normals to slip systems

$\dot{\gamma}^{\propto}$ Slip rates

With increase in computing power over the years, finite element crystal plasticity models [6] are now being used in the microscale material mechanics modeling. FEM representative volume elements (RVE) at various length scales are built to model the behavior of polycrystalline materials. The basis for building such models, however, is relevant experimental results similar to what is described in this thesis.

1.2 WHY DIGITAL IMAGE CORRELATION?

Full field displacement and strain measurements provide the necessary global and local density of data required to quantify material behavior and assist in the development of realistic models. In this context, traditional contact methods, such as

strain gages are rendered practically incapable of measuring full field strains and even more so measuring strains across grains in a polycrystalline material.

Digital Image Correlation (DIC) is a versatile full field deformation metrology solution. Its use can be adapted to perform nanoscale to meter-scale surface deformations measurements. DIC is a practical non-contact tool that can be used to obtain accurate *in-situ* full field strain measurements. Keeping in mind that X-ray diffraction, Raman spectroscopy, Speckle Interferometry, Neutron diffraction, and Electron diffraction techniques are also capable of making deformation measurements at grain and even lattice-scale, DIC is a novel alternative that has unique advantages and provides a robust and practical solution for multiscale strain measurements using a simple data acquisition procedure based on clicking pictures using high resolution cameras and image processing them to get results with outstanding resolution and accuracy.

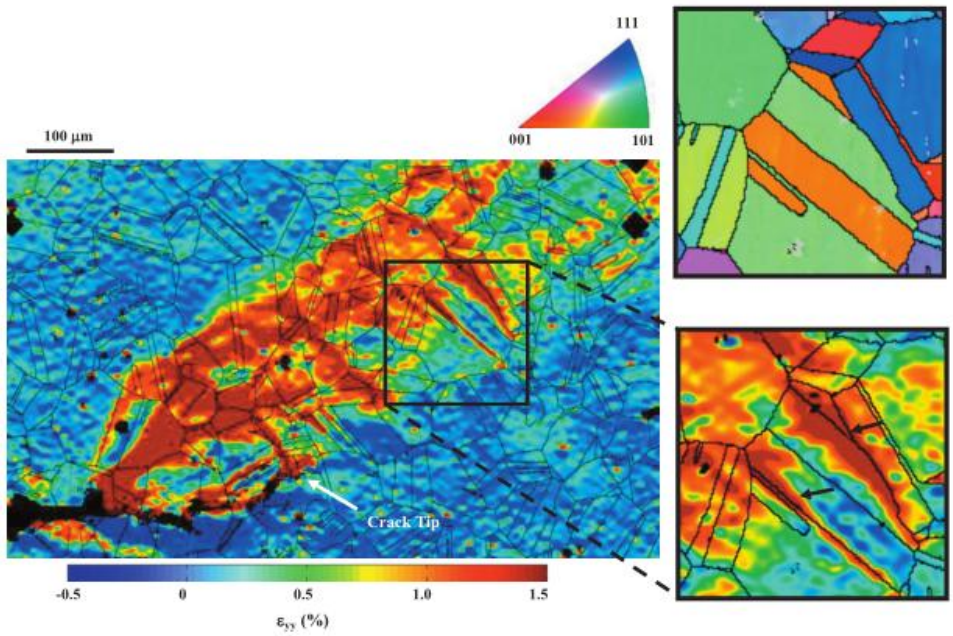

Figure 2: Crack tip in Nickel based alloy [6]; Left – strain map overlay on grain boundary map. Right – zoomed in view of strain map at vicinty of crack tip and the corresponding grain orinetation map

The chief drawback of Digital Image Correlation compared to high penetration methods like neutron diffraction and high energy x-ray diffraction is that it cannot probe into the thickness of the material. However, comparing the equipment cost and the time taken to the make similar measurements with comparable accuracy, the use of DIC in monitoring

polycrystalline materials, either in the research laboratory or in the field, is justified and there is the need to further develop, and validate its use as presented in this thesis.

1.3 THESIS ARRANGEMENT

This thesis has seven chapters. The first chapter explains the need for grain-scale strain measurements and why digital image correlation is chosen for such measurements. The second chapter explains in fair amount of detail the principles behind the working of digital image correlation. The third chapter provides an overview of the methods generally used to observe and quantify deformation in the grains of polycrystalline materials. It also discusses various instances of application of DIC for quantifying strain in polycrystalline materials. Chapter four describes an attempt to directly extend the use of a commercially available DIC system's 2D configuration to perform grain boundary pattern matching. Chapter five again takes an *in-situ* 2D DIC approach on an aluminum alloy CT specimen. The key note of this experiment is the augmentation of the high resolution DIC camera used in chapter four with a long distance microscope to observe a much smaller region of interest. Chapter six describes how an image series acquired *in-situ* using a scanning electron microscope during loading of a steel alloy was used for DIC with no prior sample preparation done for image correlation. The strain obtained from DIC was validated with the strains obtained from the load cell strain gage. Finally, chapter seven discusses shortcomings of the methods utilized in this thesis and the steps to be taken to overcome these shortcomings. It also gives the general direction for further development of the methods used in this thesis.

CHAPTER 2: DIGITAL IMAGE CORRELATION

2.1 INTRODUCTION

Digital Image Correlation (DIC), also known as digital speckle correlation method (DSCM), texture correlation, computer-aided speckle interferometry (CASI) and electronic speckle photography (ESP) is a non-contact, optical technology used to perform surface measurements [7]. Cameras are used to acquire images of a specimen whose surface has dense variations in contrast. These images are then processed digitally in a computer and intensity analysis is performed on the region of interest captured in these images to obtain surface co-ordinates, displacement and strain along with their rates. Measurements can be made at scales ranging from a few meters to nanometers. Tested specimen can be under quasi-static or dynamic loading. Temporal frequencies of many images per second can be achieved with the hardware capabilities available in the market today. As a result, DIC has found extensive application inside the laboratory as well as in the industry. The feature that has made this technique popular in the displacement and strain measuring community is its ability to provide full field measurements of the specimen observed with ease compared to its alternatives. Full field strains assist the quantitative understanding of material phenomena, relating local information to global characteristics which before DIC was very difficult to achieve.

2.2 DEVELOPMENT OF DIC

Sutton et al. developed the initial implementations of Digital Image Correlation technique in the early 1980s [8, 9]. The correlation procedure was originally used for tracking material changes by monitoring ultrasonic waves reflected from material during loading. Fundamental concepts of continuum mechanics were used for the correlation process. Their DIC implementation was capable of two-dimensional correlation using white speckles. A 512 x 512 pixel sensor array was used and the image was digitized using a VAX and PDP – 8/E mini computers to assign a gray value between 0 and 255 to the picture element (pixel) acquired by each of this sensor. However, only one point of interest could be tracked. A point load was applied at the free end of a cantilever beam and the deflection along the beam was measured using DIC. The results thus obtained were in good agreement with finite element analysis of the beam. This original method proposed by Sutton underwent many improvements, modifications, validations and various algorithms for the numerical implementations of the method emerged through research all over the world [10]. The method gained acceptance and popularity in the experimental mechanics community for planar full field strain measurements due to its ease of use. With the advent of powerful microscopy technology like scanning tunneling microscopy and scanning electron microscope, the two-

dimensional implementation was extended to the micrometer regime [10]. It was also applied to two-dimensional fluid flow to measure velocities. The complexity of displacements that could be tracked improved with introduction of higher order displacement mappings. Finite Element Methods from computational mechanics also severed as an inspiration to the programmers of Digital Image Correlation software and as a result continuum type, mesh correlation algorithms were developed.

Table 1: Salient developments in methods of DIC [10]

DATE	DEVELOPMENT	CONTRIBUTORS:
1983	Feasibility of 2D DIC was proved	Sutton et al.
1984	2D DIC was applied to measure velocity in fluid systems	Chu et al.
1986	2D DIC was improved to subpixel accuracy	Sutton et al.
1987	2D DIC was used in estimating stress intensity factor	McNeil et al.
1993	Fast Fourier Transform correlation process was applied	Cheng et al.
1994	Automated 3D DIC was first realized in measuring crack tip deformations	Sutton et al.
1995	Volumetric DIC using X ray computed tomography was applied in measuring volumetric 3D strains in trabecular bone	Bay
1998	2D DIC was used with scanning tunneling microscopy to get deformations at a submicron scale	Vendroux and Knauss
	Bundle adjustment techniques were adapted into 3D DIC for flexible and robust calibration	Lavest, Viala and Dhome
1999	3D DIC was done in SEM by in-situ specimen tilting	Lockwood and Reynolds
2000	Accuracy was greatly improved by using higher order deformation functions and higher order spline functions for intensity interpolation	Schreier et al.
	Bundle adjustment calibration efficiency was improved greatly with a seven parameter stereo-camera model	Garcia et al.
2003	3D DIC and high speed imaging were integrated and studied	Tiwari, Sutton and Mcneill
2005	Finite Element Methods were extended to 2D DIC	Réthoré, Hild and Roux
2008	Scanning Electron Microscope was used to measure μstrains using 2D DIC	Sutton et al.
	3D DIC with motion and temperature estimates from same camera system	Orteu et al.

Using the principles of triangulation and bundle adjustment optimization in stereo imaging, two cameras were used simultaneously to successfully implement three-dimensional digital image correlation which is sensitive to depth of field and

out-of-plane motion. Thus, strains and displacements in the z-direction were also made possible. With the advent of volumetric imaging techniques such as Computer-aided Tomography (CT) and Magnetic Resonance Imaging (MRI) in the medical field, their use was adapted to the implementation of digital correlation of the volumetric scans. This led to volumetric DIC for full field volumetric three-dimensional displacement and strain mapping [11].

2.3 THEORY

2.3.1 2D CONTINUUM MECHANICS

DIC is used to estimate the unknowns in displacement field formulations in continuum mechanics. Consider an *infinitesimally small line segment* ***PQ*** of length *ds* as shown in Figure 3 in the initial configuration of the object. The infinitesimally small line segment **PQ** transforms to **P'Q'** after deformation.

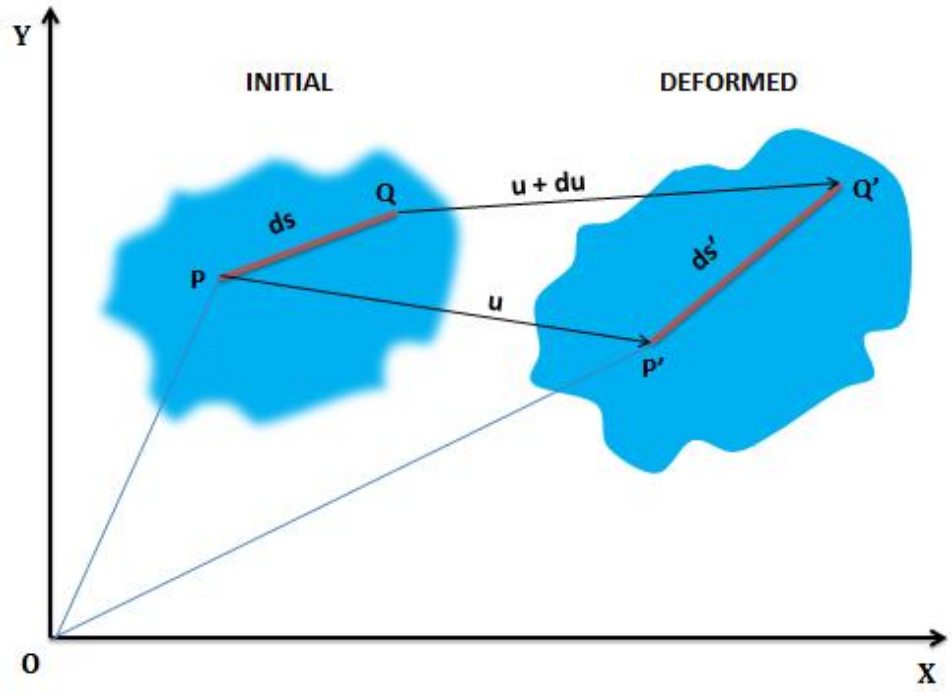

Figure 3: 2D Deformation

Using infinitesimal formulations,

Table 2 shows the coordinates of points P, Q, P and Q' thus obtained.

Table 2: PQ Coordinates

	INITIAL STATE	DEFORMED STATE
Point P	$[\,\boldsymbol{x}\,,\boldsymbol{y}\,]$	$[\,\boldsymbol{x}+\boldsymbol{u}(\boldsymbol{P})\,,\boldsymbol{y}+\boldsymbol{v}(\boldsymbol{P})\,]$
Point Q	$[\,\boldsymbol{x}+\boldsymbol{dx}\,,\boldsymbol{y}+\boldsymbol{dy}\,]$	$[\,\boldsymbol{x}+\boldsymbol{dx}+\boldsymbol{u}(\boldsymbol{Q})\,,\boldsymbol{y}+\boldsymbol{dy}+\boldsymbol{v}(\boldsymbol{Q})\,]$

Where *dx* and *dy* are components of *ds*. After deformation *ds* changes to *ds'*, where *dx'* and *dy'* are its components. In terms of **P'** coordinates, **Q'** coordinates are (2):

$$[\,x+u(P)+dx'\,,y+v(P)+dy'\,] \tag{2}$$

Hence,

$$\begin{aligned} u(P)\ +\ dx'\ =\ dx\ +\ u(Q) \quad &\rightarrow \quad dx'\ =\ u(Q)\ -\ u(P)\ +\ dx \\ v(P)\ +\ dy'\ =\ dy\ +\ v(Q) \quad &\rightarrow \quad dy'\ =\ v(Q)\ -\ v(P)\ +\ dy \end{aligned} \tag{3}$$

Expressing the lengths of **PQ** and **P'Q'** in terms of their coordinates and the differential components and we get:

$$\begin{aligned} (ds)^2\ &=\ (dx)^2\ +\ (dy)^2 \\ (ds')^2\ &=\ (dx')^2\ +\ (dy')^2 \\ (ds')^2\ &=\ (u(Q)\ -\ u(P)\ +\ dx)^2\ +\ (v(Q)\ -\ v(P)\ +\ dy)^2 \end{aligned} \tag{4}$$

Performing a *first order Taylor's expansion* for the displacement function about the point **P** gives the displacement of Q in terms of the displacement of P.

$$\begin{aligned} u(Q) &= u(P)+\frac{\partial u}{\partial x}dx+\frac{\partial u}{\partial y}dy \\ v(Q) &= v(P)+\frac{\partial v}{\partial x}dx+\frac{\partial v}{\partial y}dy \end{aligned} \tag{5}$$

Using these relationships, we can now express *dx'* and *dy'* in terms of the Taylor's expansion

$$(ds')^2\ =\ (\frac{\partial u}{\partial x}dx+\frac{\partial u}{\partial y}dy+\ dx)^2\ +\ (\frac{\partial v}{\partial x}dx+\frac{\partial v}{\partial y}dy+\ dy)^2 \tag{6}$$

The Cauchy's strain tensor and the infinitesimal rotation tensor can be obtained from the linear Taylor expansion. The Taylor's expansion is given by

$$u(Q) = u(P) + \frac{\partial u}{\partial x}dx + \frac{\partial u}{\partial y}dy$$
$$v(Q) = v(P) + \frac{\partial v}{\partial x}dx + \frac{\partial v}{\partial y}dy \quad (7)$$

This can further be expanded as:

$$u(Q) = u(P) + \frac{1}{2}\left\{\frac{\partial u}{\partial y} + \frac{\partial v}{\partial x}\right\}dy + \frac{1}{2}\left\{\frac{\partial u}{\partial y} - \frac{\partial v}{\partial x}\right\}dy$$
$$v(Q) = v(P) + \frac{1}{2}\left\{\frac{\partial v}{\partial x} + \frac{\partial u}{\partial y}\right\}dx + \frac{1}{2}\left\{\frac{\partial v}{\partial x} - \frac{\partial u}{\partial y}\right\}dx \quad (8)$$

The Cauchy's infinitesimal strain tensor is given by:

$$\in = \frac{1}{2}\left\{\frac{\partial u}{\partial y} + \frac{\partial v}{\partial x}\right\} \quad (9)$$

The infinitesimal rotation tensor is given by:

$$\omega = \frac{1}{2}\left\{\frac{\partial v}{\partial x} - \frac{\partial u}{\partial y}\right\} \quad (10)$$

The strains in the X and Y direction, and the shear strain can be obtained from the gradients of the displacement field. It is important to keep in mind the assumptions made in this analysis of deformation.

- Line segment PQ is assumed to be infinitesimal. Hence, P is in the neighborhood of Q. The same assumptions hold good for line segment P'Q'.
- Mapping between PQ and P'Q' are one-to-one and continuous.
- Since the displacements assumed are infinitesimal, the expressions for strain and rotation are also approximated for infinitesimal quantities.

2.3.2 IN-PLANE DISPLACEMENT MAPPING ESTIMATION BY IMAGE CORRELATION

Estimation of transformation from the initial to the deformed material configuration is done by image correlation whose basic procedure is shown in. Figure 4. Any image acquired from a digital camera is composed of *m x n* pixels. Based on the intensity of light received at the pixel sensor, the pixel is assigned an intensity value. Typically, a grayscale value between 0 and 255 (2^8 values) is assigned to a pixel in an 8-bit monochrome digital camera. These intensity values are used in image matching algorithms. To effectively represent the material surface points in the images for these algorithms, a pattern with densely varying contrast is applied to the surface of the material. This is commonly referred to as speckle patterning in DIC

and is shown In Figure 5. As the surface of the material deforms, the speckle pattern also deforms with it and serves as a carrier of the deformation information in to the images.

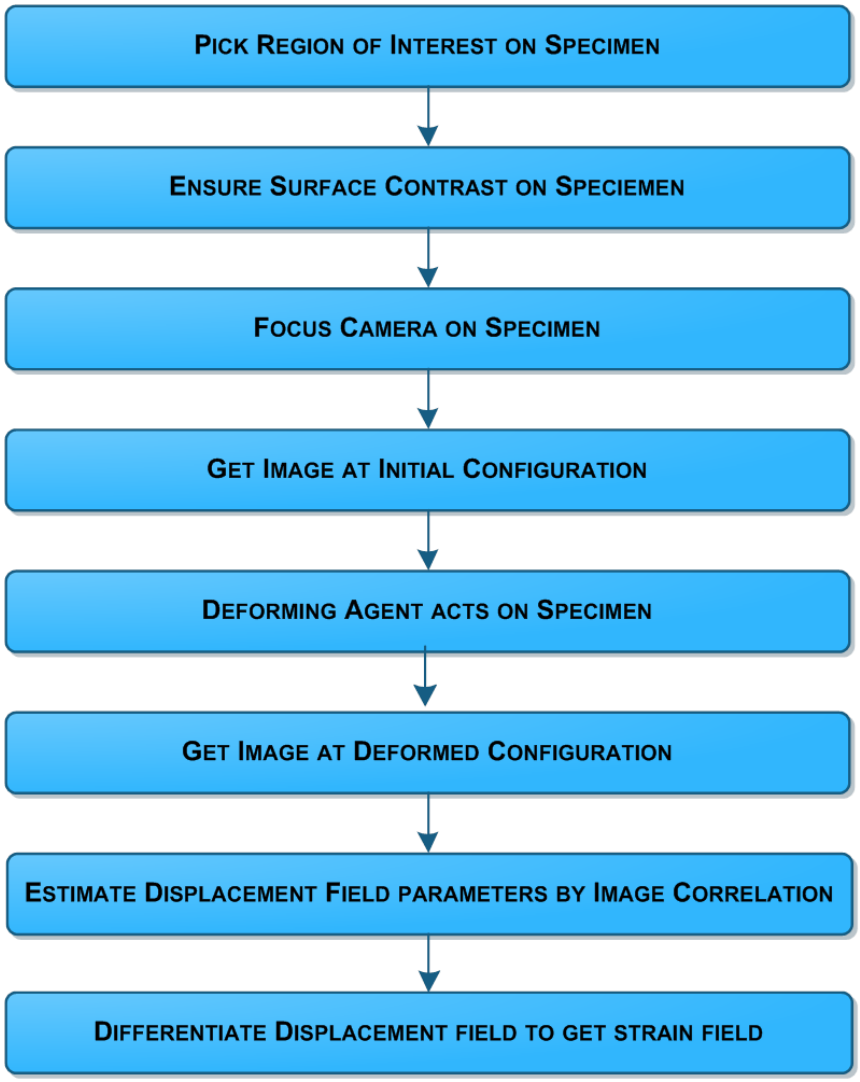

Figure 4: Digital Image Correlation Procedure

A typical speckle pattern consists of a thin coat of white paint in sprayed on to the plain surface. Black speckles are then sputtered on this white coat. Figure 6 shows the initial undeformed image of such a patterned specimen. The sample then is put up on a loading frame and high resolution charged couple device (CCD) cameras are setup to look at the region of interest. Lenses are used to direct the light from the specimen on to the camera sensor.

Let us now consider an image acquired of the speckle patterned surface at the undeformed state of the specimen depicted by Figure 7 **A**. Another image as shown by Figure 7 **B** is acquired at the deformed state. Consider a material surface point **P** that is present in both images. To find its displacement, this material point must be identified in both images and coordinates based on a fixed reference frame must be assigned. To uniquely identify point **P** in the reference and the deformed image, a rectangular (or square) patch of pixels, called a subset, centered on this material point **P** as shown in Figure 6 is used.

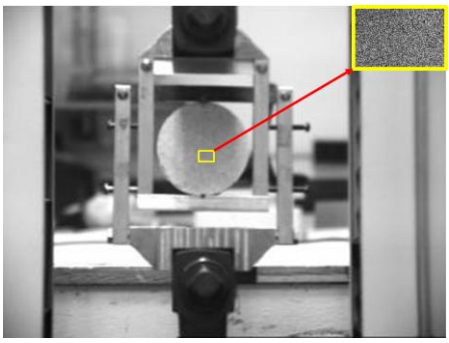

Figure 5: Brazilian Disk test (Inset: Speckle pattern) [12]

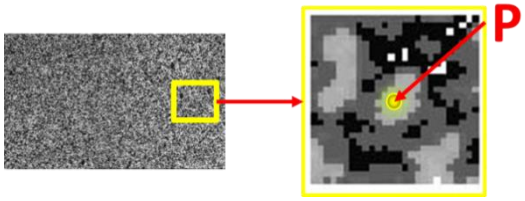

Figure 6: Square of 25 pixels around a material point P

Similarly, all the material points covered by the speckle pattern can be assigned its own square of pixels for identification. This gives rise to a field of subsets in the undeformed reference image and the deformed image. An example is shown in Figure 7

.

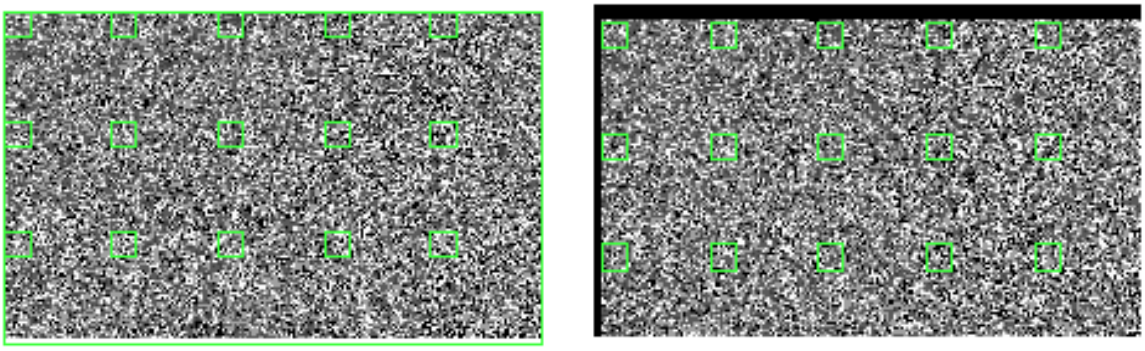

(A) (B)

Figure 7 : Initial (A) and Deformed (B) Subset Fields assigned in DIC

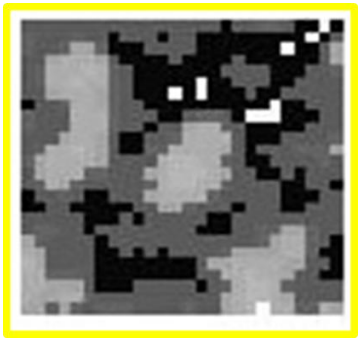

Figure 8: 25 pixel subset

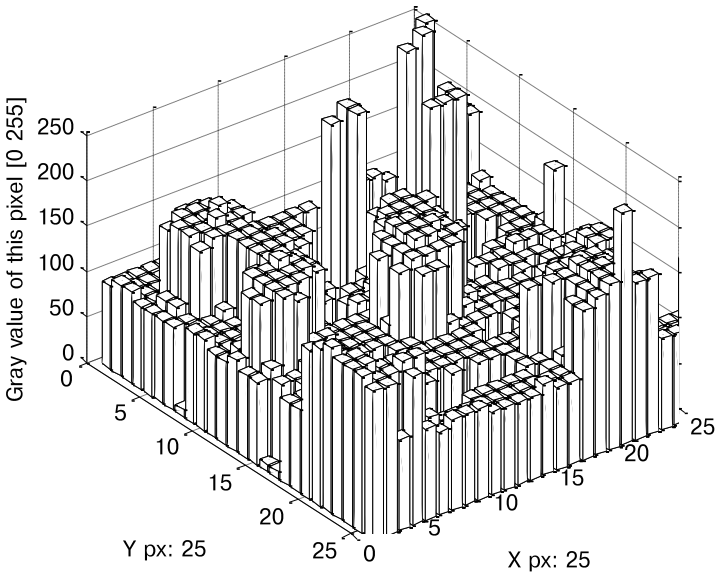

Figure 9: Corresponding Grayscale values; [0 – Black; 255 – White]

In the numerical processing of images for correlation, the grayscale intensity values in the subset are used to uniquely identify the material point at the subset center and same material point is identified in other images by finding the best match for this subset. A subset is preferred to an individual pixel for correlation as the grayscale values of a subset is statically unique as compared to individual pixels and can be identified in the deformed as well the undeformed images [9, 13]. It is important to keep in mind that assumptions from continuum mechanics carry through to the optical deformation measurements. The ones to be kept in mind are:

- The subset itself deforms when the material deforms but the a neighborhood of material points within a given subset in **A** remain in the same subset in **B** [13]
- The intensity pattern in subsets of **A** and **B** are related mathematically by a homogeneous linear mapping that applies to the deformation on the surface of the actual material [9]

This means that grayscale value of some point Q which was in the vicinity of P in the reference stage is still in its vicinity in the deformed stage. The deformation of the specimen changes the surface pattern such that the point **Q** retains the same grayscale value in the deformed stage. Looking back at the continuum equations, we get the displacement equation (5) for any point **Q** in the vicinity of **P**. The physical deformation of the material causes the pattern applied on it to deform with it. This deformation information is carried into the images through the grayscale values and translates the deformation to the subset field [13] shown in Figure 7. Individual subset deformation occurs as shown in Figure 10.

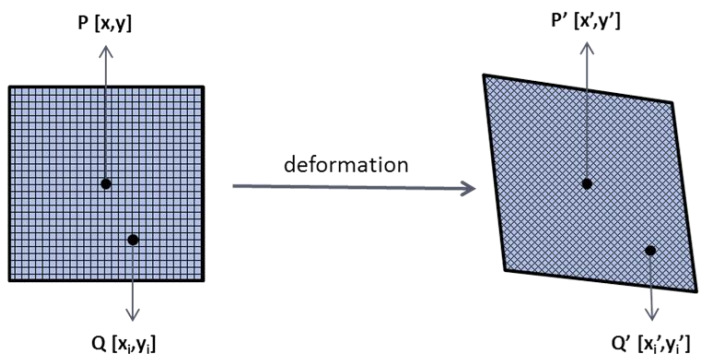

Figure 10: Subset Deformation

The adaptation of the deformation mapping from continuum mechanics to grayscale values within subsets thus looks like as follows:

$$x_i' = x_i + u + u_x\Delta x + u_y\Delta y \qquad (11)$$

$$y_j' = y_j + v + v_x\Delta x + v_y\Delta y$$

WHERE:

x_i', y_j'	**Q** coordinates after deformation
x_i, y_j	**Q** coordinates before deformation
i, j	$-h \le i \le h; -w \le j \le w$; for (2h+1 x 2w+1) pixel subset
u, v	Displacement of subset center in x, y
u_x, u_y, v_x, v_y	First order displacement gradients of the reference subset
$\Delta x, \Delta y$	x, y distance of pixel **Q** from pixel **P**

Here, **P**, the material point of interest, is the subset center and **Q** represents material points at the center of every other pixel in the subset. The basic problem to be solved by the numerical procedures of correlation is estimating the best values of the unknowns: *u, v, ux, uy, vx,* and *vy* in equation (5) at the centers of each subset. Optimization procedures are utilized for this purpose. Each subset in the deformed image is compared with all of those in the reference image or a predefined searching area [13] and a correlation coefficient is used to grade each comparison a score (12).

Cross-correlation coefficient: $C_{CC} = \sum_i \sum_j [f(x_i, y_j) g(x_i', y_j')]$ (12)

WHERE:

$f(x_i, y_j)$: Grayscale value at pixel x_i, y_j

$g(x_i', y_j')$: Grayscale value at pixel x_i', y_j'

This process yields a correlation field indicating the level of similarity for all the subsets in the reference image. A typical correlation field is shown in Figure 11.

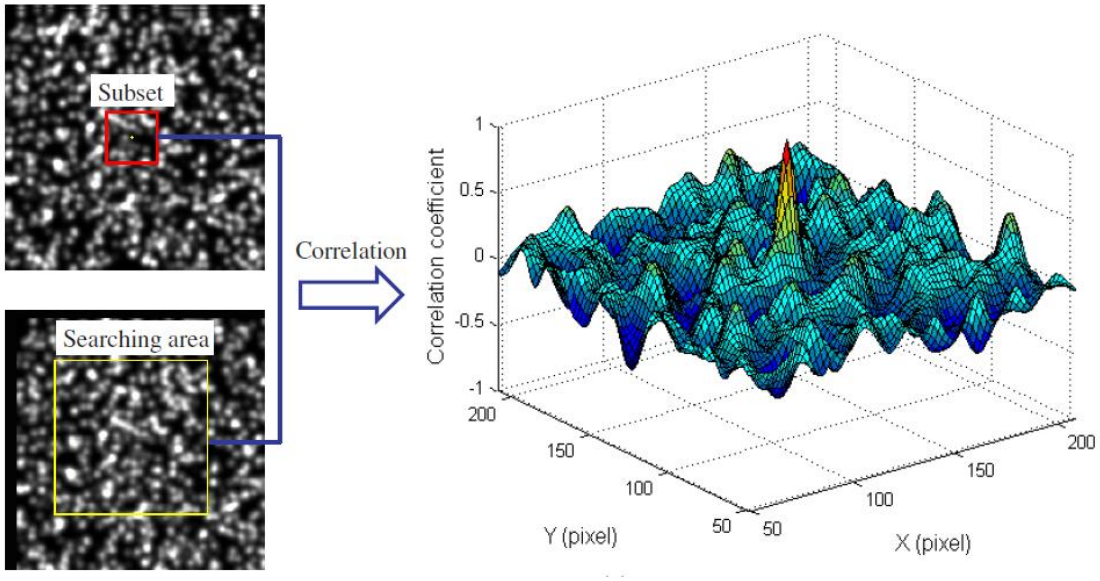

Figure 11: Correlation Field [13]

A global peak gives the location of the best match for this subset as seen in Figure 11. The unknown variables u, v, u_x, u_y, v_x, and v_y for the center of the subset are optimized based on this location at the integer pixel level. Newton-Raphson iterative optimization is a popular optimization scheme employed in improving an initial guess of the unknowns iteratively until a predefined pixel accuracy requirement is met. The initial guess is usually obtained by search methods utilized for a defined search region where the displacement is expect to take place [9]. By repeating this optimization procedure for every subset in the deformed image, the displacement field for the entire field of view is obtained. At the end of the optimization routine, the points being tracked on the image and their corresponding displacements look as shown in Figure 13 and Figure 14.

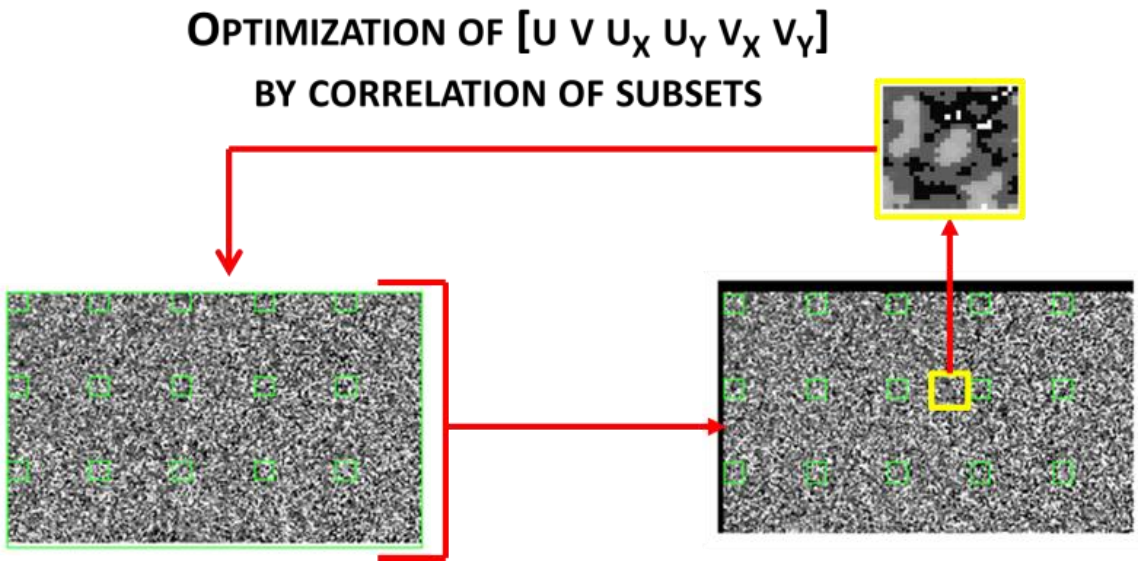

Figure 12: Correlation Procedure Schematic (yellow: subset)

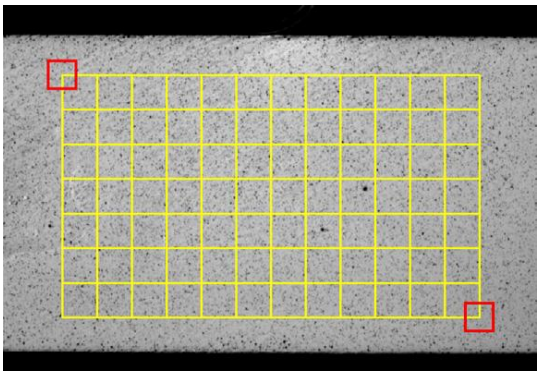

Figure 13 Reference image; RED subsets; grid: centers of subsets [13]

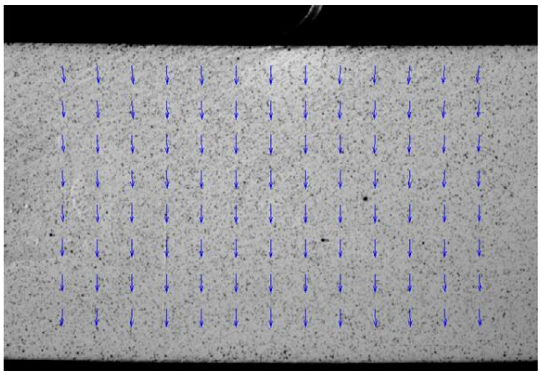

Figure 14: Displacement vectors obtained by image correlation [13]

SUBPIXEL DISPLACEMENTS

Each pixel is a discrete entity. Even when a 5 megapixel camera is used to look at a sample that is 5 cm long and 5 cm wide, each pixel covers an area of about 5 mm^2 and represents only the center of this 5 mm^2 material area. However, there are more material points between centers of two adjacent pixels Figure 15. To account for this material, one can use overlapping subsets. However, after a threshold, increase in overlapping of subsets induces noise from algorithm in the displacements

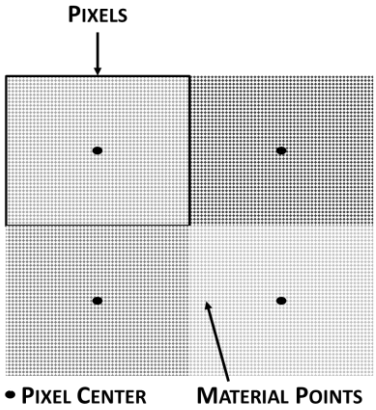

Figure 15:Sux-pixel level schematic

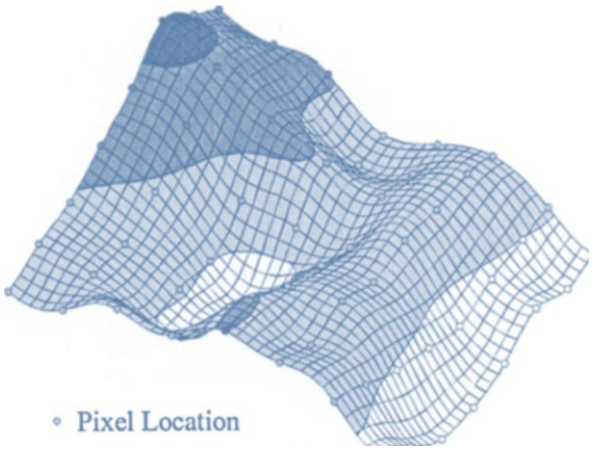

Figure 16: Bicubic spline subpixel grayscale interpolation in an 8 pixel subset **[14]**

To push the resolution even higher with the available information from the images, subpixel intensity interpolation is used to represent the material points in between the centers. The grayscale values of pixels in any considered deformed subset are discrete as shown in Figure 15. A surface is fit into the grayscale values of the subset by interpolation [9] as shown in Figure 16. This surface gives a much higher spatial resolution for material point representation as compared to using only pixels. The number of pixels used to interpolate sub-pixel intensities depends on interpolant utilized. Correlation performed on the grayscale values of this fitted surface gives us displacements and its gradients with subpixel resolution. The integer pixel level displacements and gradients are used as initial guess for the subpixel level correlation routine.

STRAIN CALCULATIONS

Once the displacements at all the subsets in the deformed image have been calculated, the strains are calculated using this displacement field using numerical differentiation techniques. Numerical differentiation of the discrete displacement field obtained by the optimization process at the subset centers by itself induces a lot of noise [13] into the strains computed. To improve the strain computation accuracy, displacement of a square window of subset centers is used to compute a continuous displacement field. Assuming the strain varies linearly in the assumed window, the displacement in this window is assumed to have a form of

$$\begin{aligned} u &= a_0 + a_1 x + a_2 y \\ v &= b_0 + b_1 x + b_2 y \end{aligned} \tag{13}$$

The values of a_0, a_1, a_2, b_0, b_1, and b_2 are obtained using the displacement values at the subset centers in the picked strain window. To compute strains at the subset centers at the edges, the displacement field is extended using continuity extension to obtain the displacements at the boundary [13].

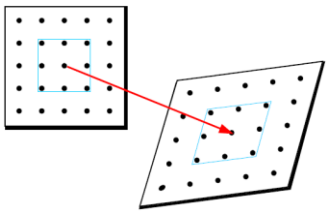

Figure 17: **Linear Strain Scheme**

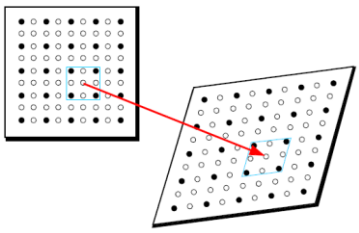

Figure 18: **Spline Strain Scheme**

Hence, only six valid subset centers are required to compute the strain at the center of this window. A typical strain calculation window is shown in Figure 19. In the commercial DIC software ARAMIS, the size of this window is called the "strain computation size" in its linear strain computation scheme as shown in Figure 17. In the spline strain method, an interpolation scheme is used to obtain displacement values in between the measurement grid from the subset field.

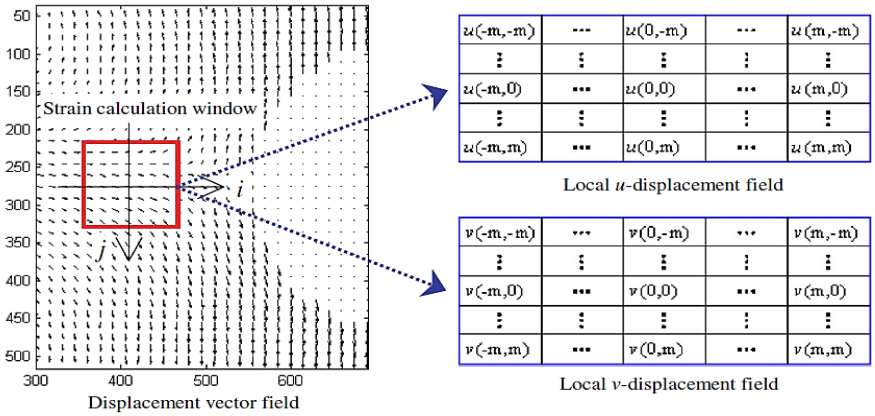

Figure 19: Strain calculation window [13]

For in-plane two-dimensional strain the formula used is given by:

$$\epsilon_{xx} \cong \frac{\partial u}{\partial x} + \frac{1}{2}\left\{\frac{\partial u^2}{\partial x} + \frac{\partial v^2}{\partial x}\right\} \tag{14}$$

$$\epsilon_{yy} \cong \frac{\partial v}{\partial x} + \frac{1}{2}\left\{\left(\frac{\partial u}{\partial y}\right)^2 + \left(\frac{\partial v}{\partial y}\right)^2\right\} \tag{15}$$

$$\epsilon_{xy} \cong \frac{1}{2}\left(\frac{\partial u}{\partial y} + \frac{\partial v}{\partial x}\right) + \frac{1}{2}\left\{\frac{\partial u}{\partial x}\frac{\partial u}{\partial y} + \frac{\partial v}{\partial x}\frac{\partial v}{\partial y}\right\} \tag{16}$$

When these relationships between the displacement gradients and strain is used to compute strains in DIC, it is assumed that out-of-plane displacements affects in-plane displacements minimally [15].

2.3.3 3D Image Correlation

Stereo Vision: Two cameras can be used together to get stereo-vision, enabling extension of Digital Image Correlation to three-dimensional measurements. The techniques of photogrammetry for three-dimensional geometry reconstruction using paired digital camera images in the computer vision community has enabled the experimental mechanics community perform optical three-dimensional strain measurements.

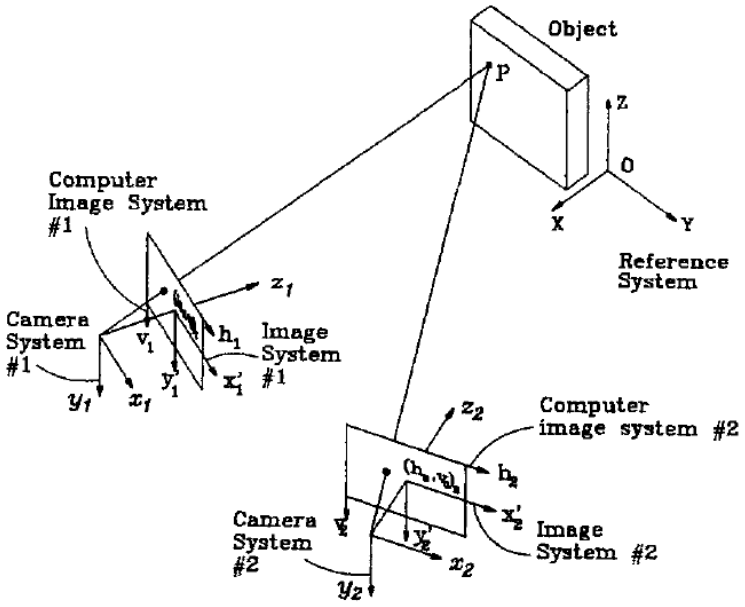

Figure 20: **Coordinate systems in 3-D DIC setup [16]**

A model of a camera such as the pin-hole camera is assumed to mathematically relate the world co-ordinates into the acquired image's coordinates. To make a 3D measurement possible, the stereo camera pair model must first be calibrated to get camera centers and angles with respect to the reference frame, lens distortion, and other geometric parameters of the stereo camera model assumed [16-19]. Once calibrated, the images must be stereo-correlated to be able to identify same point in both images using triangulation [18].

BUNDLE ADJUSTMENT: Calibration for a single camera involves determining the camera model parameters shown in Table 3. For a stereovision setup, in addition to these parameters, the relative position and orientation between the cameras must also be determined. This is done by the process called bundle adjustment. Images of a patterned artifact with regularly spaced dots at known distances are acquired at many orientations. Since the distances between the dots in the images are known, information from all images is used to initialize these dots in the virtual three-dimensional space of the correlation system called the measuring volume. The least squared difference between dots in every picture and these initialized points is minimized by finding the system's optimal intrinsic and extrinsic parameter values by an optimization algorithm such as the Levenberg-Marquardt algorithm [19]. The images obtained from the calibrated system are first aligned and the same material points on the image pairs are identified. Using the camera model parameters computed earlier, the three-dimensional geometry of the object in image pair is reconstructed using triangulation techniques [20]. Similar to two-

dimensional DIC, image pairs of the specimen's reference and deformed configuration are acquired using the stereo-vision setup.

Table 3: Parameters to be estimated during camera calibration

Intrinsic Parameters		Extrinsic Parameters	
$[u_o, v_o]$	The coordinates of intersection of the optical axis and the retinal plane	R	Camera rotation with respect to global coordinates
$\alpha_u = fk_u$ $\alpha_v = fk_v$	Two scale factors along the vertical and horizontal axis of the image	t	Camera translation with respect to global coordinates

Where: f is the focal length in length units; k_u and k_v are the numbers of pixels per unit length

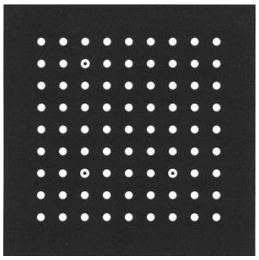

Figure 21: **A typical Calibration artifact [21]**

The material surface is three-dimensionally reconstructed for every deformed image pair. The three-dimensional reconstruction in the reference and the deformed image is compared to find the displacement field for the object surface. This process is called temporal matching [18]. Local strains are computed in small windows of the displacement field. The ARAMIS digital image correlation software distinguishes between two methods of computing strains (1) linear strain and (2) spline strain. In the linear strain method, the strains are obtained from the displacements computed directly from subset centers. In the spline method, more points are interpolated between the displacements obtained directly from the subsets. ARAMIS allows for the concept of a 'validity quote' in strain calculation which allows not counting points at the edge for computing strain as this adds noise to the measurement. [18] use ABAQUS finite element software to calculate the strain fields from the three-dimensional displacement fields obtained, effectively utilizing finite element meshing techniques.

2.4 EQUIPMENT & PROCEDURE

A typical DIC system (Figure 22) consists of optical sensors, a data acquisition system (DAQ) and a digital computer. High resolution charge-coupled device (CCD) sensors are used for image acquisition. These are connected to a frame grabber which serves as a live interface between the sensors and the computer. It also supplies power to the cameras. The computer provides a user interface for the whole system, enabling control of image acquisition and system parameters during the measurement and processing after the measurement. Lenses are used to focus light rays from region of interest onto the sensor.

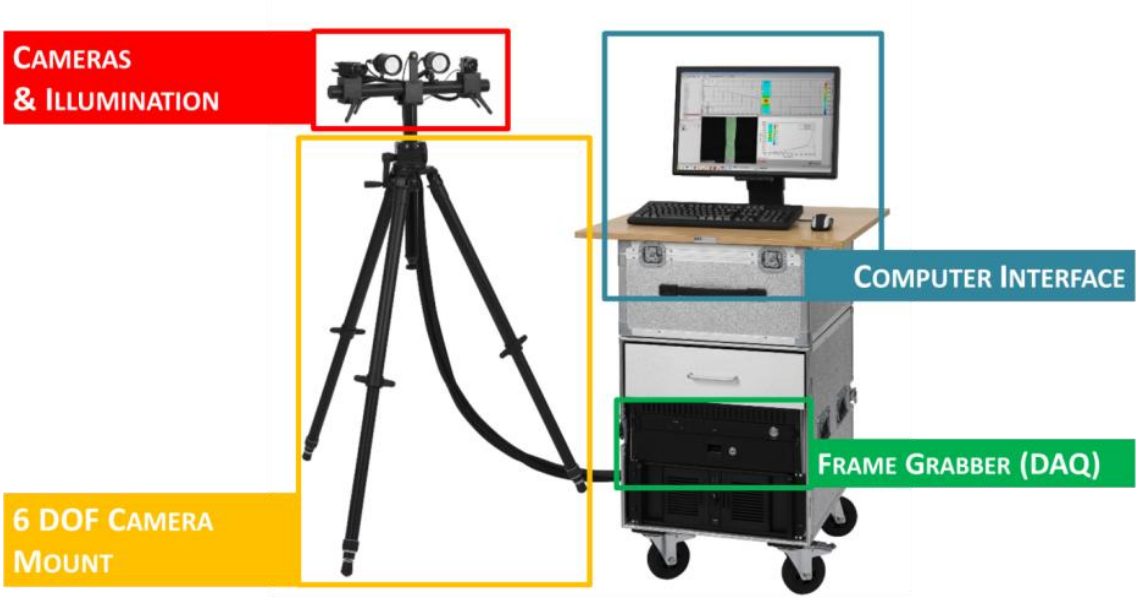

Figure 22: A typical Digital Image Correlation System

HARDWARE COMPONENTS AND PARAMETERS

The two key components of the optical part of the DIC system are lens and camera. The camera houses the light sensor on to which the lens directs light from the region of interest. Light sources are used to illuminate the region of interest. Tripods, horizontal bars and mounts are used to provide mechanical stability as per the application requirements.

CAMERAS

Image sensors are of two types: Charged Couple Devices (CCD) and Complementary Metal Oxide Semiconductor (CMOS). CCD sensors produce higher image quality [22] and are appropriate for optical metrology applications such as DIC. The sensors themselves are an array of metal oxide semiconductors corresponding to pixels. Each pixel accumulates electric charge based on local illumination intensity. When exposure of the image sensor is complete, the charge at each pixel area is transferred to an output which converts the charge to a voltage and sends it for further gain and signal processing on the camera printed circuit board. The schematic of the flow is shown in Figure 23

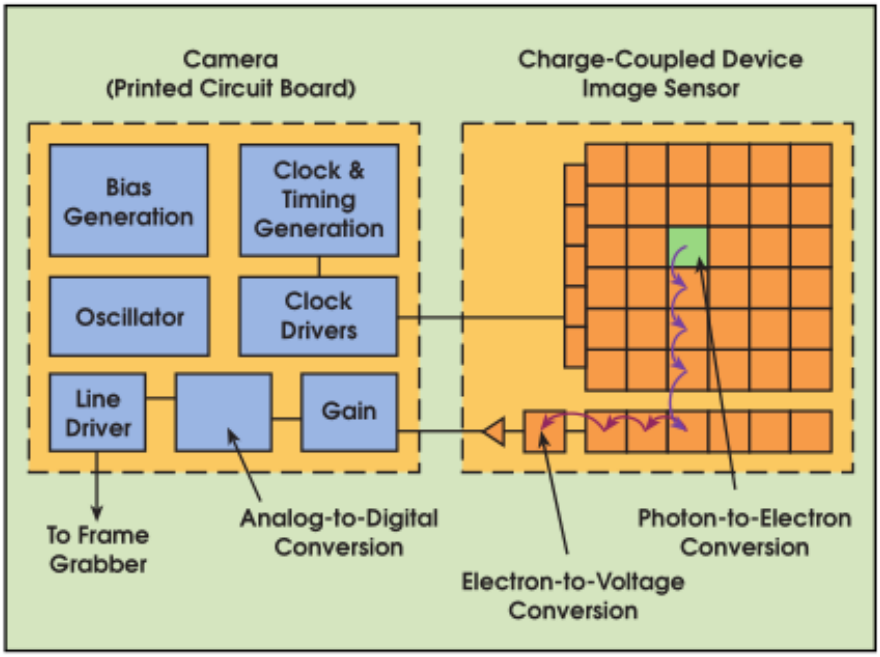

Figure 23: The schematic of a CCD camera sensor.

SHUTTER TIME: This is the duration of the exposure of the sensor chip to the light incident. If the test is static, low shutter time is feasible. However if the test is dynamic, high shutter speeds must be used. Depending on how dynamic the test is, the shutter speed must be adjusted. Inadequate shutter time causes blurring in the images resulting in inaccurate representation of the surface in the images.

Figure 24:Camera and LED Illumination

Figure 25:High speed cameras [23]

Lenses

Lenses greatly influence the capabilities of the Digital Image Correlation setup. While their key function is to focus and distinctly resolve light rays from the desired area on the specimen on to the CCD chip, the choice of the lens also determined what field of view can be effectively monitored. A key parameter of lenses is its focal length. Choosing the lens of the right focal length for a given field of view is vital for a successful measurement.

20 mm Lens 100 mm Lens

Figure 26: Lenses [24]

FOCAL LENGTH: The focal length is the distance between the lens and the camera's sensor when the object, which is the source of the light, is at infinity with respect to the lens. For a thin lens, with light parallel to the optical axis entering it, ideally, the region from which these light rays originated is resolved only when the sensor is in the focal plane of the given lens – camera system.

MEASURING DISTANCE: For two-dimensional measurements, the measuring distance is that distance from the specimen to the camera chip where the best focus is obtained. For a three-dimensional setup, this is dependent on the distances obtained from stereo imaging and triangulation principles. The optimum measuring distance is generally characteristic to a given combination of camera resolution, the distance between the two stereo cameras, the angle they make with the center line between them, focal length of the lens and the field of view.

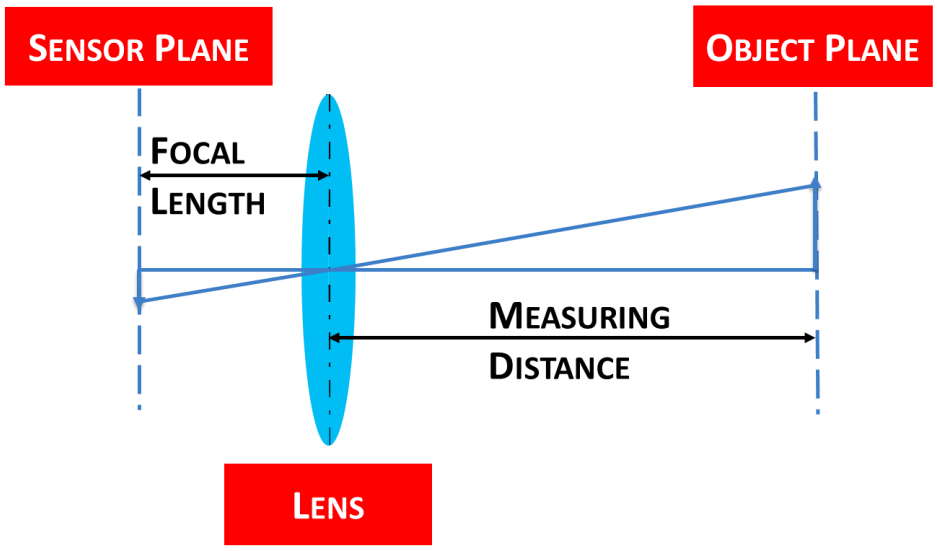

Figure 27: Focal length and measuring distance

DEPTH OF FIELD (DOF): Ideally, focus of the object obtained is planar and captures distinctly only a plane from the object. However, in reality the space in front and behind the object appears to be in focus and is called the depth of field. The depth of field is dependent on the f-stop and the magnification used [10]. In lens systems, an aperture diaphragm is generally provided right in front or behind the lens to control the operational diameter of the light inlet and helps control the depth of

field. More open the aperture, more light is allowed through, causing blurring and it costs depth of field. At its closed position, it allows some light but provides the maximum depth of field.

$$f - stop = \frac{focal\ length}{diameter\ of\ aperture\ diaphragm} \tag{17}$$

FIELD OF VIEW (FOV): Also called the angle of view, this is the extent of the scene that can be seen by the lens camera system and transform this image onto the sensor for a given focal length and a measuring distance. For the same measuring distance between the lens and the object, as the focal length of the lens gets larger, the field of view also gets smaller. However, higher magnifications of the object can be obtained.

OTHER HARDWARE COMPONENTS

ILLUMINATION: White light is the used for illuminating the specimen. Ample lighting of the specimen must be ensured as this is crucial for proper representation of surface through the image grayscale values in correlation algorithm. Lighting is typically using Light Emitting Diode (LED} or Halogen sources. Polarizers may also be used with lighting to control the quality of illumination of the specimen.

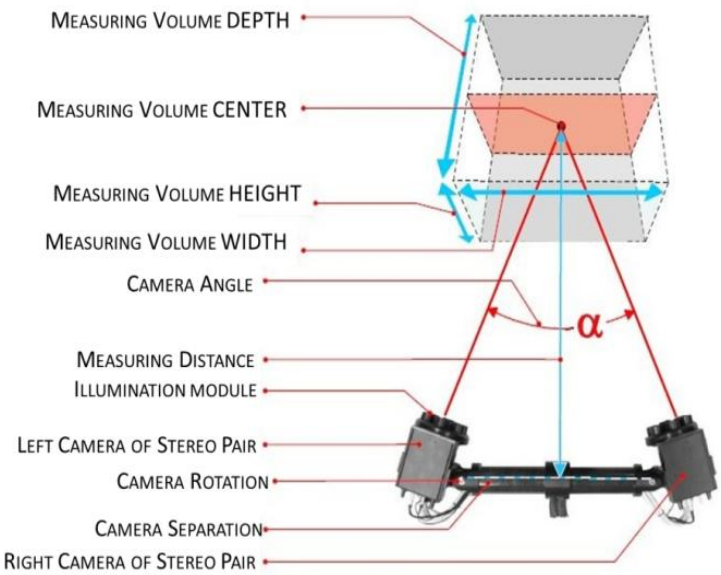

Figure 28: Measuring volume in 3D DIC [24]

POLARIZERS & FILTERS: Light has both phase and amplitude associated with it. Normally, visible light has waves in all phases. Polarizers assist in filtering out light of one kind of polarization only. Typical use of polarizers is to eliminate glare in the acquired images. Filters maybe used to selectively allow some component frequencies of white light into the lens.

CAMERA SUPPORT: The cameras are mounted on a camera bar. This camera bar can be mounted on a tripod with a tripod head. This mounting system helps provides stability to the camera system with flexibility in orientation. It can also be mounted on an optical table with a two directional motion control.

SPECIMEN PREPARATION

Surface contrast is at the heart of implementing Digital Image Correlation. Contrast from the surface is captured in the acquired images, effectively transferring information about specimen surface to the correlation algorithms. During loading, the changes in the surface of the specimen results in change of the surface pattern. Correlation of the intensity fields obtained from this surface contrast in the images before and after deformation of the surface can be used to find the displacements on the surface.

Surface contrast can be a stochastic or a regular pattern of dramatically varying intensities. An optimum surface contrast will have a Gaussian distribution of gray values without many extreme grays viz. black or white [25]. The size of patches of contrast change is directly related to the field of view. From user experience, a single dark patch (surrounded by light background) on the specimen must occupy about 5 pixels for successful correlation in the images acquired from the 5-megapixel sensor. Methods to impart contrast to the specimen surface is open ended and can be improvised or devised as the testing condition demands.

WHAT IS A GOOD SURFACE PATTERN?

The key function of the surface pattern is to carry surface deformation information form the real test to the computer image. The quality of the speckle pattern influences the accuracy of the measured deformation. Many assessments have been performed in the literature using computer generated speckle patterns. A known displacement is applied to computer generated speckle patterns and DIC is performed on the initial and the displaced patterns. When every other parameter in the algorithm is kept constant and different speckle patterns are tested with known displacements, the influence of the surface contrast is are clearly seen in the measured displacement fields [26]. There are two major criteria that qualify a good surface pattern for a successful DIC measurement:

a. Intensity Distribution of Speckles:

A Gaussian Distribution that does not substantially include extreme values of the gray scale is appropriate for DIC [25]. Most monochromatic digital cameras have 8-bit sensors. So, every pixel has assigned a value in the range [0,255]. Image processing tracks the grayscale values of these pixels, and not the material points themselves. To provide good identification to the surface points in the image, the pixel grayscale values must be well-distributed and varied. To achieve this, a speckle pattern without localization of light or dark spots must be obtained on the surface. It must vary densely. [27] specify use of the entire dynamic range of the 8-bit camera without saturation of any one particular value of the grayscale. To evaluate a speckle pattern's feasibility quantitatively, Pan et al.[26, 28, 29] propose:

i. Mean Intensity Gradient: A global quantitative measure of the pattern's intensity variation.

ii. Sum of Square of Subset Intensity Gradient (SSSIG): A subset level local measure of the pattern's intensity variation

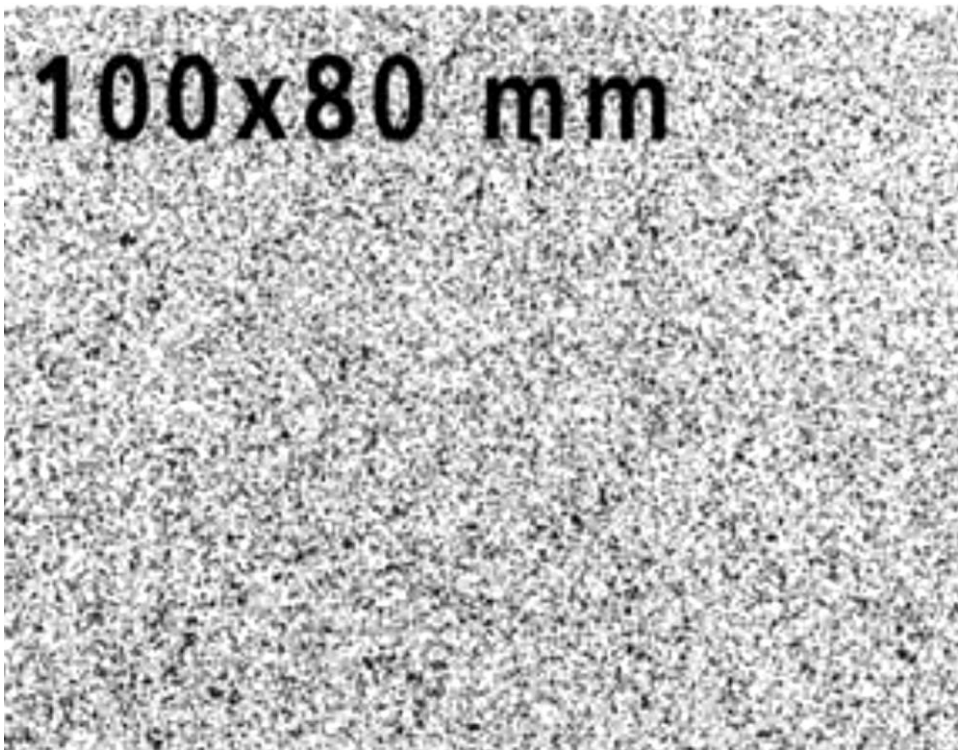

Figure 29: Ideal pattern density; 100 x 80 mm FOV [30]

GOM recommends a dull, non-reflective stochastic pattern with good contrast implying a good distribution of dark and light grays [30].

b. Size of Speckles relative to Field of View:

Lecompte et al. [31] perform an empirical study on a reference speckle pattern with three different levels of zooms to determine how the size of the speckles influences the displacement measured. Mean Speckle Size is used as a quantifying parameter for the size of the individual blotches of black speckles on flat white paint.

A close correlation is found between the size of the speckles and the size of the subsets used in tracking the surface pattern. For a small subset of 13 x 13 pixels, a mean speckle size of 3 pixels gave the most accurate displacements. Similarly, for 23 x 23 pixel and 33 x 33 pixel subsets, speckles of average size equal to or greater than 10 pixels gave best accuracy. GOM gives a relative size of the speckles recommendation in the ARAMIS manual. It is recommended that the applied pattern should be adapted to the field of view, the resolution of the camera and used subset size [30].

CALIBRATION

Panels and scale bars which have fixed distances distinctly marked on them serve as calibration artifacts (Figure 30). Ideally, a panel or a scale bar which completely fills up the selected field of view is chosen for this process. Images of various orientations of the artifact with the markers clearly visible are captured using both cameras Table 4. The orientation and the distance in each image are correlated and the measuring volume is then back calculated by the system. The region of interest on the specimen must be completely within this volume for a successful measurement. A two-dimensional measurement can be performed without calibration. When this is the case, a length scale is defined within the image in post processing before implementing the correlation algorithm.

Figure 30: Typical Calibration Artifacts [30]

Feasibility and Noise Check

Noise is induced in the system from image sensors and in the correlation algorithm. Once the image acquisition system is setup and calibrated, to quantify system noise for the given configuration of the system, two images of specimen are obtained one after without any load applied on the specimen and correlation is performed on these images. We know that the specimen's configuration was not changed at all from the first acquisition to the second. Hence, ideally no strain must be observed. Any displacement or strain observed in the system after correlation qualifies as system noise.

Table 4: Steps in Calibration using a patterned calibration artifact [24]

Group 1: Front, Middle and Back of measuring volume upright images

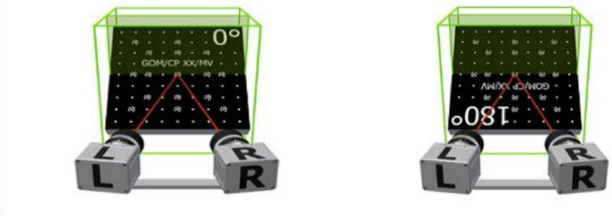

Group 2: Tilt orientations

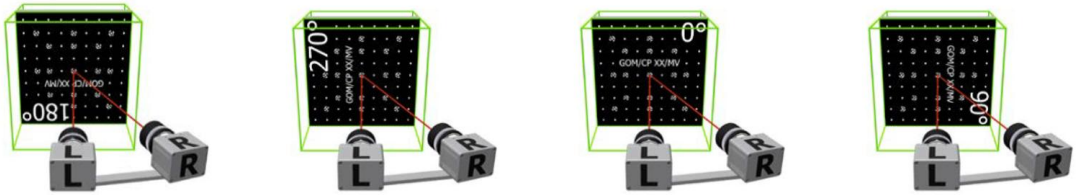

Group 3: Left camera perpendicular Orientations

Group 4: Right camera perpendicular Orientations

TESTING & IMAGE ACQUISITION

The testing procedure of the specimen is planned out. The frame rate of image acquisition is determined if using automated image acquisition. If high speed cameras are used, up to 200,000 images can be captured per second. Advances in camera hardware technology can improve this further. Image acquisition can also be manually triggered. A typical DIC measurement follows the following procedure:

1. Pick the region of interest (ROI) on the specimen (in a laboratory) or the structure (in the field)
2. Ensure grease, dirt and rust free surface and ample surface contrast
3. Pick lens such that:
    - It resolves best the surface contrast at the working distance
    - The given region of interest stays in the lens's field of view for the entire time of monitoring
4. Adjust the focus of the lens-camera system so as to obtain sharp image of the region of interest
5. Adjust f-stop number of the aperture such that:
    - Sufficient depth of field is obtained to keep the specimen in focus throughout the time of monitoring
    - Enough light enters the lens and onto the sensors such that the surface contrast is distinctly visible
6. Estimate the image acquisition rate and adjust shutter time depending on the displacement rate or the strain rate of the test
7. Apply load while acquiring images (in-situ) or apply load and release load and then acquire images (ex-situ)
8. Post-process the images to extract displacement and strain fields at the deformed configurations of the region of interest.
9. If connected with a loading machine, the DAQ records the load data simultaneously and is saved into the DIC data.

2.5 DIC ALGORITHMS

Sutton and his research team members devised a procedure to perform digital image correlation in 1983 [8] The procedure has seen many improvements over the years. In this section, some salient algorithms of DIC available in literature are presented. While the basic scheme of Digital Image Correlation, which involves acquiring images of a specimen with a pronounced surface contrast at a reference and a deformed configuration, estimating the deformation parameters and

differentiating the obtained deformation field to obtain the strains is the same, the way the displacement mapping is chosen and strain is computed from the obtained displacement field has seen a lot of improvement.

2.5.1 SURFACE PATTERNING METHODS

MACRO SCALE METHODS

COTTON SWAB TECHNIQUE: This is generally used when part of a much larger structure is under investigation. The surface is cleaned of grease, rust and dirt. A thin layer of white paint is sprayed on to surface and regularly spaced black dots are applied on to the surface of the area of interest by dabbing a cotton swab dipped in black paint.

STENCIL & MESH TECHNIQUE: Generally used when the field of view is ~1 meter. Surface is cleaned and a thin layer of white paint is sprayed on it. A mesh is placed on the surface and black paint is sprayed and the mesh is removed. A grid of regular black lines with white background is thus realized. The thickness of these lines can be varied by using meshes of different thickness. If the situation demands, a custom made stencil can be crafted from corrugated cardboard and can be used just like the mesh.

SPECKLE PATTERNING TECHNIQUE: This is the most commonly implemented surface patterning technique and can be implemented for a wide range of field of views from ~1 meter to the centimeter regime. The surface is first prepared by getting rid of any grease, dust or rust. A thin layer of white paint is sprayed on to the surface of the specimen. Then, black paint is sprayed such that only tiny speckles of paint settle on the specimen. This is achieved by holding the spray tip at an angle. A fine layer of black speckles is obtained on the layer of white paint. The speckle sizes can be manipulated by sputtering the black paint instead of spraying it. In some cases a hole can be drilled right at the nozzle tip to increase the size of the dots for larger fields of view so that the dots are about 5 pixels large. This technique is versatile and can be implemented with minimum resources.

MICRO SCALE METHODS

AIR BRUSH TECHNIQUE: This technique is appropriate for FOVs in the regime of millimeters and micrometers. It offers selection of particle sizes that will be deposited on the surface of the specimen. Powder of the required kind is suspended in a natural solvent. The tank of an air brush is filled with this suspension and pumped using a compression pump. At an optimum

distance along the spray, the powder is deposited on the surface of the specimen leaving behind a stochastic pattern on the material surface.

PARTICLE DISPERSION TECHNIQUE*:* This technique is for patterning specimens when FOVs are in the micrometer range and was developed by Jonnalagadda et al. in their experiments. The specimen is free suspended at the top of a cylinder with the surface of interest facing into the cylinder. This cylinder has inlets for compressed air at the bottom [25]. Slightly above this is inlet for the patterning powder. The powder generally comprises of micro particles. The compressed air brings the powder up to the specimen. van der Waals forces and static charges cause the adhesion of these particles to the specimen. The size of the deposited particles can be controlled using sieves of filter between the sample and the inlets. Different densities can be obtained by changing the distance of the specimen from the inlets and varying the number of times the particles are sprayed. This technique is useful for specimens when they are susceptible to mechanical damage with other techniques.

ETCHING: This is technique used to expose the microstructure in metals and alloys. When the micro structure is revealed, enough surface contrast can be obtained to perform a DIC measurement. In order to expose the microstructure, the region of interest on the specimen is grounded and polished. Then, it is treated with an appropriate etching agent. This technique was used in Chapter 5 to expose grains and DIC measurement was successfully performed.

2.5.2 DISPLACEMENT MAPPING AND STRAIN CALCULATIONS

Two main approaches for displacement field estimation have been put forth by various researchers [32-35]. There are subset based algorithms which perform correlation in the image piece by piece. Then there are the continuum algorithms implementing transformation to B-Spline parameter space or utilizing finite elements meshing techniques in each image. Each method has its own advantages and disadvantages.

SUBSET BASED DISPLACEMENT ALGORITHMS

The key feature of the subset based methods is displacement is estimated for the center of deformed subsets one by one and assembled together for all subsets in the image to obtain the full field displacement field [9, 10, 13, 14, 28, 36].

DISPLACEMENT MAPPING FUNCTIONS

Consider just one subset from the deformed image. The material corresponding to this subset undergoes a certain displacement ξ in the x direction and η in the y direction in case of in-plane displacements. A material point with initial

coordinates (x, y) transforms to (x′, y′) by this displacement. The exact nature of the displacement (ξ, η) is not known and a certain mapping or shape function is simply assumed to approximate the underlying displacement. The parameters of this displacement are obtained by optimization. The objective of the optimization process is to guess values for the unknowns in the assumed displacement by maximizing the similarity between the considered subset and all subsets in the reference image. A first order or a second order shape function can be used as reasonable assumption for the unknown displacement.

First Order Shape $x_i' = x_i + [u + u_x\Delta x + u_y\Delta y]$

Function: $y_j' = y_j + [v + v_x\Delta x + v_y\Delta y]$

Second Order Shape $x_i' = x_i + \left[u + u_x\Delta x + u_y\Delta y + \frac{1}{2}u_{xx}\Delta x^2 + \frac{1}{2}u_{yy}\Delta y^2 + u_{xy}\Delta x\Delta y\right]$

Function: $y_j' = y_j + \left[v + v_x\Delta x + v_y\Delta y + \frac{1}{2}v_{xx}\Delta x^2 + \frac{1}{2}v_{yy}\Delta y^2 + v_{xy}\Delta x\Delta y\right]$

WHERE:

u, v	Unknown displacements in X and Y directions of subset center	
u_x, u_y, v_x, v_y	Unknown first order displacement Gradients	
$u_{xx}, u_{yy}, u_{xy}, v_{xy}$	Unknown second order displacement Gradients	
Δx	$= x_i - x$	(x: reference subset center x coordinate)
Δy	$= y_j - y$	(y: reference subset center y coordinate)

Table 5: Displacement variables to be optimized in correlation process

SHAPE FUNCTION	VARIABLES TO BE OPTIMIZED	# OF VARIABLES
First Order	$\boldsymbol{P} = [u, v, u_x, u_y, v_x, v_y]$	6
Second Order	$\boldsymbol{P} = [u, v, u_x, u_y, v_x, v_y, u_{xx}, u_{yy}, u_{xy}, v_{xy}]$	10

Use of second order displacement mapping was introduced by Lu and Cary [14] and has found wider application compared to other polynomials as it accounts for nonlinear deformation including translation, rotation, shear, normal strains and combinations of these in reasonable computing time where a first order shape function would not be able to accurately estimate the nonlinear displacement components [13, 14, 37].

CORRELATION CRITERIA

A certain correlation criterion defines the cost function of the optimization process and accounts for the best match of the gray scale value with the displacement mapping variables. These variables are represented by vector ***P*** **(**Table 5**).** If a first order displacement function is assumed, six unknown values of the components of the displacement function are guessed to maximize this cost function (to maximize similarity or minimize the difference) effectively looking for the best match for a deformed material point in the reference image. Digital Image Correlation owes its name to this key step in determining the displacement fields [38]. Chu et al. [9] describe the use of the cross correlation coefficient. Its discrete domain adaptation is shown in [13]. Least squares correlation coefficient has also been used [38] widely.

1. Cross Correlation (CC)

$$C = \sum f_i(x,y) g_i(x,y,\boldsymbol{P}) \tag{18}$$

2. Sum of Squared Difference (SSD)

$$C = \sum (f_i(x,y) - g_i(x,y,\boldsymbol{P}))^2 \tag{19}$$

These correlation coefficients compare two subsets (a) whose displacement we are looking for: g (b) another subset from the in the reference image: f and compute a value in range [0,∞]. (b) is done for every subset in the reference image and a *correlation field* is obtained. At the global maximum of this correlation field, the best match for (1) exists. The values of **P** that correspond to this best match are the displacement coefficients we are looking for. When this is repeated for every subset in the whole deformed image, we get a displacement field.

In practical implementation of DIC, pixels representing the same material point will not have the same grayscale values in the reference image and the deformed image. This change is caused by the variations in the intensity of the illumination received at different points on the surface. The intensity may also vary with time. The reflectivity of the surface changes during the test due to strain or change in surface roughness. The same point on the surface of the material will have different grayscale if simply looked at from a different angle [38]. The changes in intensity can be a linear variation, an offset to the values or a combination of both in the reference images. The correlation coefficients can be affected by light fluctuations. This in turn affects the reliability of the measurements obtained by the correlation procedure. This calls for a modification of the correlation criteria used in the implementation of DIC. Normalized correlation coefficients are insensitive to linear changes in

illumination intensities. Zero mean correlation coefficients are insensitive to offset changes in illumination intensities. Combining them together makes the correlation coefficient account for both of these types of illumination changes [13, 28]. Pan in his work [28] proves that all the correlation criteria are equivalent to each other and yield similar results.

REGULARIZATION

Displacement is discretely calculated at the subset centers and this data is used to form the full field displacement. Regularization introduces taking information from neighboring subsets when estimating the unknown displacement variables for a subset in the correlation process. An extra term is added to the correlation coefficient with a weight and the new objective function for optimization is:

$$C_{Regulariged} = C + \lambda R \tag{20}$$

Where:

C: Chosen Correlation Coefficient

R: Regularization term

λ: Weight for regularization

Cofaru et al. [39] propose regularization based on Geman-McClure robust function. It adaptively decides the influence of the 8 neighboring subsets' displacement variable values on the current subset's displacement. A first order displacement mapping is assumed.

$$R = \sum_{i=1}^{6} \sum_{j \epsilon N_i^8} \rho(r_{ij}, \sigma_i(r_{ij})) \tag{21}$$

$\rho(r, \sigma) = \frac{r^2}{(r^2+\sigma)}$ (Geman-McClure robust function)

σ_i: Weight based on standard deviation of the difference between current and neighboring subsets' displacement variables

r_{ij}: Difference between displacement variables of current and neighboring subset

This kind of regularization modifies the displacement of the current subset that is being regularized. More the difference between the current and the neighboring subsets' displacement values, higher the influence of regularization. This is ensured by the weights based on the standard deviation of the difference in the values.

SUBPIXEL DISPLACEMENTS

Pixel Grayscale Interpolation: At the images' pixel level, one subset of M X N pixels theoretically represents the material point at the center of the subset. In reality, however, a pixel covers a region of material and not just one material point. To account for all the material points in between and extend the measurement resolution to deeper than the pixel level, grayscale values are interpolated to get a continuous field of grayscale values within the subset [9, 13, 14, 40]. Polynomials are used to interpolate the discrete grayscale values into a continuous field. Lower order polynomials do not give a very smooth fit but retain the spatial density of the original grayscale values. Higher order polynomials will provide very smooth fits but reduce the originally acquired grayscale content [9]. Hence when using high order polynomials for sub-pixel interpolation, it is important to oversample, i.e. use high- resolution image sensors so that the spatial frequency in the fit is reliably accurate. Up to 40% systematic error was found in strain measured from the displacement fields computed using linear grayscale interpolation.

Based on computation speed and accuracy, Schreier et al. [13, 41] recommend the use of cubic spline interpolation and when speed is not a concern, quintic spline interpolation with a low pass filter. Lu and Cary [14] also use a bicubic spline interpolant in their DIC algorithm. [42] discuss performance of a family of interpolation functions based on digital filter form of bicubic spline interpolation. Bicubic Spline Interpolation is a piecewise interpolation scheme using a third order polynomial that takes the grayscale values from a square of four pixels and interpolates grayscale values for the material points in between. The general form of the interpolant is given in (below). The interpolation is used on both the reference and the deformed subsets.

$$f(x,y) = \sum_{m=0}^{3}\sum_{n=0}^{3} \alpha_{mn} x^m y^n \tag{22}$$

Displacement Variables Optimization: Many subpixel level displacement algorithms have been developed over the years. Most of these algorithms depend on integer pixel level displacement for initial guesses as provided by search methods. The prominent ones discussed in the literature that have been successfully applied for at least translational motion are presented below:

a. Newton Raphson Method [14, 39, 40, 43, 44]

To present this method, we pick the sum of squared difference correlation criterion.

$$C = \sum (f_i(x,y) - g_i(x,y,\boldsymbol{P}))^2$$

WHERE:

p: Material point $f_p(x,y)$: Grayscale value of point p in reference subset

S: Subset $g_p(x,y,\boldsymbol{P})$: Grayscale value of point p in deformed subset corresponding to $\boldsymbol{P}$

In the correlation field obtained from this coefficient, the gradient of this field converges to zero at the minimum. The gradient is given by the Jacobian of the correlation field. The Newton-Raphson method iteratively improves an initial guess of $\boldsymbol{P}$ i.e. $\boldsymbol{Po}$, using the Jacobian and Hessian matrices computed for the correlation function **C**. The correction for the *k*th guess is given by:

$$\boldsymbol{P}_k = \boldsymbol{P}_{k-1} - \frac{\nabla \mathrm{C}(\boldsymbol{P}_{k-1})}{\nabla\nabla \mathrm{C}(\boldsymbol{P}_{k-1})} \tag{23}$$

WHERE:

$\boldsymbol{P}_k$ kth correction of the displacement variables vector

$\boldsymbol{P}_{k-1}$ k-1th set of values of the displacement variables vector

$\nabla \mathrm{C}(\boldsymbol{P}_{k-1})$ Jacobian of the correlation coefficient; First derivatives

$\nabla\nabla \mathrm{C}(\boldsymbol{P}_{k-1})$ Hessian matrix of the correlation coefficient; Second derivatives

When a correlation criterion that accounts for changes in illumination is used, the grayscale at a given material point can be assumed to be the same in the reference and the deformed images can be assumed to be the same; i.e. $f(x,y) = g(x,y,\boldsymbol{P})$. Also, by assuming that the initial guess vector **Po** is close to the solution, the computation of the Hessian matrix is made less cumbersome by using an approximation as used by [14, 36].

$$\begin{aligned} \nabla\nabla \mathrm{C}(\boldsymbol{P}) &= \left(\frac{\partial^2 C}{\partial \boldsymbol{P}_i \partial \boldsymbol{P}_j}\right)_{\substack{i=1:length(\boldsymbol{P}) \\ j=1:length(\boldsymbol{P})}} \\ &\cong \left(\frac{2}{\sum_p f_g^2} \sum_p \frac{\partial g_p(\boldsymbol{P})}{\partial \boldsymbol{P}_i} \frac{\partial g_p(\boldsymbol{P})}{\partial \boldsymbol{P}_j}\right)_{\substack{i=1:length(\boldsymbol{P}) \\ j=1:length(\boldsymbol{P})}} \end{aligned} \tag{24}$$

The integer pixel displacement value for the subset is used as the initial guess for this iterative optimization method.

b. Curved Surface Fitting Method [45]

An optimal correlation criterion is chosen and used to compute the correlation coefficient at every subset center in the deformed image. A fitting window is considered in the grid of subset center points and in each window, a quadratic polynomial is used to fit a surface through the correlation coefficients.

$$C(x,y) = a_0 + a_1x + a_2y + a_3x^2 + a_4xy + a_5y^2 \quad (25)$$

That way, every point in between the centers of the individual pixels will have a correlation coefficient associated with it. When the correlation function reaches its maximum value in the interpolated correlation field, the best match is found. The location of the maximum is found by differentiating this fitted surface and setting it equal to zero and solving for the x and y coordinates.

$$\frac{\partial C(x,y)}{\partial x} = a_1 + 2a_3x + a_4y = 0$$

$$\frac{\partial C(x,y)}{\partial x} = a_2 + a_4x + 2a_5y = 0$$

$$x = \frac{2a_1a_5 - a_2a_4}{a_4^2 - 4a_3a_5} \qquad y = \frac{2a_2a_3 - a_1a_4}{a_4^2 - 4a_3a_5}$$

c. Gradient Based Method [45]

Displacement in every subset is assumed to be translation given that the subsets are small enough. A pixel level and subpixel level translation is used as displacement mapping. A correlation criterion that allows assumption of constant grayscale value for a given material point is used to find the subpixel level match and thus the displacement mapping is obtained.

d. Iterative Gradient Based Method [45, 46]

No explicit correlation function is used in this method. Optimization is done for the displacement mapping variables in vector **P** based on the assumption that grayscale value of a material point stays the same in the reference and in the deformed image. The objective function for the optimization is of the form:

$$f(x,y) = g(x + u + u_x\Delta x + u_y\Delta y, y + v + v_x\Delta x + v_y\Delta y)$$

$$\boldsymbol{P} = (u, v, u_x, u_y, v_x, v_y)$$

The integral level displacements are found first using a cross-search method [46]. They serve as initial guess for **P** of the form $[U\ 0\ 0\ V\ 0\ 0]$ for Newton's iteration scheme to obtain the subpixel level displacements.

e. Artificial Neural Network [47]

Artificial neural networks are electronic circuit architectures inspired by how neurons in the brain work. Networks are modeled to represent a data set by exposing them to input and the corresponding output. The weights of the nodes in the

network are adjusted as the network 'learns' to give the desired output for a given input. Multilayered perceptron (MLP), a 'trained' network was used for Digital Image Correlation in [47]. The network architecture itself stored the displacements. 24 x 24 pixel subsets in the image of sample were given as the input. A known, random subpixel displacement was applied to these subsets externally and it was given to the network as the required output thus training the network to modify the displacement vector stored in it according to the reference and the deformed subset. Training was done with 10,000 examples. In-plane displacement for a thermally stressed plastic quad flat pack microelectronic device was successfully obtained by this method in [47]

f. Genetic Algorithm [48]

Genetic algorithm is a random search method that is inspired by the biological processes of life, reproduction and death. The displacement variables in **P** are encoded in the form of genes into chromosomes. Several chromosomes together make a population. The fitness of each chromosome is evaluated based on its genes by evaluating the objective function. In DIC, the objective function is the minimization of the difference between a given deformed subset and the subsets in the reference image. The chromosomes with the worst fitness are killed and the pairs of the remaining chromosomes are selected as parents and their genes are cross-linked to create offspring chromosomes to fill the population to initial or a certain specified number. A fraction of the genes are then mutated to avoid getting stuck at a local extremum. The chromosomes are again evaluated for fitness and the process is repeated until the genes converge to the required accuracy. Since the values of displacements u, v and displacement gradients u_x, u_y, v_x, v_y are in different orders of magnitude, when mutating and crosslinking to create offspring, the orders have to be adjusted by scaling or crosslinking displacement genes to displacement genes and gradient genes with gradient genes. The number of chromosomes required to be initialized at the beginning of the process, the chromosome population that has to be maintained over the operation of the optimization, the exact fraction of mutation of genes that take place and the subset size needs to be optimized for that specific application for quick convergence. Using this algorithm, one-dimensional and two-dimensional strain was successfully measured in [48]

g. Particle Swarm Optimization Method [49]

PSO is an artificial intelligence algorithm generally used in robotics. A cross search based integer pixel displacement is used to provide initial guess for the core subpixel displacement algorithm. Several particles at various positions within a neighborhood of the integer pixel displacements are initialized. They are also assigned some initial velocity. The formulation for this method is as follows:

$$v^{k+1} = wv^k + c_1 rand(pbestp^k - p^k) + c_2 rand(gbestp^k - p^k)$$

$$p^{k+1} = p^k + v^{k+1}$$

Where:

p	particle position	v	particle velocity
w	inertia weight	k	1,2,3,…
$pbestp$	particle's personal best position	$gbestp$	global best position
c_1	particle swarm's ability of self-examination	c_2	particle swarm's ability of learning from colony

The value of *w* determines how quickly the swarm of these particles can jump from the local extremum to the global extremum and how steadily they can stay at the local point for speedy convergence. In DIC, this swarm optimization specifically applies to finding the global extremum in the correlation field between a deformed subset and the reference subset field. The fitness of every particle is computed based on the correlation coefficient value associated with it. Based on this fitness pbestp and gbestp is initialized. The velocity is recomputed and the new particle position is calculated again. The fitness of all particles is now computed again. This is a cyclic process till the positions of the particles converge to maximum correlation with a given accuracy.

h. Fourier Domain Approach [50]

The first principles of this method are mainly obtained from the spectral fringe pattern method for determining displacements [51]. The image of the patterned specimen is broken down into subsets and Fast Fourier Transform (FFT) is performed on the subsets from both the reference and deformed images. Correlation is performed by finding a resultant spectrum using these two subsets and then FFT is performed again to get the actual displacement vector. This method from [51] has seen many improvements and this method has also been integrated with many full field implementations of DIC. At the subpixel level however, the basic algorithm still involves analysis of grayscale values of a small region of pixels in the acquired images. According to optical flow assumptions, the displacement from the reference image to the deformed image can be expressed as:

$$g(\boldsymbol{X}) = f(\boldsymbol{X} + u) + b(\boldsymbol{X}) \tag{26}$$

WHERE:

g	Grayscale values of deformed image
f	Grayscale values of reference image

u Displacement field on material from reference to deformed

b Noise in system and implementation

Linear combination of some basis functions is assumed for displacement mapping between the reference and deformed images as shown in (27). Assuming the displacements are small enough to use a first order Taylor's expansion, (28) is the objective function to be optimized to find the optimum values of amplitudes v_i .

$$\boldsymbol{v} = \sum_i \eta_i(\boldsymbol{X}) v_i \tag{27}$$

$$\Phi(\boldsymbol{v}) = \iint [g(\boldsymbol{X}) - f(\boldsymbol{X}) + \boldsymbol{v}(\boldsymbol{X}).\nabla g(\boldsymbol{X})]^2 dx \tag{28}$$

The complex conjugate of a reference subset is computed using Fast Fourier Transform (FFT), multiplied with the FFT of the deformed subset being considered and the inverse FFT is obtained to find the correlation between the subset in the reference and the deformed image (29). [50] [52].

$$f \circ g = lFFT^{-1}[\overline{FFT(f)} FFT(g)] \tag{29}$$

WHERE:

l The number of pixels along the edge of the square subset

$\overline{FFT(f)}$ Complex conjugate FFT of reference grayscale values (over line)

$FFT(g)$ FFT of deformed grayscale values

Integer pixel level displacement is first found using integer pixel level FFT based cross-correlation or a coarse-fine search method [50]. Grayscale values in the subset are interpolated using subpixel interpolation. Either the shift or the modulation operator helps perform non-integer level correlation.

CONTINUUM BASED DISPLACEMENT MAPPING

The subset method involves finding displacement mapping parameters **P** individually for all the small regions called subsets over the whole region of interest on the specimen and putting them together to get the full field displacement field. Unless a regularization term is used as in [39] or compatibility with neighboring subsets is explicitly considered as done by [53], the displacement continuity will not be accounted for and degrades the accuracy of the displacement field calculated [35, 54]. Furthermore, the discrete displacement fields obtained from the subset method need to be smoothened before reliable strains can be calculated from it [35]. In contrast to the discrete, discontinuous displacement tracking points as defined by

subset based algorithms, the continuum based algorithms define a single finite element mesh [35] or a parameter space [54] for the whole region of interest image where all pixels are considered at the same time for the correlation process [54].

FINITE ELEMENT MESHING BASED CONTINUUM DIC

In this approach, the whole region of interest is assigned elements and nodes similar to the Finite Element Methods in computational mechanics [35]. An element represents a region of material points. The displacement of the material points within the element are related to the displacements of the nodes of the element by (30).

$$.u(x,y,\boldsymbol{P}^e) = \sum_{i=1}^{m} N_i(x,y)u_i$$
$$v(x,y,\boldsymbol{P}^e) = \sum_{i=1}^{m} N_i(x,y)v_i \tag{30}$$

$\boldsymbol{P}^e = [u_1 v_1, \dots, u_i v_i, \dots, u_m v_m]$ m: Number of nodes in the element

$N_i(x,y) = Shape\ function\ of\ the\ element$

A correlation criterion is used to find the optimal values of displacement at all the nodal points by finding the best match for elements in the deformed image and the undeformed image. Using a sum of squared correlation coefficient, the objective function can be defined as [35]:

$$C = \sum_{e \in E} \sum_{p \in e} \left(f_p - g_p(\boldsymbol{P}^e) \right)^2 \tag{31}$$

WHERE:

e: element p: point in element

E: set of all elements $\boldsymbol{P}^e$: element displacement vector

The minimum of the objective function (31) is found by setting its gradient to zero.

$$\nabla C = \left(\frac{\partial C}{\partial \boldsymbol{P}_{global,i}} \right)_{i=1,2n}$$

$$= -2 \sum_{e \in E} G^T \sum_{p \in e} \left(\frac{\partial g_p(\boldsymbol{P}^e)}{\partial \boldsymbol{P}_{global,\boldsymbol{j}}} \left[f_p - g_p(\boldsymbol{P}^e) \right] \right)_{j=1,2m} = 0 \tag{32}$$

WHERE:

G: Nodal assembly matrix

$\boldsymbol{P}^e = G\boldsymbol{P}_{global}$ $\boldsymbol{P}_{global} = [u_1 v_1, \dots u_i v_i, \dots, u_n v_n]$

To find the roots of the Jacobian in (32), Newton-Raphson method of the form (33) is used [35].The Hessian matrix required for the process is computed by the equation (34) which is an approximation for the hessian matrix with the assumption that the initial guess **P**global,o is close to the solution [36].

$$\nabla\nabla C\left(\boldsymbol{P}_{global_o}\right)\left(\boldsymbol{P}_{global}-\boldsymbol{P}_{global_o}\right)=-\nabla C\left(\boldsymbol{P}_{global_o}\right) \tag{33}$$

$\boldsymbol{P}_{global_o}$:Initial guess of the global displacement vector for the Newton-Raphson iteration

$$\nabla\nabla C = \left(\frac{\partial^2 C}{\partial \boldsymbol{P}_{global,i}\partial \boldsymbol{P}_{global,i}}\right)_{\substack{i=1,2n\\ i=1,2n}}$$

$$= \sum_{e\in E} G^T\left\{2\sum_{p\in e}\frac{\partial g_p(\boldsymbol{P}^e)}{\partial \boldsymbol{P}^e{}_h}\frac{\partial g_p(\boldsymbol{P}^e)}{\partial \boldsymbol{P}^e{}_k}\right\}G \tag{34}$$

Initial guess $\boldsymbol{P}_{global_o}$ is generally set to zero for small deformation and large rigid body translation. For large deformations, the initial guess can be estimated by interpolation with user-defined functions. The approach described above is the one taken by [35]. Other important finite element approach works in the literature are [55] where the authors implement DIC with Q4-P1 shape functions. Fourier decomposition is used for subpixel intensity interpolation.

B SPLINE PARAMETER DOMAIN BASED CONTINUUM DIGITAL IMAGE CORRELATION

In this approach, a B-Spline parameter domain is introduced [54]. Each pixel location (x,y) in the undeformed **M x N** pixels region of interest is converted to a location (α,β) on this domain which is a unit square matrix and hence $0 \le (\propto,\beta) \le 1$. Figure 31 shows the schematic of the method. The mapping is given by:

$$\alpha = \frac{x}{N-1} \qquad\qquad \beta = \frac{x}{M-1} \tag{35}$$

The *x* and *y* displacement at (α,β) in this B-Spline parameter domain is given by (36).

$$\begin{aligned}\boldsymbol{u}(\alpha,\beta) &= \sum_{i=0}^{n}\sum_{j=0}^{m} N_{i,p}(\alpha)N_{j,q}(\beta)\boldsymbol{p}_{\boldsymbol{ij,x}}\\ \boldsymbol{v}(\alpha,\beta) &= \sum_{i=0}^{n}\sum_{j=0}^{m} N_{i,p}(\alpha)N_{j,q}(\beta)\boldsymbol{p}_{\boldsymbol{ij,y}}\end{aligned} \tag{36}$$

$N_{i,p}(\alpha)$ and $N_{j,q}(\beta)$ are multi-segment, continuous polynomial functions which serve as basis of the displacement at (α,β).

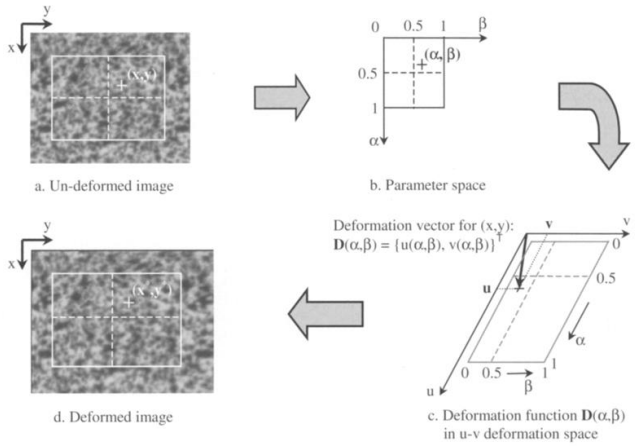

Figure 31: B- Spline parameter space correlation [54]

There are n control points in the α direction and m control points in the β direction over which i and j iterate respectively. For a given direction α, these splines are recursively generated based on equation (37).

$$N_{ip}(\alpha) = 1, \quad if\ \alpha_i \le \alpha < \alpha_{i+1}$$
$$N_{ip}(\alpha) = 0, \quad otherwise$$
$$N_{ip}(\alpha) = \frac{\alpha - \alpha_i}{\alpha_{i+p} - \alpha_i} N_{i,p-1}(\alpha) + \frac{\alpha_{i+p+1} - \alpha}{\alpha_{i+p+1} - \alpha_{i+1}} N_{i+1,p-1}(\alpha) \tag{37}$$

A material point (x,y) in the **M x N** pixels region of interest moves to (x*,y*) according to displacements in (36). Assuming that the grayscale value of this point stays constant, the correlation process to optimize the values of $\boldsymbol{p_{ij,x}}$ and $\boldsymbol{p_{ij,y}}$ is carried out for all the pixels in the **M x N** pixel area [54]. This approach has been successfully been applied for rigid body translation and rotation, quadratic deformations, and uniaxial tension testing in [54] and they found their B Spline parameterization method approach to be better than their subset approach. It is also worth noting that though this approach accounts for continuity in the material, when testing is being performed when new surfaces are formed due to cracking and plastic deformation, a different parameterization approach will be required.

A DISCUSSION

SUBSET SIZE AND STEP

Subsets serve the function of uniquely representing a material surface point. Subsets must be big enough to cut through some of the speckles on the surface and enclose some spots such that every subset in the image is as unique as possible.

Table 6: A study of effect of subset size on the strain noise

Subset Size	75			50			40			30			20		
Subset Step	19	38	56	13	25	38	10	20	30	8	15	23	5	10	15
Overlap %age	75	49	25	74	50	24	75	50	25	73	50	23	75	50	25
# of Points	12054	2969	1382	26804	7161	3104	45596	11374	4994	71701	20333	8604	184595	45686	20353
Strain Noise (%)	0.025	0.013	0.008	0.134	0.075	0.02	0.142	0.041	0.023	0.252	0.11	0.059	0.756	0.304	0.13

While bigger subsets do give more accurate results, it is at a cost of computing power [29]. The accuracy increase reaches a saturation point beyond which increase in subset size will not increase the accuracy anymore[29]. *Table 6* shows a study of the effect of size of subsets and density of the subset grid on the zero deformation noise. Two images were acquired at the same configuration of the specimen and the strain noise was computed.

Continuum vs. Subset Methods

Comparative studies between full field and subset based DIC methods are found in literature. In the study by Sutton et al. [54] the B-Spline method is claimed to be faster and more accurate than the subset method. However, this method is error prone near boundaries compared to the subset method. It also requires a complete overhaul of the displacement function assumed when the material tested has discontinuities, making its application less flexible. Shen and Paulino conclude in their work that finite element based and subsets methods have similar accuracy. However, errors are found to be more consistent in the finite element method compared to the subset method [34]. Noise has a higher standard deviation in the subset method [35]. Both methods suffer when computing the displacements at the discontinuities (i.e. crack tip, notch, hole etc.) in material being considered. The variation in strains obtained by subset based is also much higher compared to that of element based full field methods. Zhang et al. [33] also perform a comparative study of the subset based method and finite element based method. They test it on aluminum plates with holes and conclude that the two methods yield comparable results. However, both methods have their own benefits and drawbacks. For a given number of points to be tracked in image, the subset method is more efficient for the same number of points. In contrast, finite element methods fare better at measurements of specimen with complex geometry compared to the subset method. To combine the advantages and minimize the cons of these two methods, a novel adaptive DIC method is proposed in [33] which meshes the whole image by the principles of finite element meshing instead of the simplistic division of the image into subsets. To improve efficiency, at the nodes of this mesh subset based correlation procedure is used.

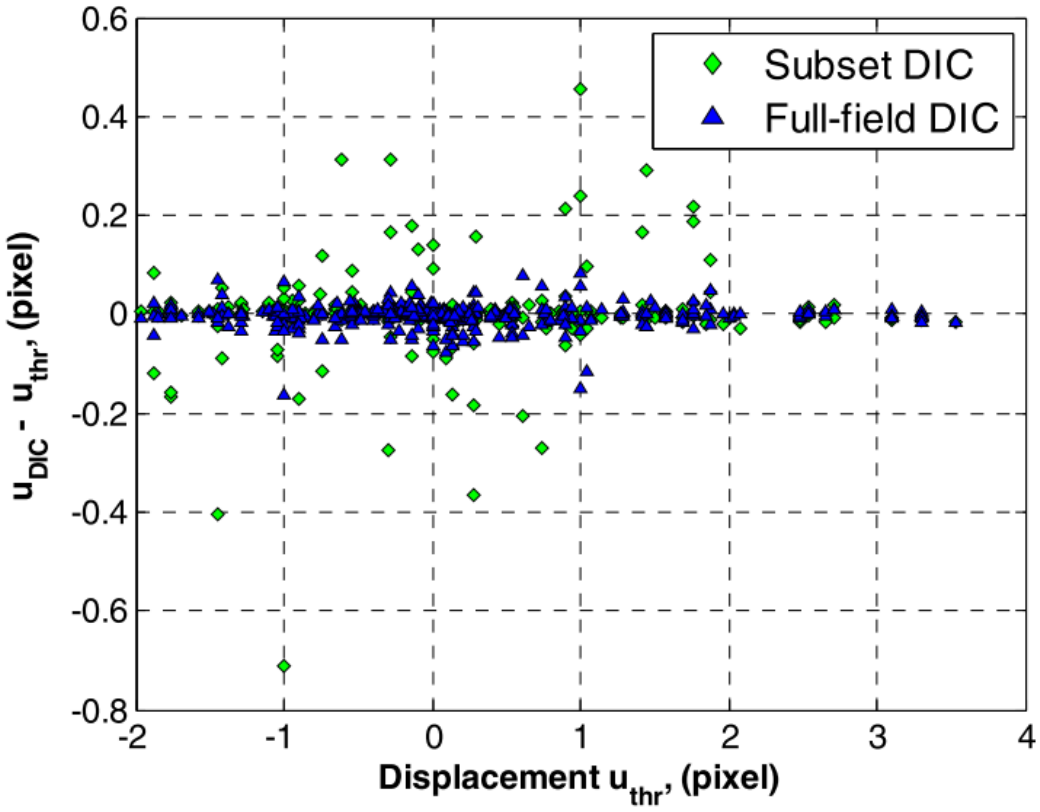

Figure 32: Error comparison of field and subset based method [34]

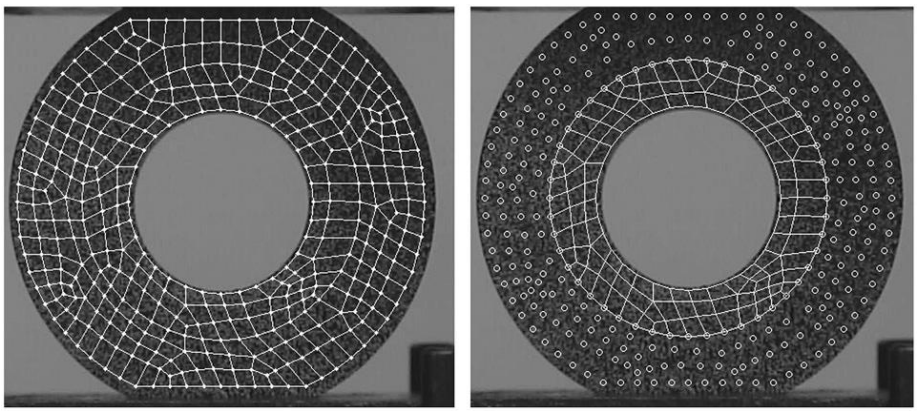

Figure 33: The adaptive FEM - DIC method;(Left: Mesh on the specimen; Right: Nodal measurement points)

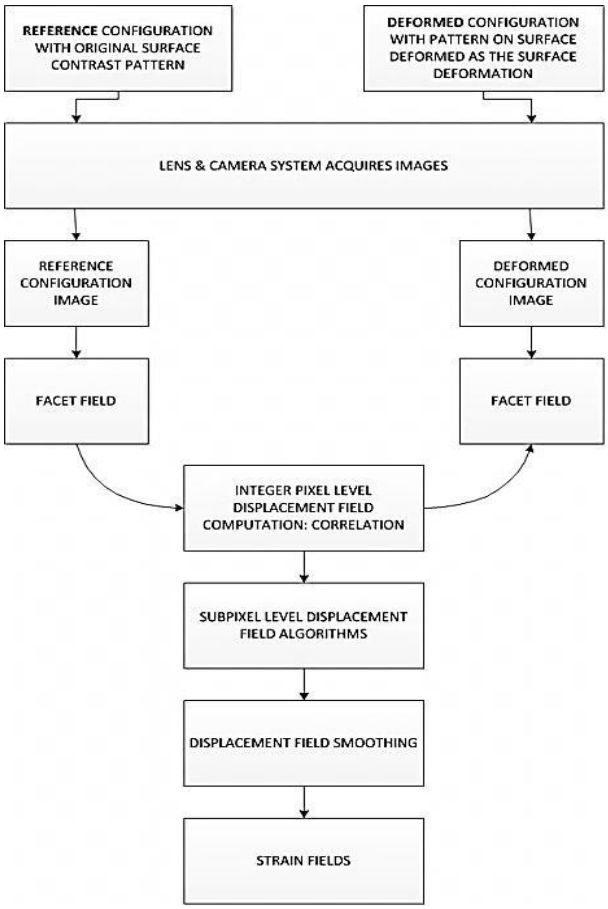

Figure 34: Basic framework of DIC displacement and strain computation algorithms

CHAPTER 3: STRAIN HETEROGENETIES IN POLYCRYSTALLINE METALS

3.1 APPROACHES

A salient feature of optical non-contact approaches is full field strain and displacement measurements with good accuracy and reliability obtained in the region of interest without any physical contact. These optical methods that rely on visible light wave find their roots in methods using electromagnetic waves (interferometry) to obtain information about the material. Reflection, interference and diffraction of electro-magnetic waves such as X-ray and visible light, as well as beams of sub atomic particles such as electrons and neutrons are utilized to observe grain behavior under loading. Displacements and strains are quantified by recording and processing numerically the changes observed in the fields of intensity and phase of the wave used. The various approaches found in literature to monitor strain heterogeneities at the grain scale are broadly categorized as follows:

1. **Interferometry Methods**

— Holographic Interferometry (HI)

— Moiré Interferometry

2. **Diffraction Methods**

— X-ray Diffraction (XRD)

— Neutron Diffraction

— Electron Backscattered Diffraction (EBSD)

3. **Other Methods**

— Grid Method

— Digital Image Correlation (DIC)

INTERFEROMETRY METHODS

Interferometry techniques are based on the interference phenomenon of visible light. Visible light is an electromagnetic wave with an amplitude and phase associated with it. When a beam of light of a given phase interacts with another of a different phase, it undergoes constructive or destructive interference.

SPECKLE AND HOLOGRAPHIC INTERFEROMETRY:

A detailed review of holographic [56] and speckle techniques [56, 57] are presented in literature. Here, the basic working of the method is presented. When coherent light is reflected from the surface of an optically rough opaque material, the reflected wavefronts have a random distribution of intensity in space. This is called speckle pattern and is unique to the combination of rough surface, incidence and observation angle.

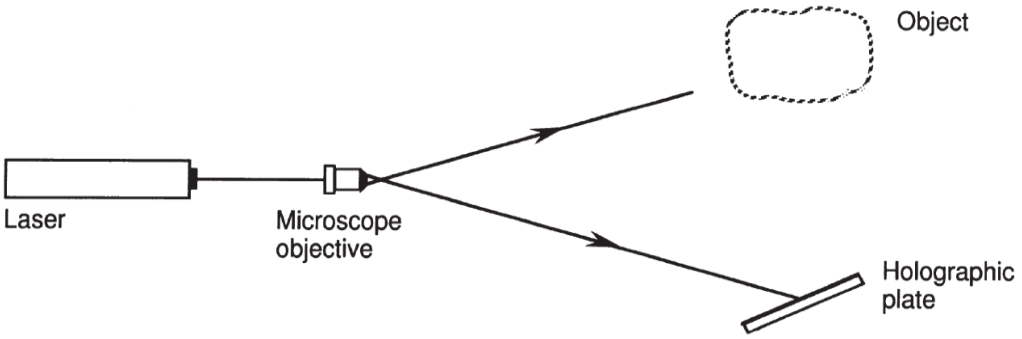

Figure 35: Holographic recording [56]

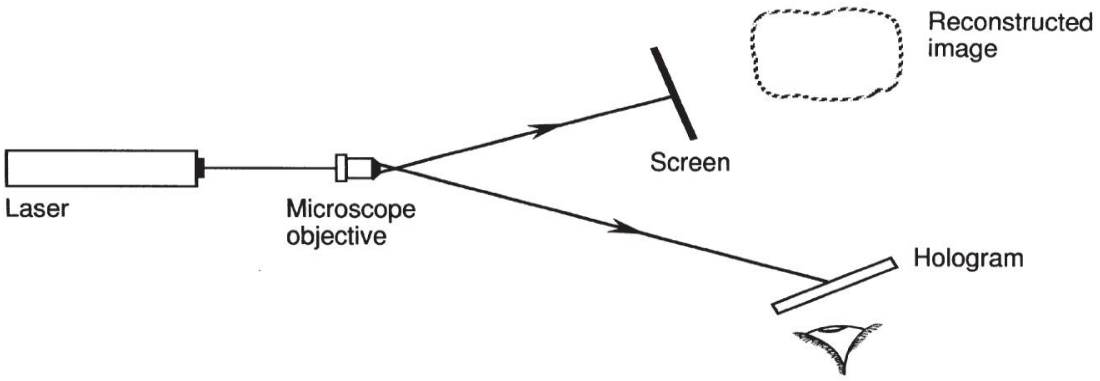

Figure 36: Holographic reconstruction [56]

These speckle patterns reflected off surfaces can be used to track the surface changes though time. The amount of interference in the light observed between speckles recorded initially and in those recorded subsequently at deformed configurations give information about the deformation that takes place on the material surface [56, 57].

Holographic interferometry is a specialized from of speckle interferometry where three-dimensional reconstruction of the object surface is possible [57]. Holograms are recordings of light amplitude and phase on specialized holographic plates, traditionally photographic films or in the modern day, CCD sensors. Light scattered from an opaque object's surface is made to interfere with a reference wave, which results in a fringe pattern. This fringe pattern is recorded by exposing it to a holographic plate and then developed to get a hologram. The original wave scattered from the opaque surface can be reconstructed by shining a beam of light similar to the reference wave on the hologram. This way, an object's three-dimensional geometry at a given point in time can be stored and recalled.

Reconstruction of the recorded wave can be done pointwise using a laser scanner where the reference wave is passed along the recording one point at a time, reproducing the interference pattern at the region illuminated by the beam. It can also be achieved by using a full field collimated laser beam where the reference wave is incident on the entire recording to reconstruct the complete image as opposed to the point reconstruction method.

Holographic interferometry is based on the principle that when light from the object's surface in its undeformed stage is recorded and imposed onto that when it is deformed, an interference pattern is obtained. This interference pattern can be used to estimate accurately how much the object deformed. Consequently, a hologram is recorded for the initial configuration of the sample. Then, the interference fringe pattern that shows the difference between the initial and final configuration of the observed object can be observed in three ways [56]:

I. Real-time by projecting the deformed object wave on the reconstruction of the initial configuration. Dark areas show destructive interference between the undeformed and deformed object waves i.e. the phase difference between the two is $2n\pi$ ($n = 0, 1, 2\ldots$) The real time projection can be recorded continuously by digital cameras to track the fringe pattern throughout the test.
II. In the second method, the same holographic plate is exposed to both the initial configuration and the deformed configuration light waves. When this double exposed hologram is reconstructed, the interference fringes which contain the information about the deformation of the object between the two exposures are obtained. This is permanently stored in the holographic plate. Bright fringes are seen when the phase difference between the two is $2n\pi$ ($n = 0, 1, 2\ldots$)
III. In the third method, two holographic plates are used simultaneously for a single exposure. After the object is deformed, a new pair of the plates is similarly exposed. After the holograms at both stages are developed, the back plate from the first exposure is sandwiched with the front plate and illuminated by the original reference beam of light. The

reconstruction now gives a fringe pattern of interference that gives information about the deformation between the exposures.

Experiments have proved the feasibility of digital CCD cameras instead of holographic plates to record the holograms and obtain the fringe patterns between the exposures. This has led to digital holography interferometry.

APPLICATION: The method of holographic interference was used by Gerasimov and Zhilkin [58] in measuring strains on the surface of grains and grain boundaries in commercial aluminum, which is a polycrystalline metal. The holograms were obtained at 11 steps through the tensile loading of the aluminum sample up to 0.6 kN. The superimposed hologram from the sixth step was interpreted quantitatively and was compared with finite element analysis which indicated good agreement.

MOIRÉ INTERFEROMETRY

The characteristic feature of this approach involves introducing line systems with alternating light and dark lines called gratings on the surface of interest. A given grating has a density α, which is the ratio of the width of the light stripe to the pitch, *p* which is the distance between the center lines of the light and dark stripes. Grating with low density can be used with normal visible light (incoherent) and the resulting moiré patterns can be seen with the naked eye. However, as the grating density increases, coherent light must be used for moiré patterns instead of normal visible light as diffraction effects become more prominent and adversely affects the moiré patterns produced.

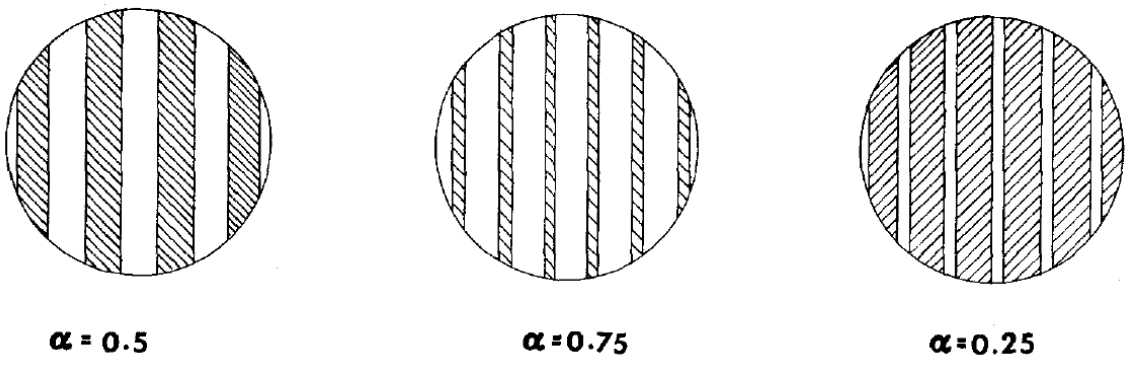

Figure 37: Line gratings with ratio of the width of the transparent space to the distance between the center lines [59]

Gratings can be applied to the surface by either engraving the moiré patterns or projecting them on to the surface. Two functional kinds of gratings are necessary. One grating called the model grating is used to track the relative changes on the surface from the initial undeformed configuration to the final deformed configuration. Another grating called the master grating is used to determine the changes in the model grating. When these two gratings are superimposed and observed using a camera, they produce moiré patterns in the image plane of the camera [59].

The intensity of the transmitted light for superimposition of the model and master grating, when the lines of grating are normal to the grating's assumed *x* axis is given by:

$$I(x) = I_0 + I_1 \cos 2\pi\psi(x) + I_2 \cos 4\pi\psi(x) + I_3 \cos 6\pi\psi(x) + \cdots \quad (38)$$

WHERE:

I_0	Background Intensity	$I_1 I_2 I_3$	Harmonic Components
$\psi(x) = (\frac{1}{p} - \frac{1}{p(x)})x$		$p(x)$	Local equivalent pitch

These patterns give information about the displacement that took place in the model grating with respect to the master grating in the direction normal to the master grating. The actual mathematical relationship between the moiré patterns and the displacements depends on which method of moiré interferometry is used. The displacement fields obtain in such a way can be used to estimate strains of the surface monitored. Depending on the relationship between the model grating, the master grating and the observation system used displacements are extracted from the change in moiré patterns in three ways. They are (1) intrinsic moiré: where displacements of points are measured with respect to their initial positions (2) shadow moiré: where the displacements are measured with respect to another reference surface (3) reflection moiré: surface slope with respect to the reference state is obtained to give displacement gradients.

APPLICATION: With the use of gratings appropriate for the grains observed in a material, this method has been extended to observing strains on individual grains at the tip of the crack in polycrystalline materials.

One such instance is the work of Bastowros and Kim [60]. Aluminum alloy 6061-T6511 with an average grain size of 80 µm was loaded in displacement control in a four-point bend test. A gold layer of 50 Å was applied to improve surface reflectivity. A field of view of 1 mm around the crack tip was observed with strain sensitivity between 0.1 % and 10 %. Two moiré patterns, one at the front of the crack and other at the back of the crack tip, were recorded at every stage of loading to get the in plane displacement components. The moiré patterns themselves were recorded in 512 x 480 pixel images. For two

stages, strains at individual grains and the fluctuations from grain to another were obtained. However, in another stage when the moiré pattern recorded had lesser fringes per unit area, the strain fluctuation was not resolved into individual grains.

Use of state-of-the-art moiré interferometry equipment has been demonstrated in [61] and the methodology is more sophisticated compared to [60]. In this work, Aluminum alloy was loaded in tension and its surface was etched with a corrodent to exposed grain structure. The evolution of the grain structure and the moiré interferometry patterns that evolved with each grain are shown in Figure 38. Strains in X and Y direction were obtained for five individual grains. It was concluded that strains vary from grain to grain but stay fairly homogeneous within each grain through loading.

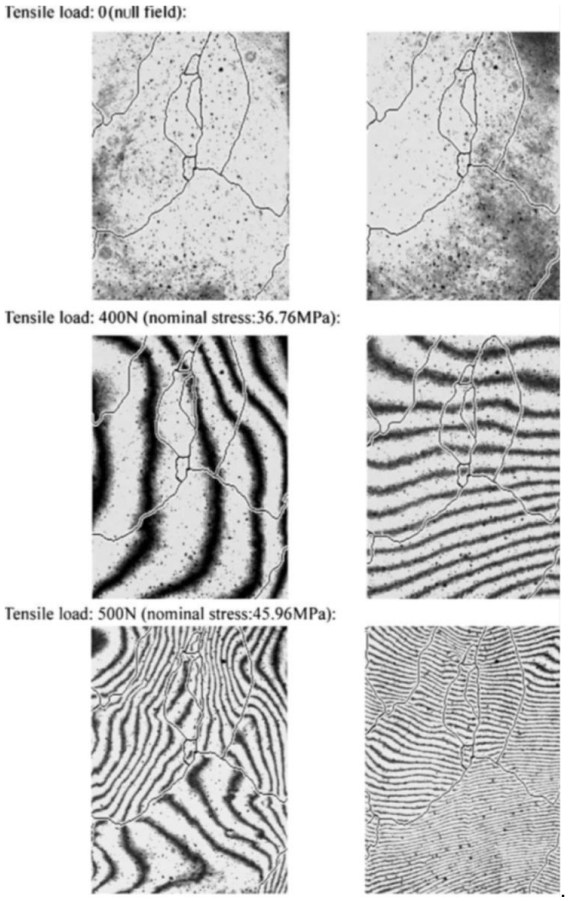

Figure 38: Moiré Interferometry applied to polycrystalline aluminum [61]

DISCUSSION ON INTERFEROMETRIC METHODS

The key strength of holographic interferometry is its spatial resolution that can reach 5000 lines/mm. However, the implementation of holographic interferometry is very time consuming when photographic plates are used as they have to be developed using wet chemical procedures. Also, the recorded waves must be reconstructed using a coherent source of light. In moiré interferometry, the specimen preparation is cumbersome and time consuming as two sets of gratings need to be imparted to the specimen surface. In addition to this, rigid body motion and rotation induces additive fringes which lead to fictional displacements in the post process of the fringe patterns. So care must be taken to adjust the loading frame to rule out these effects.

DIFFRACTION METHODS

Diffraction is the phenomenon seen in waves where they bend around an obstruction in the length scale of their wavelength. This phenomenon is manifested in single slit and double slit experiments where light passes through the slits and then spreads out. The diffraction phenomenon observed in waves of x-rays, neutron rays and electron rays has been used to observe the grain and lattice behavior in materials, because the wavelengths of these rays are comparable to the grains length scale in most crystalline metals.

The basic hardware setup for a diffraction measurement is the same for electron, x-ray and neutron diffraction. Figure 43 shows a schematic of the various components used in neutron diffraction measurements. A beam from an appropriate source (x-ray, neutron or electron) is incident on a specimen mounted on a stage. The incident beam scatters when it hits the material lattice structure and the scattered rays are collected on detectors located at the path of these scattered rays. Information about lattice orientation is inferred using the intensity and the phase of the received scattered beam. A mechanical loading device can be mounted on the stage to induce loading on the specimen. Using such a configuration of the diffraction system and the loading stage, waves scattered from the material lattice can be monitored *in-situ*. Lattice strains can be calculated by observing changes in lattice geometry.

X-RAY DIFFRACTION

An X-ray radiograph of a material of interest is obtained by projecting a cone-beam of X-ray a material mounted on a stage. The material absorbs some of the X-ray depending on the energy on the x ray beam, the atomic number of the element, and

the density of the material. The rest of the X ray transmitted from the material is received on a florescent screen which converts it to visible light which is then captured on a cooled CCD camera.

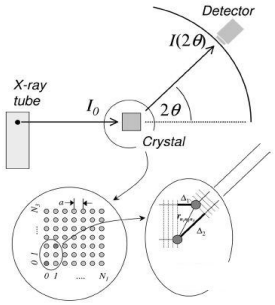

Figure 39: The mechanism of the X ray diffraction observed in a simple cubic lattice [62]

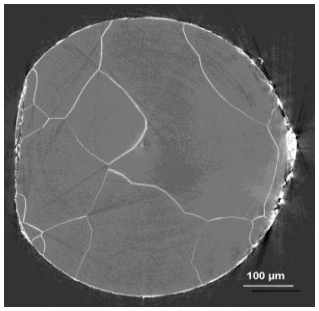

Figure 40: 2D Grain structure of pure Al wetted with Ga – XRD [63]

In some materials, different constituents may have the same attenuation factor for the intensity of transmitted x-ray. In such cases, the phase of the transmitted beam is also quantitatively analyzed to obtain lattice information. In X ray tomography, multiple X ray radiographs are acquired at different orientations of the material and the three-dimensional structure of the material is computed as shown in Figure 41. High intensity X-rays which are parallel with the divergence of the beam about 1 µradians can be used to obtain high resolution maps which aid in micro-tomography.

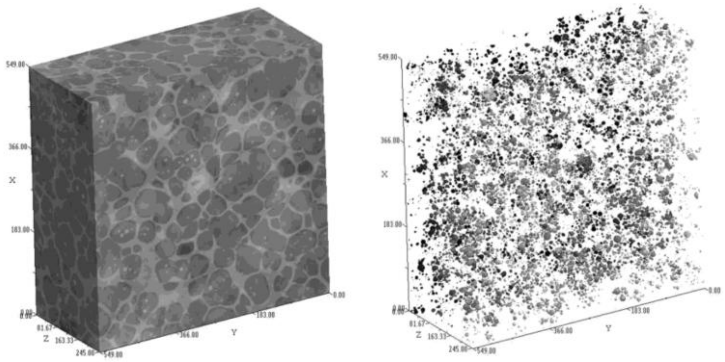

Figure 41: X ray tomography 3D construction - A357 alloy (right) & Entrapped liquid (left) [63]

A mechanical testing device can be mounted on the stage in line with the x ray beam and in-situ tensile tests with resolutions as small as 2 µm be made [63].

APPLICATION: Polycrystalline aluminum wetted with liquid gallium has exposed grain boundaries due to the effect of gallium on grain boundaries. This phenomenon can be observed using X ray tomography [63]. Far field type 3D X ray diffraction was used by Oddershede et al. [64] in their work of quantifying stress on individual grains, overall stress fields and lattice rotations. They performed tensile loading on a notched dog-bone sample of MgAz31 alloy with an average grain size of 30 µm and monitor an area of 165 x 165 µm2 for tomography. X ray maps were obtained at certain levels of which an example is shown in Figure 42 (B). Software was used to identify grains and calculate their center of mass, orientations and the elastic strains from the diffraction maps recorded in the experiment.

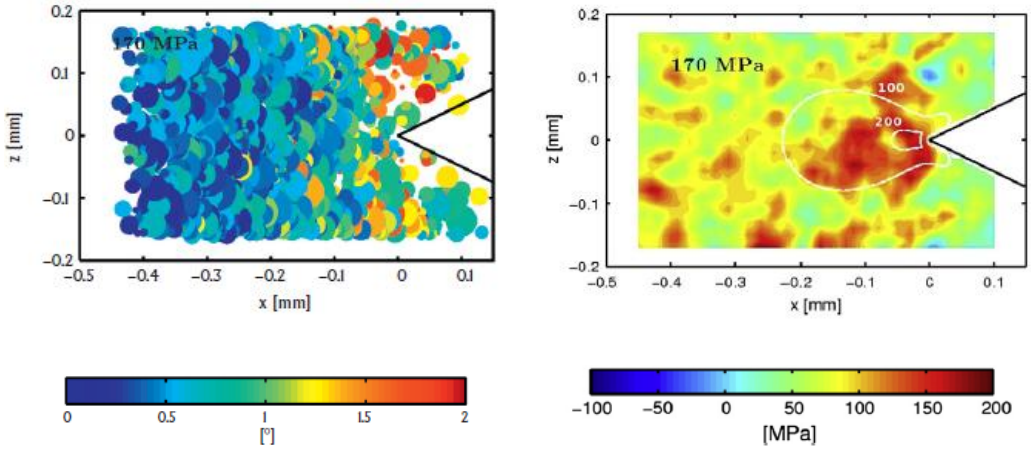

(A) MEASURED LATTICE ORIENTATION

(B) σ_{11} STRESS MAP WITH OVERLAID CONTOURS FROM ABAQUS 3D FEM SIMULATION

Figure 42: Lattice orientation (A) and Stresses (B) measured at tip of notch on MgAz31 alloy (Applied load - 170 MPa)

NEUTRON DIFFRACTION

In the last two decades, neutron diffraction has been developed as an alternative complementary technique to the conventional X-ray method. Neutron diffraction is an experimental technique with huge potential for the characterization of residual stress via probing the interior of solids. It brings the opportunity to acquire otherwise inaccessible information on the state of strain within the bulk of structure. It provides a spatial resolution that is readily adjustable and is adequate for resolving strain gradients in engineering components.

Unlike X-rays which are electromagnetic waves, neutron waves are particle waves and have greater penetration depth and can be used to probe into specimens > 20mm thick. X-rays can be used to get strains in two directions in the plane of the surface being measured. However, it does not fare well in measuring strains in the direction perpendicular to the surface of incidence due to low penetration. Its use can be complemented to the use of neutron diffraction. Such a combination has been used in [65] to quantify the residual stresses along all three directions in welded plates of Al 2024 alloy.

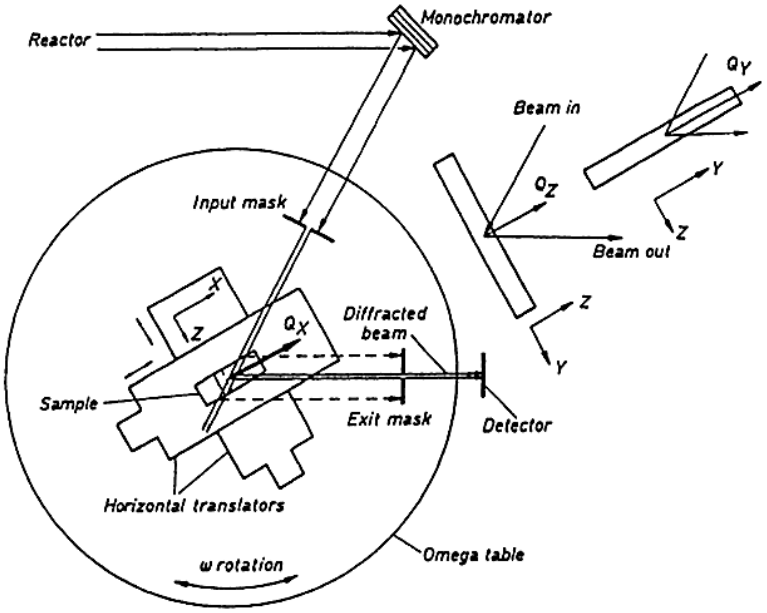

Figure 43: Neutron diffraction equipment schematic [66]

In this experimental setup, a neutron beam is directed on to the sample. The scattered rays are received by four plates at different angles with respect the incident beam and recorded. When a mechanical testing device is incorporated into the setup, the variations in the detected scattered beams' angle and phase is used to determine the changes in the lattice of the material being loaded in the mechanical testing device. Agnew at al. [67] described the use of a time-of-flight technique in neutron diffraction that allows the measurement of lattice strains along any required lattice plane by changing the position of the scattered ray detector. The difference between the spacing of the lattice planes measured at stress-free and loaded configurations of the material is used to obtain internal microscopic strains.

APPLICATION: Ganguly et al.[65] used X ray and neutron diffraction together to quantify the stresses around a weld joint in Al 2024 alloy which is widely used in aircraft fuselage. The average grain area in this work was 48 x 15 μm^2. Internal strain

distribution in the lattice of the MgAz31 alloy was successfully quantified. The behavior of individual grains with respect to the overall strains was computed from recording the in-situ scattered beams of neutrons. In the work done by Agnew at al. [67] MgAz31 with an average grain size of 50 µm was loaded in tension and compression in a horizontal load frame. A neutron powder diffractometer was used. The detectors were positioned such that diffraction data obtained could be used to compute both in plane and cross sectional internal strains.

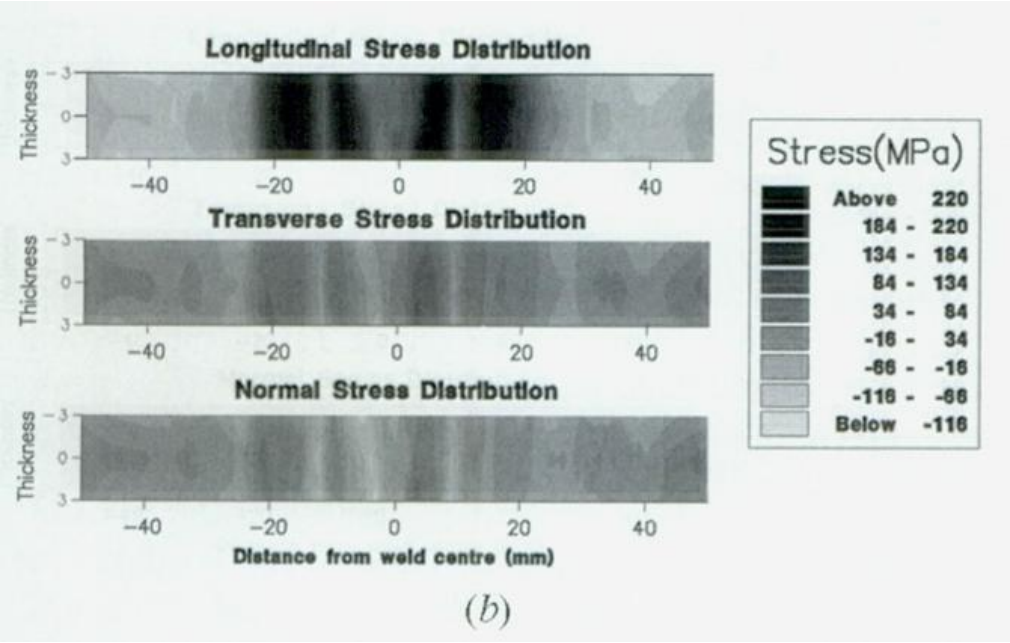

Figure 44: Stress contours on Al 2024 alloy using neutron diffraction and XRD [65]

ELECTRON BACKSCATTERED DIFFRACTION

Electron Backscattered Diffraction (EBSD) is an offshoot of the Scanning Electron Microscopy (SEM) where the diffraction properties of electron beams are utilized to obtain maps of the crystal orientations on the surface (~50nm [68]) of crystalline material. Electron beam from an SEM is incident on the specimen which is tilted with respect to the incident beam. The tilt controls the resolution of the map obtained. The electrons disperse due to interaction with the crystal lattice just below the surface and diffract along the material's crystallographic planes.

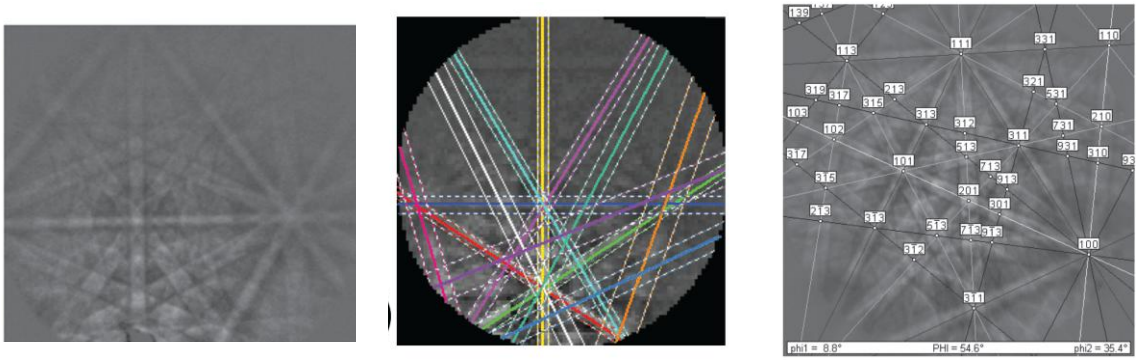

KIKUCHI PATTERNS | BANDS FROM HOUGH SPACE | ORIENTATIONS OF LATTICE PLANES

Figure 45: EBSD orientation determination procedure [68]

Kikuchi patterns are produced when these electrons interfere constructively. The interference patterns are received by a phosphor screen which is placed close to the specimen (~35mm [69]). The light emitted by this screen is captured as a digital image by CCD cameras. Orientations of the lattice elements are then determined by a three step process [68]:

- Kikuchi band detection: The pattern is transformed into Hough space by converting Kikuchi lines to points.
- Kikuchi band identification and indexing: Spacing, angles and zone axis of lattice planes are determined in this step by comparing with theoretical values
- Orientation determination: Using the information obtained from step (2), the actual orientation of all the lattice planes are computed with respect to a picked reference lattice plane. The miller's index of every grain observed can be computed this way.

APPLICATION: Orientation maps shown in Figure 46 were those obtained by Kamaya et al. using an Oxford Instruments INCA system interfaced to a JEOL JSM-6300 SEM with LaB_6 electron gun. They also report use of a TSL EBSD system interfaced to a JEOL JSM-6500F with a field emission electron gun. They obtain a reference scan at 0% and perform scans ex-situ after deforming the sample in steps of 1.3 %, 2.8%, 4.4%, 7.2% and 14.4% strain. At every step, the region of interest on the surface of the specimen was prepared by using 3 µm diamond paste and electro polishing using a combination of acetic acid and perchloric acid. The stainless steel they observed was oriented at 70° with respect to the horizontal axis. The scanning was done with a step size of 2.25 µm for crystal orientation measurements and then shifted by $2.25/\cos 70^{\circ} = 6.58$ µm. This corresponds to a resolution of 15.8 μm^2/pixel and gives 25344 measurements points in Figure 46 (a) and 23808 measurement points in Figure 46 (b). The color map itself is a map of the continuously varying crystal orientations. A

discontinuous change in the map represents grain boundaries. As we see in Figure 46, the distribution of crystal orientation with each grain is fairly consistent at 0% strain (b) and there is increased variation within a single grain when the plastic strain at 14.4% plastic strain (a). This indicates that plastic strains induce heavy misorientations within a grain in crystal and the range of these misorientations increase with increase in plasticity. To quantify this, an entity called the crystal deformation C_d is used.

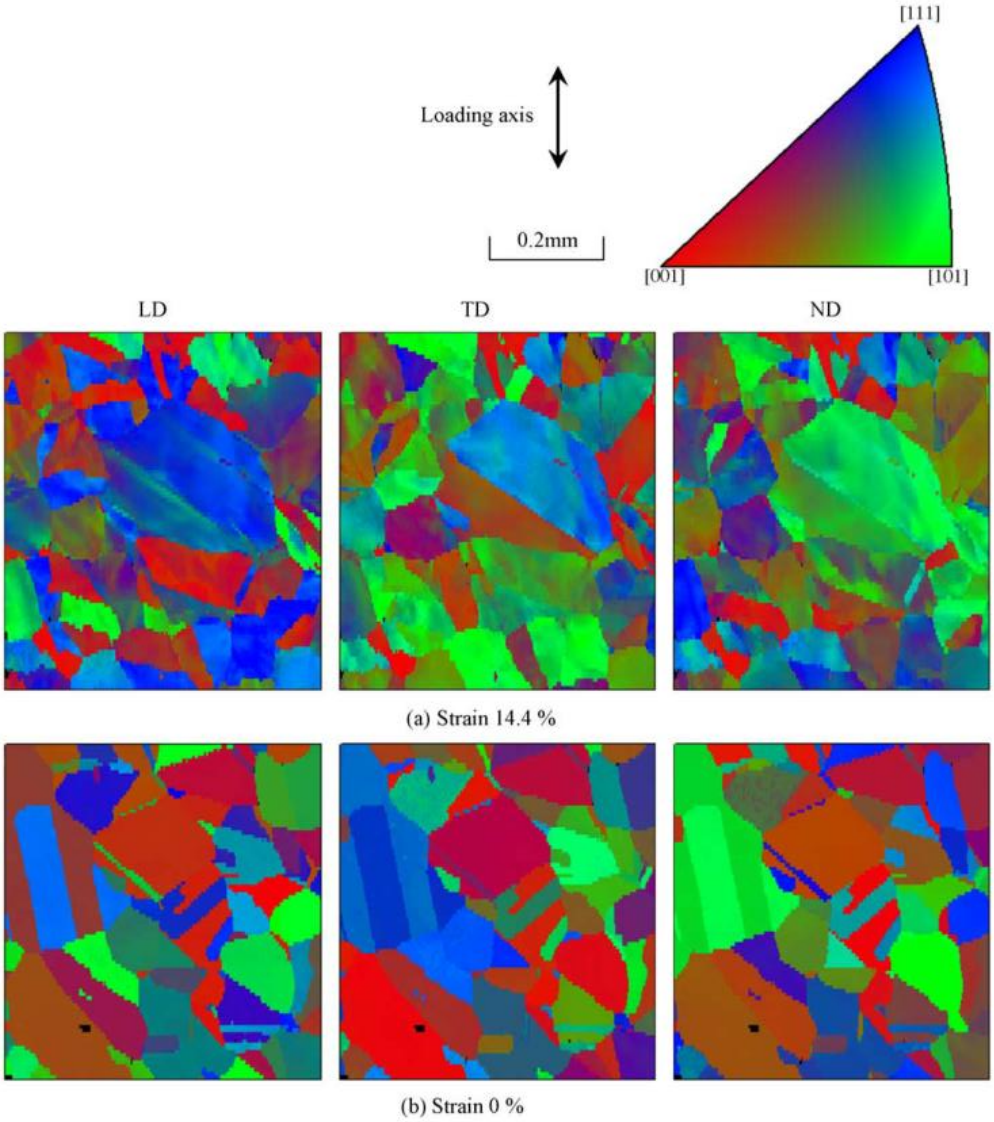

Figure 46: Grain orientation maps of stainless steel from an EBSD [70]

$$C_d = \frac{\sum_{k=1}^{n_g}(\sum_{i=1}^{n_k}\beta(p_k,i))}{\sum_{k=1}^{n_g} n_k} \tag{39}$$

WHERE:

$\beta(p_k,i)$: Misorientation between a reference point *p* with and all other point *I* within the grain

n_g : Number of grains n_k : Number of points in the grain

p_k: the point with the reference orientation for the k^{th} grain

Also, by extending cross correlation algorithms to crystal orientation maps obtained from EBSD [69] the degree of plastic strain can be computed using the changes in the local orientations. The variation in the crystal orientation inside a grain is brought about by crystallographic changes such as dislocations motions and twinning mechanisms caused by tensile plastic deformation. Changes in lattice planes cause changes in the zone axes computed in the EBSD patterns. These shifts are related to the displacement gradient tensor by (40)

$$q = Q - (Q \cdot \hat{r})\hat{r} \tag{40}$$

WHERE:

$$Q = a\hat{r} = \begin{pmatrix} \frac{\partial u_1}{\partial x_1} & \frac{\partial u_1}{\partial x_2} & \frac{\partial u_1}{\partial x_3} \\ \frac{\partial u_2}{\partial x_1} & \frac{\partial u_2}{\partial x_2} & \frac{\partial u_2}{\partial x_3} \\ \frac{\partial u_3}{\partial x_1} & \frac{\partial u_3}{\partial x_2} & \frac{\partial u_3}{\partial x_3} \end{pmatrix} \begin{pmatrix} r_1 \\ r_2 \\ r_3 \end{pmatrix}$$

$u = (u_1, u_2, u_3)$ Displacement Vector @ $x = (x_1, x_2, x_3)$

$q = (q_1, q_2, q_3)$ Shift in EBSD pattern in direction perpendicular to $\hat{r} = (r_1, r_2, r_3)$

The strains are obtained from the gradients calculated. The shift **q** is obtained by correlation between EBSD patterns.

DISCUSSION ON DIFFRACTION METHODS

Neutron diffraction has much greater penetrability that X ray diffractions, neutron interaction with matter is weak and this implies that to scan at a depth of 20 mm, will take about ten minutes to scan [65]. Also, some matter may absorb the neutron incidents, in which case there is no scattering, rendering the approach ineffective. X-ray scans are much quicker than neutron diffraction methods. X-ray synchrotron as used in [64] enables a unique combination of imaging and diffraction using the same technique. Grain resolved measurements such as the one done in this study helps understand local phenomena that cannot be explained by continuum mechanics. However, this approach will not be capable to directly correlate global and

local strains in the same picture. In-situ X ray diffraction tomography requires several wide angle X ray diffraction scans in the same configuration of the specimen, and this means that the load on the specimen must be held which may cause side effects such as stress relaxation and creep.

PHOTOGRAMMETRY METHODS

GRID METHODS

The grid method employs a regular pattern applied on to the specimen surface. Images of the surface are acquired at a reference and deformed configuration of material. Signal processing is applied to extract the phase change of the regular pattern as the material goes from initial to the deformed stage. Displacement is proportional to phase change and strains can also be extracted directly from the phase derivatives.

Recently, the grid method was applied to measure Green-Lagrange strain on the surface of polycrystalline aluminum sheets for seven grains each about a centimeter large [71]. A grid printed with 12000 dpi resolution was placed on the surface of the material with a layer of adhesive. The resolution of the camera was 5 pixel/grid of the pattern applied to polycrystalline surface. In this work, the strain evolution on the grain surface was compared with finite element simulations at various points in the test and it was in good agreement.

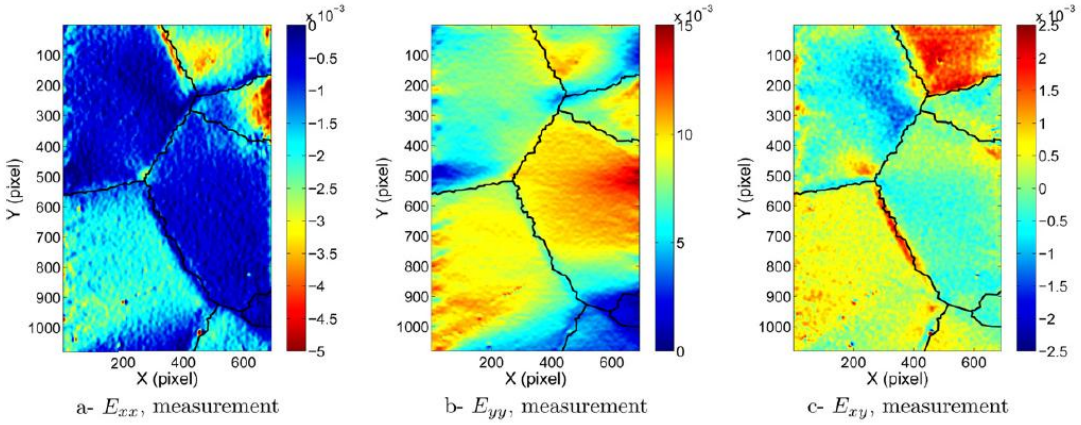

Figure 47: Strain maps on grains obtained by grid method [71]

The key difference in grid methods and Digital Image Correlation is the pattern applied and the method of post processing. To implement grid methods, a necessarily regular pattern with periodic variations are deposited on the region of interest. These patterns carry the deformation information. The phase change in the regularity of the applied pattern is tracked and these phase changes are utilized to compute the surface deformation.

3.2 DIC IN POLYCRYSTALLINE MATERIAL GRAIN STRAIN

DIC is a robust engineering tool that can be used to make accurate *in-situ* and *ex-situ* measurements in the laboratory as well as in the field. While it is true that in-situ methods like X-ray diffraction, neutron diffraction and EBSD can be used to quantify grain strains with very high resolution, DIC is a practical method that has been applied to obtain strains on grains varying from ~50 μm to few mm in length in bending , compression and tension tests with good accuracy [6, 72, 73] and can be used with images acquired from various sources. Though the accuracies of interferometry methods and DIC are comparable, the sample preparation involved is much simpler in DIC. Also, with progress in optical imaging technologies over the years, microscale imaging has grown by leaps and bounds. Digital microscopes can be integrated with CCD cameras and be used for *in-situ* measurements. Schreier at al. [21] give an example of microscopic stereo vision employed in DIC to quantify strains in a field of view of 7.6 x 4.8 mm^2 with 10 μm/ pixel resolution.

Table 7 lists grain strain quantification work doneby Jin et al. [74], Abuzaid et al. [75], Zhu et al.[72], Rehrl et al.[76], Carroll et al. [6], Padilla et al.[77], Tschopp et al.[1], Ahn et al.[78], Jonnalagadda et al. [25], Bartali et al. [79, 80], Renard et al.[81], Lei at al.[82], Hokka et al. [83], Neindorf et al.[73], and Efstathiou et al.[84]. These researchers have used DIC to monitor evolution of strains on grains of sizes ranging from ~750 nm to a few millimeters. Tensile, compressive, bending and fatigues tests were performed on polycrystalline materials like aluminum and its alloys, magnesium alloys, nickel alloys, titanium, steel, platinum and zirconium. Electrochemical etching, speckle patterning and micro-particle deposition have been found to be reliable methods to provide necessary surface contrast on the grain surface.

For in-situ image acquisition, digital optical microscopes are a popular choice used in many instances mentioned in Table 7. In-situ images acquired from Scanning Electron Microscopes were also used successfully to perform DIC. CCD cameras coupled with optical microscopes have also been used for in-situ image acquisition. For relatively low strain rates, cameras with 0.5 – 19 frames per second image acquisition rate and for high strain rates, high speed cameras with image acquisition in the order of several thousand frames per second are used.

Work	Year	Test			Measurement	DIC			
		Type	Material	Average Grain Size		Patterning	Software	FOV & Image	Resolution
Jin et al.	2011	3 point bend	Aluminum	–	In-situ SEM DIC with Backscattered Electronic Imaging (BEI); EBSD orientation maps;	Au particles through Cu mesh; Grid Patterning	ARAMIS	1150 x 980 µm² 1350 x 1150 px	0.85 µm/px
Abuzaid et al.	2012	Tension; Strain Controlled;	Hastelloy X	50µm	SEM w/ EBSD detector (8*300X), Ex situ DIC w/ 316 overlapping optical microscope images;	1 µm Si particle Pressure Deposition	-	1 X 6 mm²	0.14 µm/px
Zhu et al.	2011	Tension; Disp. Controlled;	Al Alloy 5754	1.25 mm 0.6 mm	In-Situ (0.5 fps) w/ EBSD at beginning and at strain intervals	Speckle Pattern	ARAMIS max strain dev. 0.005	5.5 x 5.5mm² †	17.85 µm/px
Rehrl et al.	2011	Compression; Constant Speed;	Stainless Steel; A220/316L;	~ mm range column grains	Ex-Situ SEM image DIC 6 steps of plastic strain 0 – 60% in split sample	Grinding paper imprint to create stochastic pattern	Alicona	350 x 350µm²	-
Carroll et al.	2010	Strain Rate Controlled;	Hastelloy X	100 µm	EBSD maps from SEM Ex situ DIC with 316 images satitched DIC field stitching	1 µm Si particle Pressure Deposition	Vic2D	500x960µm²	0.14 µm/px
Padilla et al.	2011	Compressive; Strain Rate Controlled;	Zirconium	50 µm	In-Situ DIC (5000 fps)	1 µm Si particle Pressure Deposition	In-house	500 x 400µm² 512x512 px	1.2 µm/px
Tschopp et al.	2009	Tensile loading; 12 Steps	Rene 88DT (Ni based super alloy)	-	In-Situ SEM; Secondary electron 16 bit images DIC; EBSD orientation maps	Through thin film laser ablation of Pt 1 µm particles	Vic2D	274x230 µm² 4096x3773px	-
Ahn et al.	2009	Micro-tensile; Strain Rate Controlled	Al 5083	~240 nm (fine grain) ~ 4 µm (coarse grain)	In-Situ light microscope; 2 fps DIC	Micro-surface contrast	Vic2D	1,392×1,040 pixels, *Low mag:* 1,727×1,290 *Hi mag:* 434×324 µm	Low mag: 1.24 µm/px Hi mag: 0.31 µm/px
Jonnalagadda et al.	2009	Micro-tensile; Strain-Rate Controlled	Platinum thin film on Silicon substrate	~ 25 nm	X Ray diffraction grain size and texture; In-situ Optical Microscope DIC (15 fps at low strain rate; 10000 fps for high strain rate)	1 µm Si particle Pressure Deposition	-	700 µm	x200 mag.
Bartali et al.	2009	Low Cycle Fatigue	Duplex Stainless Steel	10 µm & 30 µm (Multiphase material)	In-situ microscopy with 10 bit CCD camera	Electrochemical etching	CorreliQ4 (FE Mesh type)	120 x 90 µm²	-
Renard et al.	2010	Tensile Tests; Disp. Controlled	TWIP Steel Alloy	21 µm	Optical DIC (3 fps)	Spray paint speckle pattern	-	-	-
Lei et al.	2010	Tensile; Fatigue	Nickel based alloy	> 20 µm	Digital Microscope	Electrochemical etching	-	88 x 60 µm ; 59 x 54 µm ;	-
Hokka et al.	2010	Compression: MgAz31 Torsion: AA 1070	MgAz31 AA1070	MgAz31: 6-8 µm AA1070: 750 nm	2 MP Cameras (19 fps) Phantom High speed cameras (1000-120000 fps)	Speckle patterning	-	-	-
Bartali et al.	2010	Low Cycle Fatigue	Duplex Stainless Steel	10 µm & 30 µm	EBSD grain orientation; Optical microscope with CCD cameras	Electrochemical etching	CorreliQ4 (FE Mesh type)	120 x 90 µm²	-
Niendorf et al.	2009	Low Cycle Fatigue	UFG Steel	100 nm – 1 µm	EBSD grain orientation; (1 µm step size); AFM analysis; Digital microscope DIC	Air brush; Si particles diluted in isopropanol	VIC-2D	-	-
Efstathiou et al.	2010	Tension; Disp. controlled	Titanium	30 µm	Microscope with Digital Camera	Speckle pattern	VIC-2D	140 x 140 µm² @ 50x mag (1600 x 1200 px)	0.087 µm/px @ 50x mag

Table 7: Details of various work found in literature that employ DIC to find polycrystalline metal grain strains

SURFACE CONTRAST

A crucial step in making DIC measurements on polycrystalline grains is deciding what method should be used to provide the contrast required on the surface. A challenge often faced is to maintain the visibility of the grain boundaries while also providing the necessary surface contrast.

The length scale of the region of interest and the size of the grains play a crucial role in the method to be picked for imparting the surface contrast. When speckle patterning with flat black spray paint or a combination of flat black and flat white paint is used, grain boundaries are still visible if an optical microscope with high magnification is used [84]. While this is a good example of successful use of spray paint, grain boundaries might not be visible in every scenario. For instance, in this very work, the grain boundaries are not visible at 3.2x magnification of the microscope. A direct extension of the principle of speckle patterning to microscale measurements is the use of air brush to deposit micro and nano particles on to the surface.

Depending on the region of interest, the particle size can be chosen. A suitable suspension or a solvent containing dissolved particles is used with standard air brush equipment. Toner powder dissolved in standard alcoholic natural solvent, gold particles deposited through a copper mesh or platinum particles dissolved in ethanol are examples from literature. Silicon

particle pressure deposition technique developed by Jonnalagadda et al.[25] is a reliable and consistent way of performing the patterning at this level as it helps control the evenness and density of the pattern. In certain cases, where etching has been performed on the specimen to expose the grain structure and boundaries, the end result of this process provides sufficient surface contrast for a reliable DIC measurement.

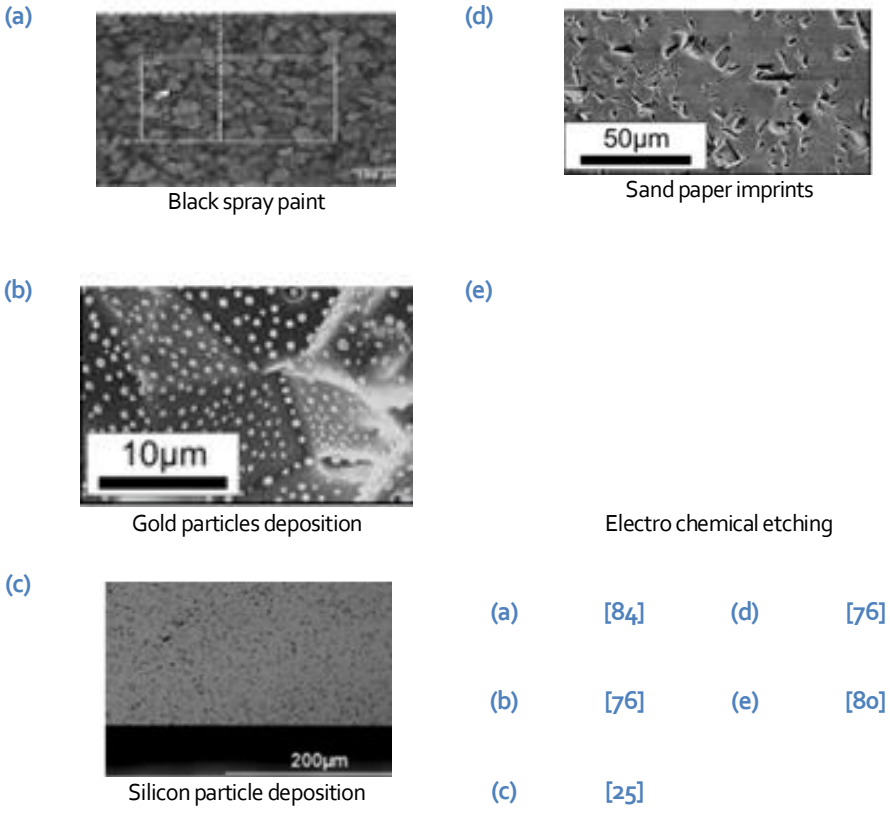

Figure 48: Surface contrast methods

Deliberate light chemical etching can also be done to improve the surface contrast of already visible grain boundaries as done by [80] and [82]. Non-conventional patterning techniques include using FIB indentation and scratching the surface with very fine sand paper [76]. However, when FIB milling is used to provide patterns on the surface for tracking with DIC, the residual stresses and strains produced must also be accounted when strain fields are computed with DIC. A quantitative study of the effects of FIB milling and the optimum procedure to perform FIB has been studied [85].

IN-SITU VERSUS EX-SITU

In-situ DIC is when the images are acquired as the material undergoes loading. This method is live tracking of both elastic and plastic strains. Ex-situ is when the loading is interrupted and images acquired. Both methods have been found useful and have their drawbacks.

As the magnification of an optical device is increased, the area of the specimen that is observed in the field of view decreases as shown in [6, 84]. Higher resolution obtained by magnification is obtained at the cost of area monitored. This phenomenon is explained in Chapter 2. In-situ methods help track the live evolution of strains on grains but when monitoring using a single optical device with high magnification, it may not be possible to monitor completely the region of interest on the material [6]

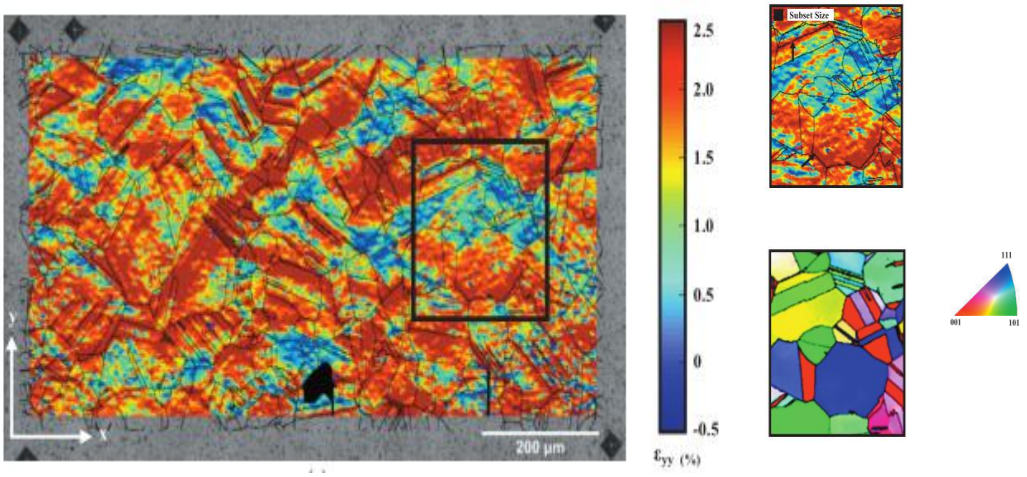

Figure 49: DIC strain maps (Left) with grain boundaries from EBSD (left, zoomed view) [6]

. Ex-situ methods can then be used. The load is removed from the specimen and then multiple images spanning the required area is acquired. These images are merged together using image stitching and DIC is performed on sets of images obtained at various stages, thus making possible high resolution DIC measurements over a large region on interest. 316 of such images acquired were stitched in the work done by [6]. The disadvantage of this method, however, is that only accumulated strain can be identified [6]. For in-situ measurement during loading, this can be implemented by using multiple cameras operating at high magnification adjusted to monitor slightly overlapping areas. 24 overlapping images were acquired where 5 were used for DIC in the work done by Bartali et al.[80].

GRAIN ORIENTATION MATCHING

When care is taken to perform a DIC measurement with exposed grain boundaries, it is possible to identify strains within individual grains. Information about grains orientations in the reference and deformed configuration corresponding to the images in DIC can be correlated. EBSD orientation maps obtained from an SEM has been used by [1, 73, 76, 80] and [6].

CHAPTER 4: *IN-SITU* GRAIN-STRAIN MEASUREMENT OF MAGNESIUM ALLOY

4.1 MOTIVATION

Among commonly used metals, Magnesium (Mg) is about 33% lighter than aluminum and about 80% lighter than steel. It also has high strength-to-weight ratio. [5]. This property has made Mg-based materials a good choice in the automotive industry [86], where light weight magnesium alloys are used to increase fuel efficiency. In addition, Mg is a recyclable material also which makes it also an environment friendly choice.

Wrought MgAZ31 alloy has magnesium, aluminum and zinc as its constituent metals. This alloy has good tensile strength, however, it suffers from low ductility and formability at room temperatures [5]. Specifically, AZ31 is characterized by tension-compression yield asymmetry and plastic anisotropy which explains why Mg alloys have not been widely adopted yet in engineering applications. The mechanical behavior of Mg is attributed to deformation mechanisms that occur at the mesoscopic/microscopic scale at which grain-scale information is important [87]. Therefore, significant efforts have been made over the past years to understand the mechanical behavior of Magnesium alloys, and particularly grain-scale mechanisms that influence bulk plasticity. For example, Choi and his colleagues [5] used the crystal plasticity finite element method to simulate both slip and twinning mechanisms and capture the heterogeneous stress distributions in MgAZ31. Oddershede et al. [64] used high energy X ray diffraction techniques to determine the full stress tensor at the grain scale. Finally Hokka et al. [83] performed macroscopic DIC strain measurements on MgAZ31 alloys in compression.

This chapter describes an attempt that was made to observe grains in MgAZ31 alloy using a 2D configuration of ARAMIS, a commercially available DIC system. The goal was to see if DIC could be successfully implemented to *in-situ* monitor microstructure-properties-behavior relationships in polycrystalline MgAZ31 alloy with an off-the-shelf experimental setup capable to achieve grain-scale strain measurements.

4.2 FEASIBILITY STUDY

SAMPLE PREPARATION:

The as cast MgAz31 alloy was received in the form of a metal block. One cylindrical sample of height 20 mm and diameter 10 mm was cut out from this metal block using Electron Discharge Machining (EDM). Another rectangular sample of 20 mm x 10 mm x 5 mm was also cut out. The samples were then mounted for 24 hours using a mixture of 20% hardener-80% resin. A flat surface was prepared by the process of grinding using P800, P1500 and P2500 silicon carbide abrasive paper. The debris

was cleaned using ultrasonic radiation in alcohol medium. Then it was polished using 3 µm diamond particle suspended solution. It was further polished with colloidal silica polishing suspension.

Figure 50: Mgaz31 sample preparation procedure

50 MM LENSES WITH EXTENSION TUBES:

5 mega-pixel cameras were used with Schneider C-mount 50 mm lenses in the standard configuration of the DIC system. For this application, however, the focal length of the 50 m lens was stretched by the use of extension tubes. These tubes fit between the camera and the standard 50 mm lenses as seen in Figure 51. To this aim, two 40 mm tubes were used; one was a variable length tube which can be extended from its default length of 40 mm to 80 mm. Hence, the total extension tube length that could be achieved was equal to 120 mm.

Figure 51: Left - Variable length extension tube; Right - 50 mm lenses

SETUP AND IMAGE ACQUISITION

Both MgAZ31 samples used had grains size of ~500 µm and the field of view targeted to be measured was 4 mm x 3 mm on the sample surface. To provide the necessary surface contrast, the surfaces of the prepared samples were lightly etched with picric acid. After etching, both samples were observed under an optical microscope. Similar microstructure was seen in both samples.

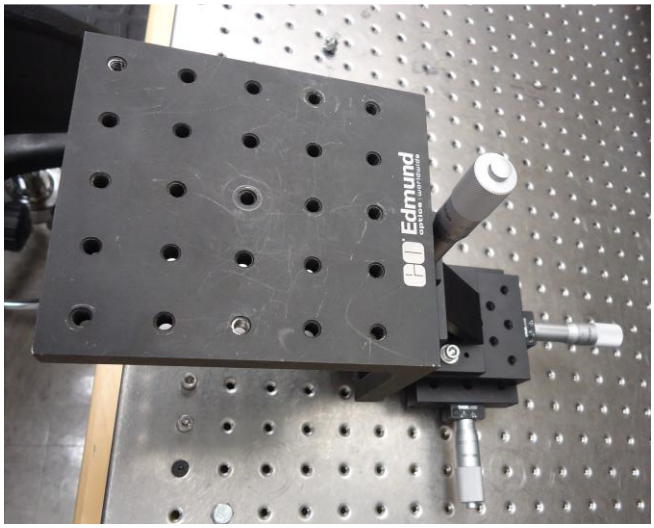

Figure 52: Stage with three axis motion control

The sample was placed on the stage that could be controlled with millimeter level resolution in the X, Y and Z directions (Figure 52). The camera was mounted on the standard camera bar which was in turn supported by a tripod head. Illumination was achieved using the high intensity LED lights that accompany the DIC system. A single camera was connected to the

frame grabber which in turn was connected to the computer with the DIC software interface. The feasibility study first involved obtaining the optimum measuring distance, focal length and aperture opening f-stop number to obtain distinct grain boundaries for the appropriate light sensitivity to reliably map strains on the surface.

Tests were done on two separate samples of MgAZ31:

a. Rectangular block: The optimum measuring distance that yielded a full field lens objective was ~40 mm from the sample. The total extension tube length used was 80 mm with the 50 mm lenses. Aperture f-stop of 5.5 was found to provide acceptable focus and sensitivity to light. Figure 53 shows the grain structure imaged using this combination of lenses and aperture settings. In Figure 54 is seen the strain mapping obtained at a 'deformed' image obtained after a lag of 1 second after Figure 53. A subset of 19 pixels and subset step size of 15 pixels was used. No filtering was applied to the data, while about 21,000 measurement points were obtained using these settings. Due to lack of depth of field at the corners of the lens, the outer regions close to the edge of the field of view had significant noise. However, the middle region of the image had almost negligible noise ~0.2%. This practically means that considering that the metallic specimen is strained to ~15-20%, the effects of the noise would be insignificant. Therefore, the feasibility study on this rectangular sample proved successful and promising for in situ grain-scale strain measurements for this microstructure.

b. Cylindrical block: Since the strain mapping on visible grain boundaries in the rectangular specimen was successful, the next goal was to perform *in-situ* DIC measurements during loading. Hence, a cylindrical sample was prepared for compression loading. The same total focal length of 80 mm, f-stop of 5.5 and a measuring distance of ~40 mm away from the sample were first selected. Subset size and subset step size were chosen based on the post processing of the feasibility study results, yielding about 21,000 measurement points on the surface. Strain mapping with acceptable noise levels was obtained at the 'deformed' image (Figure 56) which was acquired after a lag of 1 second from reference image (Figure 55). However, the grain boundaries were not visible at all in this specimen.

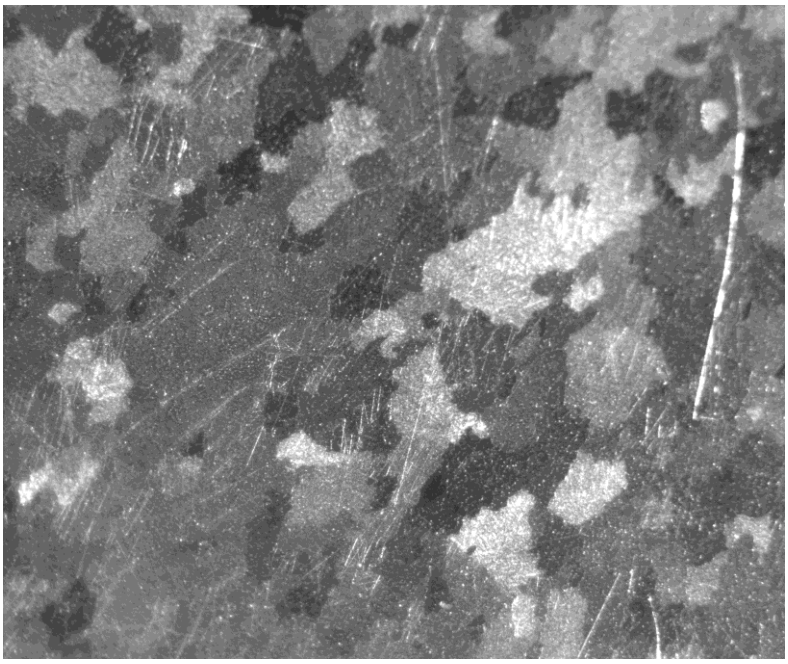

Figure 53: MgAz31 ~500 µm grains; ~4 mm region of interest

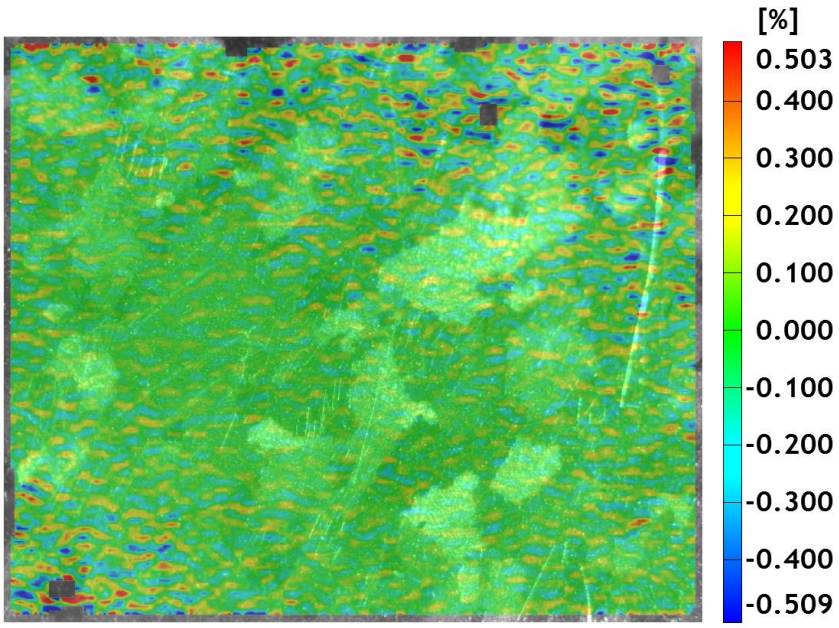

Figure 54: Strain noise as seen in feasibility study

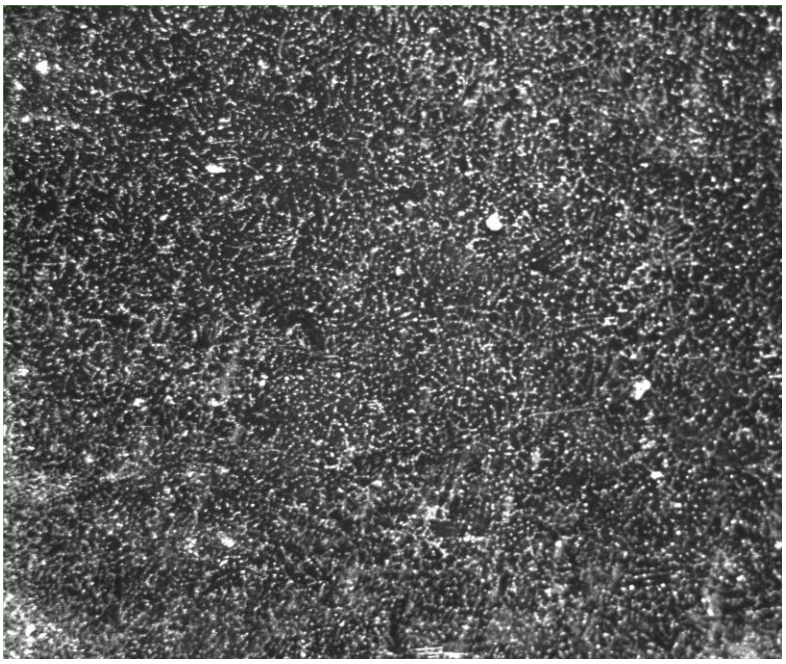

Figure 55: Cylindrical specimen - surface grain structure

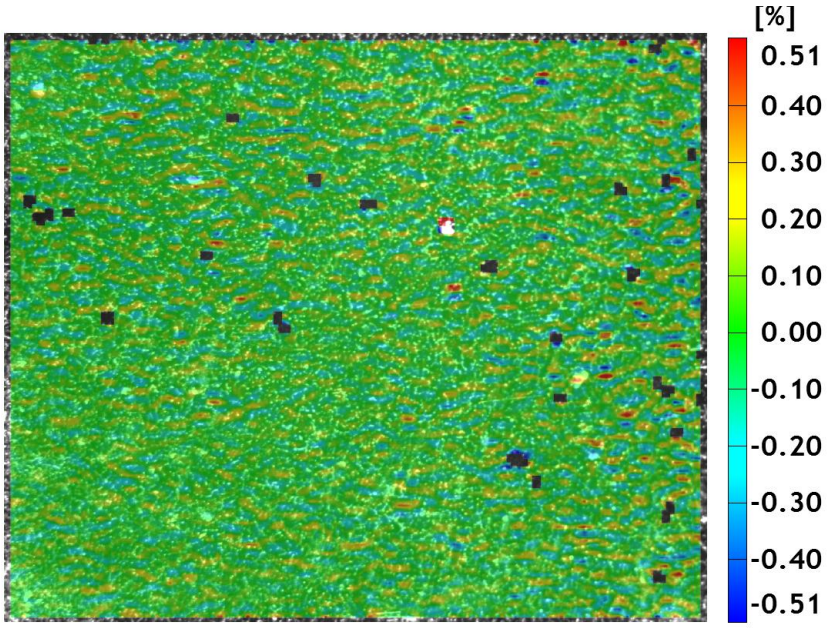

Figure 56: Cylindrical sample - strain map

4.3 DISCUSSION AND CONCLUSIONS

The rectangular sample showed distinct grain boundaries, however, the compression sample prepared later did not show the same. When the cylindrical sample did not show distinct grain boundaries, parameters of the system setup were systematically experimented. Several combinations of light sources and locations, f-stop values from 4 through 11, focal length from 80 mm through 120 mm and measuring distance 30 mm through 50 mm measuring distance were tried. In such a case, even the bare minimum of strain mapping as seen in Figure 56 could not be achieved

Several factors may be contributing to the fact that the grain boundaries are not seen distinctly in the cylindrical sample. Lighting positions were not fixed for both tests in the same way. The best lighting position were picked by trial and error by monitoring the live feed from the camera to see if the grain boundaries were visible. The second factor can be the etching. Though both samples were etched using picric acid, the depth of etching may not have been the same as it was done manually and not in a controlled manner. The grain formation in material is fairly random. The grain growth in these samples was not controlled in any way to obtain similar orientations of grains. The individual samples may have responded differently to polishing and etching treatment.

It can be said that this approach is successful to an extent that grain boundaries can be seen and can be strain mapped directly using a commercial DIC system (Figure 53 - Figure 54). However, there is room for improvement in terms of repeatability. The etching process and the lighting processes must be calibrated so that the sample is etched the same amount every time and same lighting obtained every time. The field of view for this measurement is estimated to be about 4-5 mm, however, the exact field of view for this measurement is not known yet. Following a calibration process for 2D Digital Image Correlation prior to making a measurement is also strongly suggested.

The repeatability shortcomings of this procedure is addressed in the next two chapters where more consistent approaches are used to obtain full field strain maps at much higher magnification for grains of smaller size.

CHAPTER 5: *IN-SITU* GRAIN STRAIN MEASUREMENTS NEAR THE FRACTURE ZONE OF AN ALUMINUM ALLOY

5.1 OVERVIEW AND LENS CONSIDERATIONS

This chapter describes the procedure followed to quantify grain strains at the microscale using an augmented *in-situ* Digital Image Correlation setup. A Compact Tension (CT) specimen made of aluminum alloy Al2024 was designed and fabricated based on ASTM E647-08 and was first fatigue pre-cracked to a length of 1.2 mm. The microstructure near the pre-crack region, comprising grains with an average size of 75 µm, was exposed by grinding, polishing and etching. The natural pattern observed on the specimen's surface after etching provided sufficient surface contrast for DIC measurements. ARAMIS, a commercially available DIC system, was modified and augmented by the use of long distance optical microscopy lens to monitor a region of 870 µm x 730 µm near the pre-crack. The sample was subjected to displacement controlled Mode I loading using an MTS servo hydraulic testing frame while *in-situ* acquiring images using the DIC system. In addition, acoustic emission (AE) was recorded using a multichannel data acquisition system and piezoelectric sensors to correlate the fracture process with nondestructive measurements. Strain values were obtained at the crack tip; alternating tensile and compressive strains were seen over grains at regions isolated from the propagating crack tip. Furthermore, the initiation of AE hits was correlated with strain development and onset of cracking.

LENS CONSIDERATIONS

The optimal lens system that could be used with the 5-mega-pixel CCD cameras of the ARAMIS was researched. The lens was required to monitor a region of interest around 1 mm^2 to see several ~75 µm sized grains on the surface. The following criteria had to be met by the chosen lens system:

- The ability to achieve small fields of view is determined by lenses with different magnifications positioned in series with distance between them. The larger the distance between the lens and the sensor, the smaller the field of view it can achieve. As such distances increase, however, less light reaches the cameras sensor. Consequently, the lens must provide sufficient light sensitivity at high magnifications for small fields of view.
- The next criterion for the lens is quality of focus. Not only must the grains be in focus but the features within the grains must be clearly resolved with acceptable noise to allow for pattern matching at the sub-pixel level.

- Depth of field is also important since the grain measurements would be *in-situ* with the complication that the sample could move a few microns in our out of plane, which could be enough to cause loss of focus and make the underlying correlation algorithm in capable to map strains in the region of interest.

LENS SELECTION

Initial trials were done using a lens of 50 mm focal length with 100mm extension tubes to increase the operation focal length. This trial provided a ~1 mm^2 field of view on the material surface. However, the optical quality was not satisfactory as the image focus was lacking in sharpness. The sensitivity to light was lacking even with the use of the integrated high intensity LED illumination of the ARAMIS hardware. This initial trial confirmed that the use of the 50mm lens with extension tubes to observe the microstructure would not yield reliable results.

A second attempt using the Infinity K2 long distance microscope system (Figure 57) was made. The K2 lens system has two configurations: with and without the S Lens in-system [88]. For this measurement, the S lens in-system configuration was used and the system was operated in the high-power micro mode by using a 5X zoom Archovid™ adapter (Figure 58) at the objective of the lens system. Several accessories and adaptive tubes along with rotary focus and aperture control allow for sharp focus with sufficient depth of field for fields of view from 2mm to 250 µm with ample light sensitivity. The lens system was mounted on to a 5 megapixel Baumer TXG Ethernet camera using a C-mount adapter at the eyepiece of the lens system.

Figure 57: DIC camera augmented with the K2 long distance microscopy lens, both mounted on an optical table

Figure 58: Co-axial Illumination adapter and Zoom module

The drawback to the K2 is that due to its length and weight it must be supported independently of the camera since it could bend and damage the interface between the two or cause misalignment.

5.2 EXPERIMENTAL PROCEDURE

SPECIMEN PREPARATION

A notched aluminum 2024 alloy CT test specimen was cut using EDM. The dimensions of this specimen adhered to the pertinent testing standards as specified by ASTM E647-08.To ensure stable crack growth with application of Mode I loading, a pre-crack of about 1.2 mm was introduced at the tip of the notch by fatigue Figure 59. The cyclic loading was based on ASTM criteria of $R = \frac{\sigma_{min}}{\sigma_{max}} = 0.1$; where $\sigma_{max} = 600\ N$.

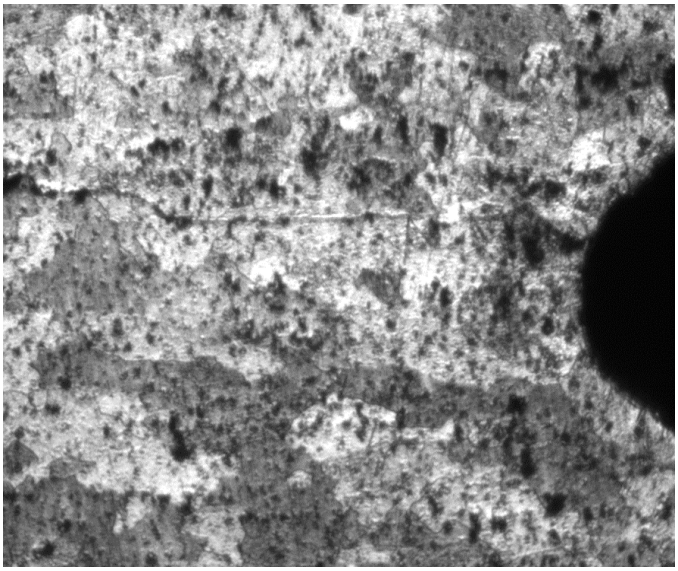

Figure 59: Surface contrast at the crack tip; Precrack visible; FOV: ~900 x 900 µm

The grain structure around the pre-crack was exposed by grinding with 600, 800 and 1200 sand paper followed by polishing with a sequence of diamond solutions hiving 9 and 6 µm particles. Keller's reagent was then used to etch the surface. Grains observed were in the range of 75 µm in diameter. The etched surface and the fatigue pre-crack are seen clearly in Figure 59.

When first observed under the microscopic lens, a natural pattern was identified on the surface due to the exposed microstructure. To perform DIC measurements, a feasibility study was carried out to determine if further particle deposition or speckle patterning was necessary to obtain a finer distribution of contrast. The CT sample was imaged using the DIC system and then processed for strain mapping while the subset size, step and accuracy tolerances were adjusted to create different point mesh densities. Finally, system noise analysis was done to determine the best settings to use for such measurements. It was concluded after this feasibility check that the chemical etching without any further applied patterning was sufficient to achieve validated strain mapping using directly the microstructure as contrast.

DIC Parameters

Subset size and Step: A 5 mega-pixel camera was used for the monitored field of view of 870 µm x 730 µm. The images acquired in the feasibility steps described earlier were processed using the subset size and step combinations shown in Table 8. It was found that, as the chosen mesh becomes finer, the strain noise increases. Therefore it is desirable to identify the settings that provide the best compromise between local sensitivity and strain noise. From the data presented in Table 8, the optimum subset size for DIC post processing was 100 pixels with distance between adjacent subsets equal to 51 pixels. These settings provide a data set of over 2000 measurement points with an equivalent strain gage length of 38 microns and 0.37 µm/pixel. Note that with 100 pixel facets, each measurement point is accurate to 1/10,000 of a pixel.

Table 8: Strain noise based on facet size and step for ~1 mm x 1 mm field of view

Facet size	100			75			50		
Facet step	25	51	75	19	38	56	13	25	38
Overlap %age	75	49	25	75	49	25	74	50	24
# of 3D Points	6155	2247	1109	12054	2969	1382	26804	7161	3104
Strain Noise (%)	0.017	0.009	0.001	0.025	0.013	0.008	0.134	0.075	0.02

PIXEL CONVERGENCE THRESHOLD: An accuracy threshold of 0.100 pixel was used to define convergence. This setting was significantly different than the default value of 0.04 pixels due to the large size of subsets and spatially disperse surface pattern.

STRAIN SETTINGS: A strain window of 3 x 3 measurement points from the measurement cloud was used to compute strains over the displacement field. A 35 % validity quote was used. This means that at least 35 % of the 9 points in the 3 x 3 window were needed for strain measurements without edge noise or unreliable data.

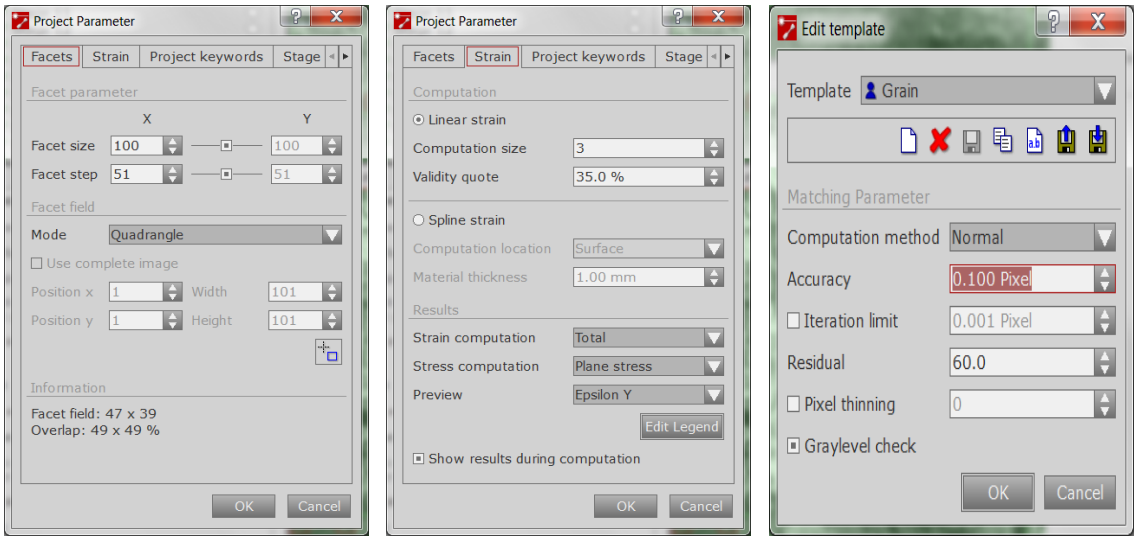

Figure 60: Optimal DIC settings for post-processing

PRACTICAL CONSIDERATIONS

To perform this measurement successfully the optimal loading range, mechanically stable system configuration, lighting and focus stabilization methods had to be determined.

LOADING RANGE: The loading range at which stable crack would occur was to be obtained before grain scale strain measurements could be achieved at the tip of the pre-crack. Experience about the appropriate loading range was gained from prior tests that used similar CT samples with the one used in this thesis.

MECHANICALLY STABLE CAMERA CONFIGURATION: During testing, the part would be rigidly gripped in a universal test machine and tensile force would be applied. If vibrations were to occur, it could be caused by the test machine and the augmented measurement setup. Therefore, the DIC system had to be made insensitive to such vibrations. Specifically, it was

important to ensure that the chosen long distance microscopy lens used had a stable connection to the DIC system and was mounted securely. The typical tripod-mounted configuration of standard DIC systems could not warrant the required mechanical stability when using a long distance microscope lens. If the camera was mounted on a tripod with a long distance lens, the camera and lens configuration could be damaged by the weight exerted by the large lens. Hence, it was chosen to mount both the camera and the long distance microscope on an optical table. This arrangement provided adequate mechanical stability and proved heavy enough to damp vibrations in the camera-lens system.

ILLUMINATION: It proved challenging to find appropriate lighting methods suitable for the use of the long distance microscope and the ~1 mm^2 regions of interest. Typical lights used for DIC are white light LED arrays designed to evenly distribute light across an area. In order to make micro-measurements the light needed to be focused and projected to an area similar in size to the cameras field of view. This was achieved by the use of a co-axial illumination module seen in Figure 58 with the K2 lens. An instance of the obtained illumination is seen in Figure 61.

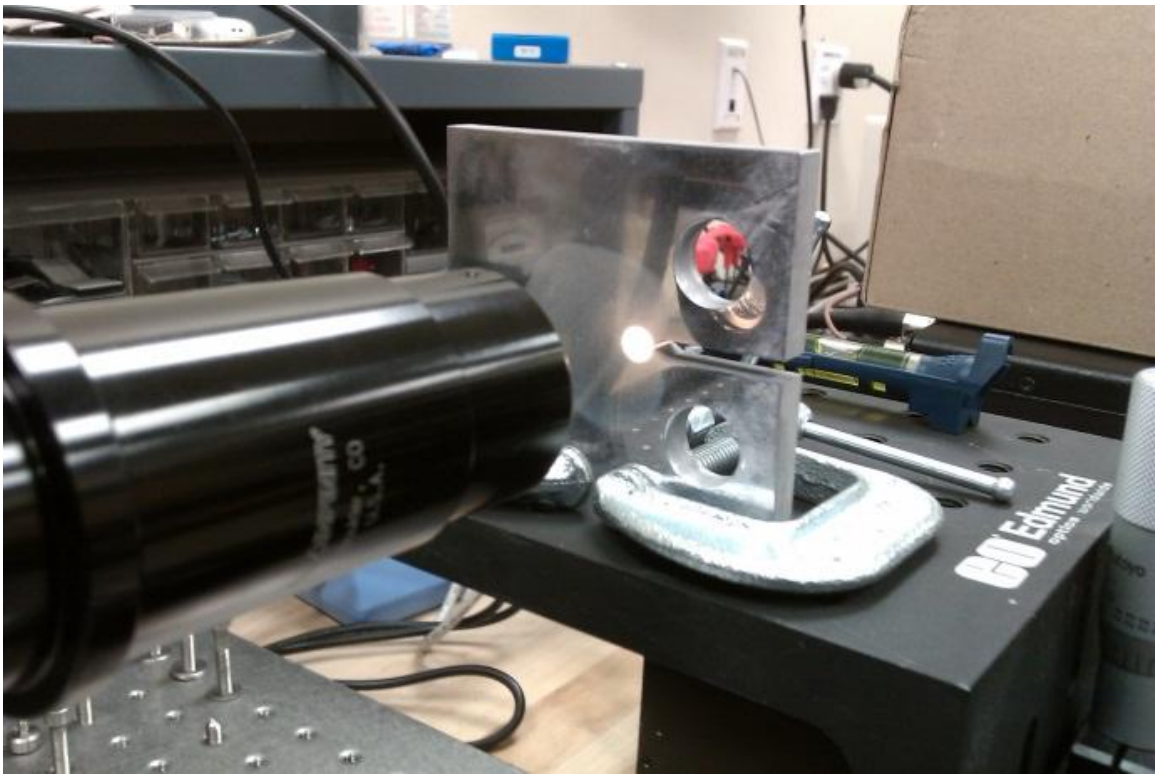

Figure 61: Close-up view of K2 lens viewing the crack tip, coaxial Illumination also seen

FOCUS DURING DEFORMATION: The tip of the crack was expected to move within the field of view during the test. In addition the sample could slightly deform out of plane. It was a priori well understood that even small deformations in the macroscale could cause significant microscale deformations, causing the DIC measurement system to go out of focus. To this aim, the lens assembly had to be capable to move to allow for manual searching of the crack tip. In the future work described in Chapter 7 in this thesis, a procedure to make this step fully automated is described. Furthermore, the system must be capable to move laterally and longitudinally both in plane and out of plane to track the crack tip at the same time as it stays in focus. This was enabled in this test by mounting the lens camera system on a 3 axis screw rotation-driven stage which enabled in plane and out of plane lateral and longitudinal, motion. Note that rather than focusing the lens at every step using the lens focus system, the working distance was controlled by being capable of making *in-situ* slight modifications.

LOADING SETUP

The final test setup had the camera secured to a 3-axis stage and mounted to an optical table. This allowed the camera to move in all directions required to easily focus on the specimen at the region of interest around the crack tip. The Infinity K2 lens was supported by a ¼-20 fixture at the center of its mass. A metal-halide light generator supplied the necessary high intensity illumination and was fed into the microscope's co axial illumination fixture with a flexible optical fiber cable. This was placed on another table away from the optical table to avoid high frequency, and low amplitude vibrations from its fan motor. The optical table supporting the system was placed on a solid worktable and mechanical stability of the table was ensured.

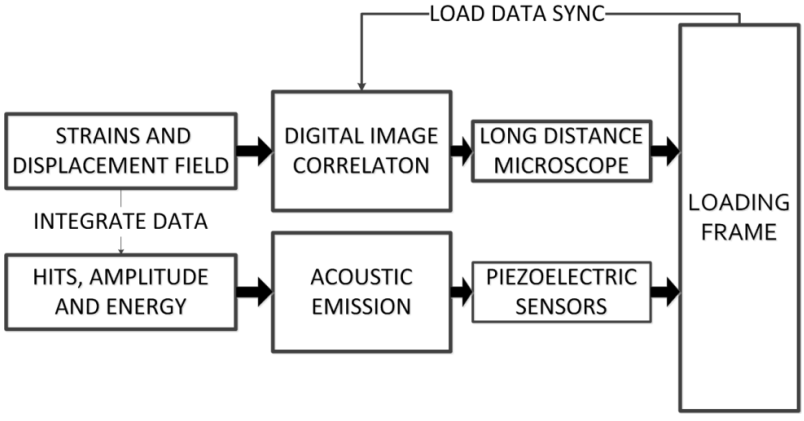

Figure 62: Schematic of experimental setup

Figure 62 shows a schematic of the experimental setup. A displacement controlled monotonically increasing Mode I (in-plane tension) loading at a rate of 0.5 mm/min was applied to the CT sample which was gripped by a pair of arms from an MTS 810 piston pump loading frame. The DIC camera/lens system was positioned in front of the test sample as seen in Figure 63.

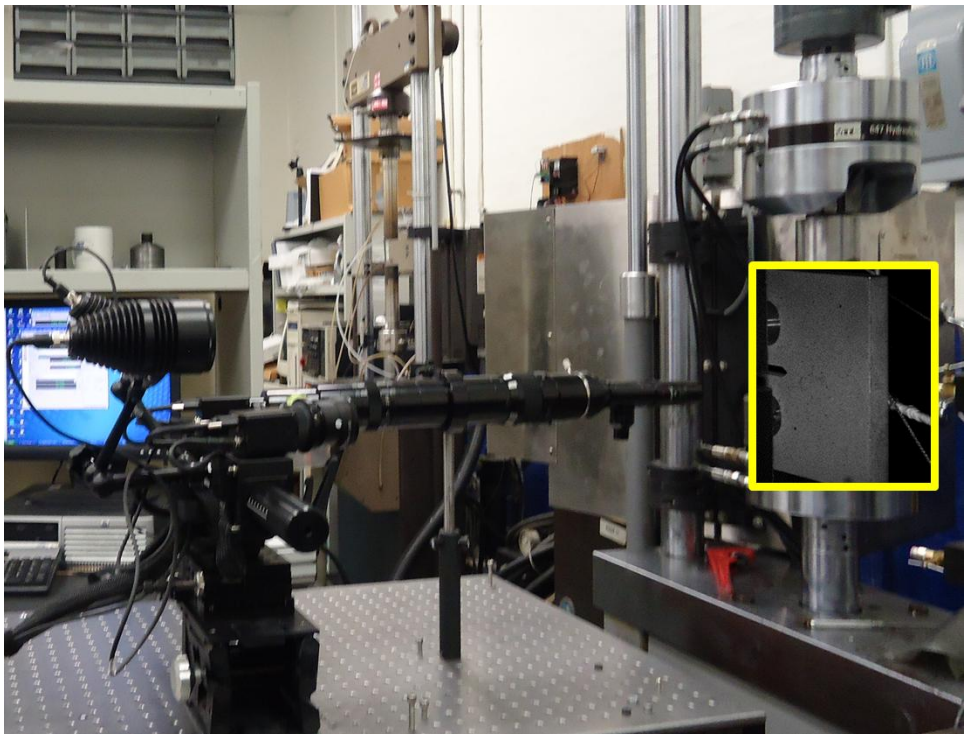

Figure 63: DIC system setup with the long distance microscope; Inset: CT sample with AE sensors attached

The height of the grips was adjusted such that the etched region of interest was visible to the lens. The field of view observed was 870 µm x 730 µm. The measuring distance from the objective of the microscope to the specimen surface was 25 mm. Load was applied in five steps; it was paused between the steps to adjust the observed region to the tip of the propagated crack. Images were recorded with a sample rate of 3Hz. Piezoelectric sensors were glued on to the CT sample to monitor acoustic activity during crack propagation using a multichannel data acquisition system.

5.3 RESULTS

Figure 64 shows the progression of the crack tip through the five stretches of loading. The first visible crack opening was seen in the third part of loading in the 7^{th} image acquired (Figure 64). in terms of strain field, however, crack initiation can be seen distinctly at ~2400 N corresponding to the 106^{th} image in the second stretch of loading (Figure 65) and is identified by the

high strain concentration at the tip of the pre-crack (Figure 65). Light and dark spots are seen in Figure 64; the various features seen here maybe grain boundaries or the bulk of the grains with contrast on surface imparted from chemical etching. It is hard to differentiate the exact grain boundaries and tell one grain apart from the other in these images. However, strain localizations in the range of the size of grains as seen in Figure 65 gives an idea about the interaction between grains and the inhomogeneity in the strains in such polycrystalline phases. The formation and coalescence of voids can also be identified in the third part of loading from the 26th, 44th and the 54th images in Figure 64.

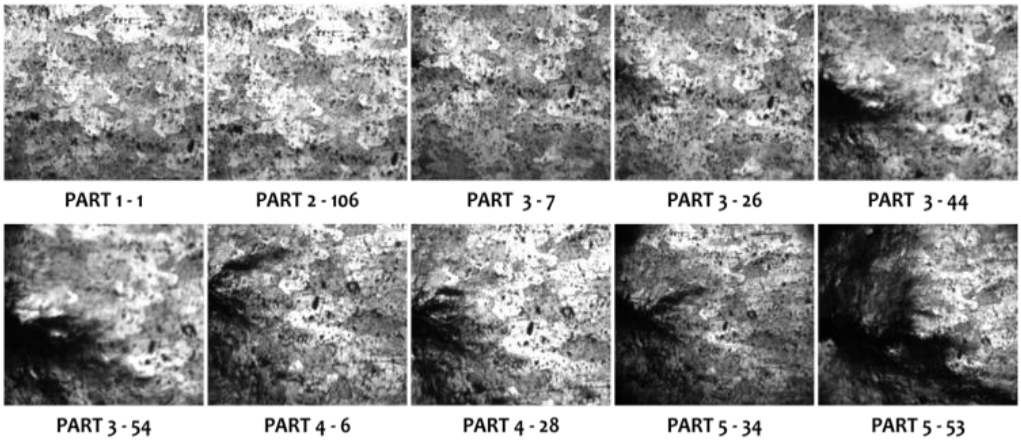

Figure 64: Progression of surface grains

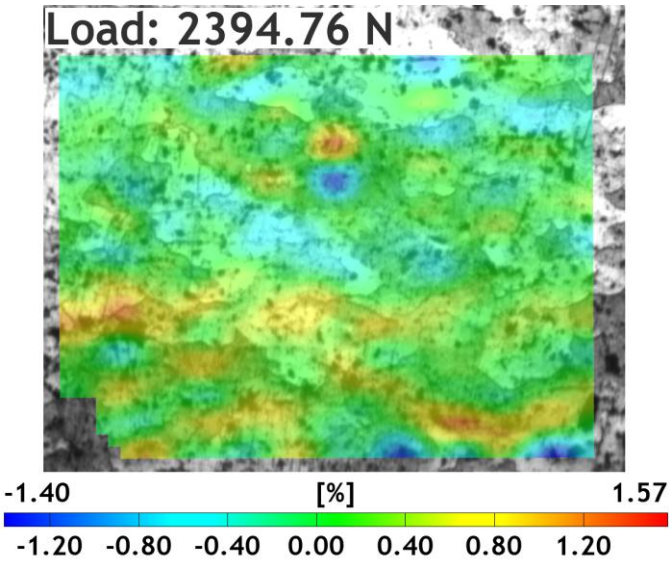

Figure 65: Strain concentration around crack tip at initiation

Evolution of Strains

As the load increased, the strain around the crack tip increased and then the crack propagated around an adjacent grain. Figure 66 and Figure 67 show the progression of strain as a factor of the crack opening displacement. Figure 68 is a plot of the amplitude of acoustic emission recorded for the second loading session. Average strain in the loading direction (Y axis) obtained from DIC is plotted here. There is good agreement between crack tip evolution and AE which showed that as the load applied increases both the strain of the whole field of view increases and the amplitude of the recorded emissions increased simultaneously.

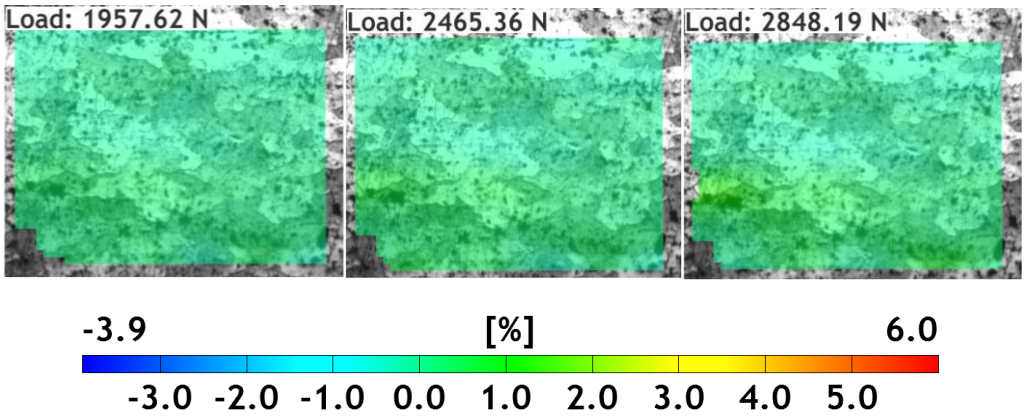

Figure 66 – Epsilon Y plots at 250 nm, 500 nm and 1 µm COD

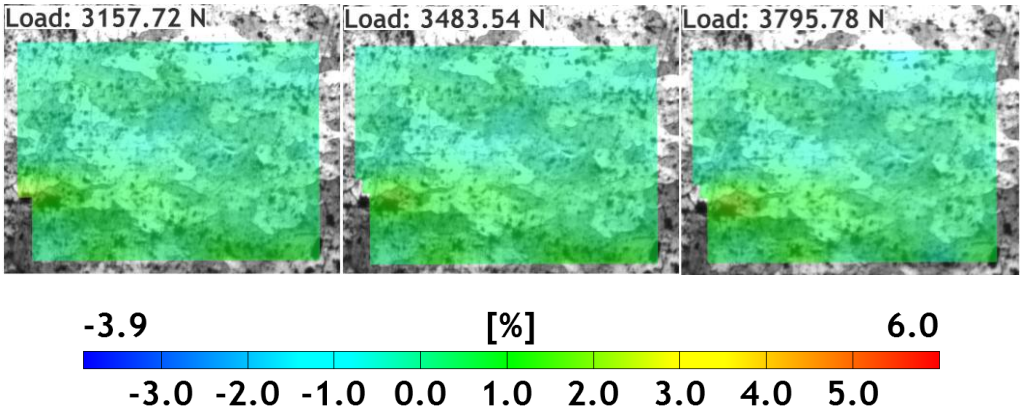

Figure 67 – Epsilon Y plots at 1.51 µm, 2 1 µm and 2.51 µm COD

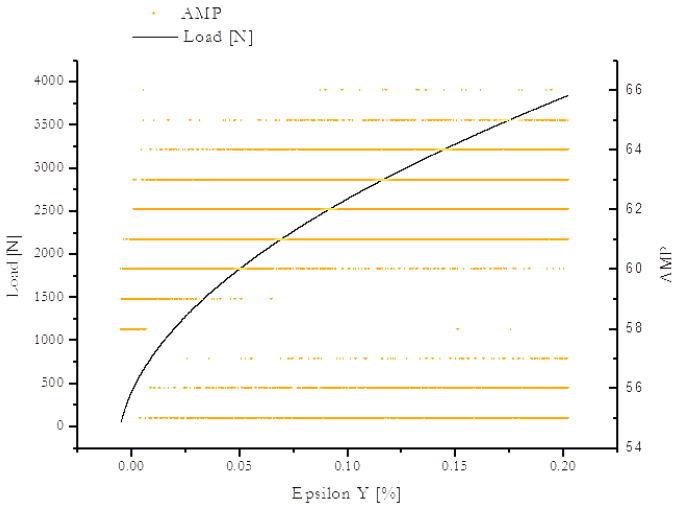

Figure 68: Average strain measured by DIC correlated with the amplitude of acoustic emissions

DISPLACEMENT IN LOADING DIRECTION:

Rigid body motion correction was used to reveal the true local displacements at the grain scale. The most likely crack path was revealed by this calculation as material points above the crack were moving upwards and points beneath the crack were moving downwards. The green areas that show no displacement between these two regions is the expected crack propagation path. It can be seen in Figure 69 that such areas of no displacement were not necessarily oriented along grain boundaries.

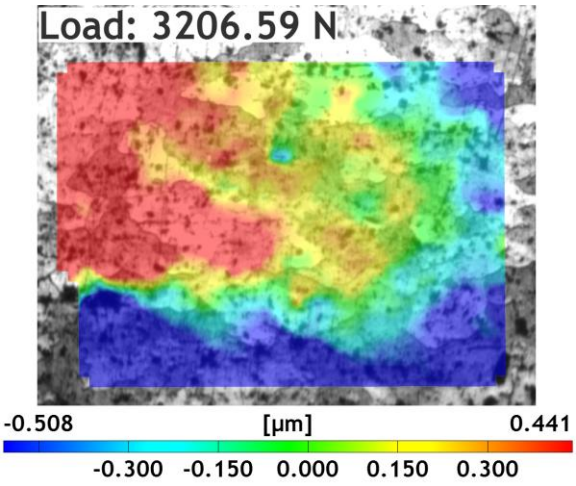

Figure 69 – Displacement Y plots show development of crack path among grains

CRACK OPENING DISPLACEMENT VS. LOAD

A virtual extensometer initially 96 microns in length, was placed with its ends on either side of the crack. The crack opening displacement and strain measured along this virtual extensometer was plotted against load in Figure 70. It can be seen that up to 1600 N, the crack does not open. At 2000N the extensometer was at 0 .25 microns. At 2600N the crack begins to open much more rapidly as seen by the change in slope of the graphs shown in Figure 70.

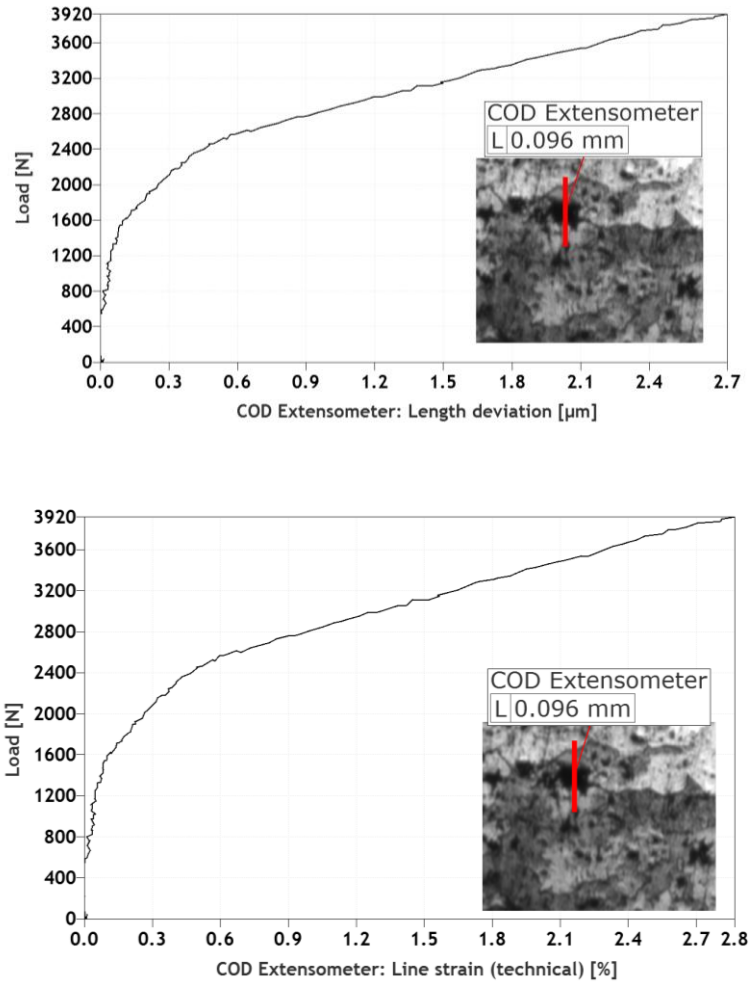

Figure 70 – a) COD vs. Load b) Strain from Crack Opening vs. Load

5.6 DISCUSSION & CONCLUSIONS

STRAIN HETEROGENEITIES:

At the microscale, there are in-homogeneously varying regions of tension and compression within and in between fairly distinguishable grains as seen by the red and blue color regions in Figure 71. There are certain noisy areas which must not be mistaken for strain distributions as shown in Figure 72.

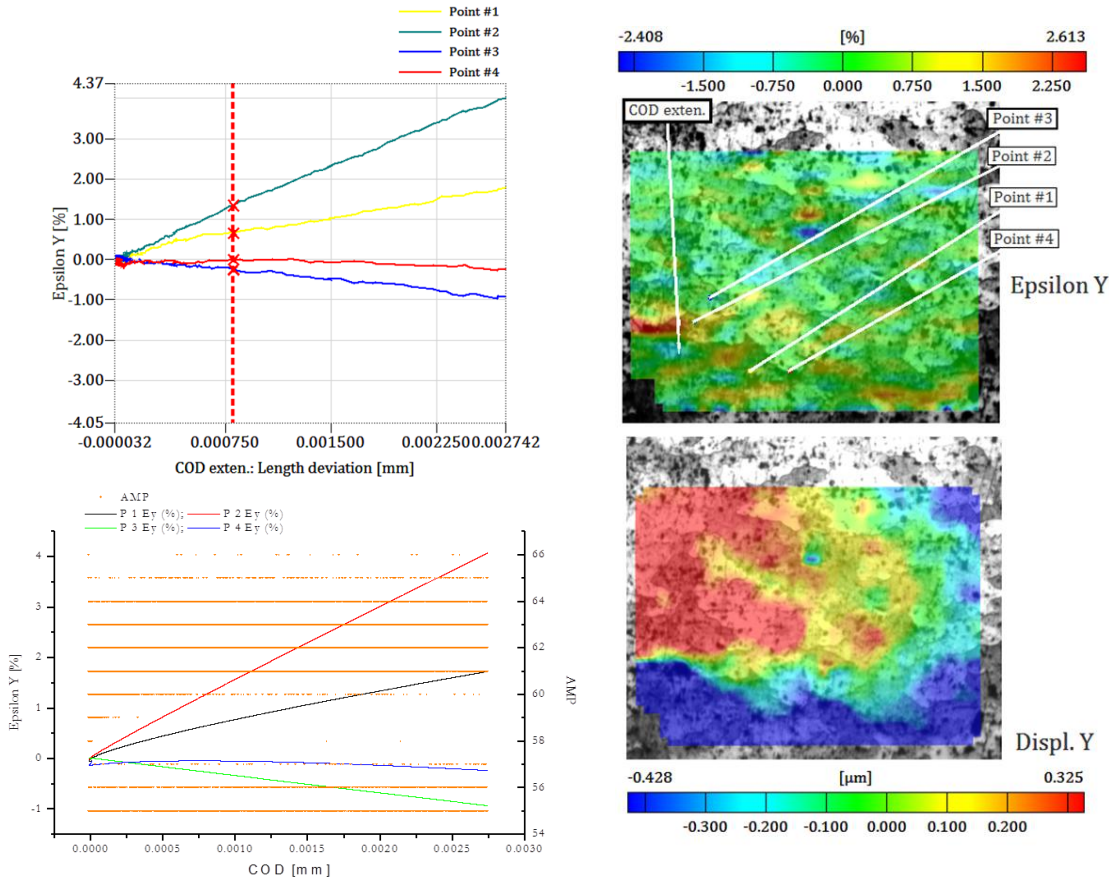

Figure 71: (left top) Evolution of strains along points on the specimen (left bottom) Correlation with amplitude of acoustic emission (right) snapshot of strain (top) and displacement (bottom) field at 2728.72 N

Also seen in Figure 71 is the correlation of the strain growth at the selected grain points from DIC with acoustic emissions recorded from piezoelectric sensors. As the strain increases, there seems to constant acoustic activity within the material, signifying changes in the internal structure of the metal.

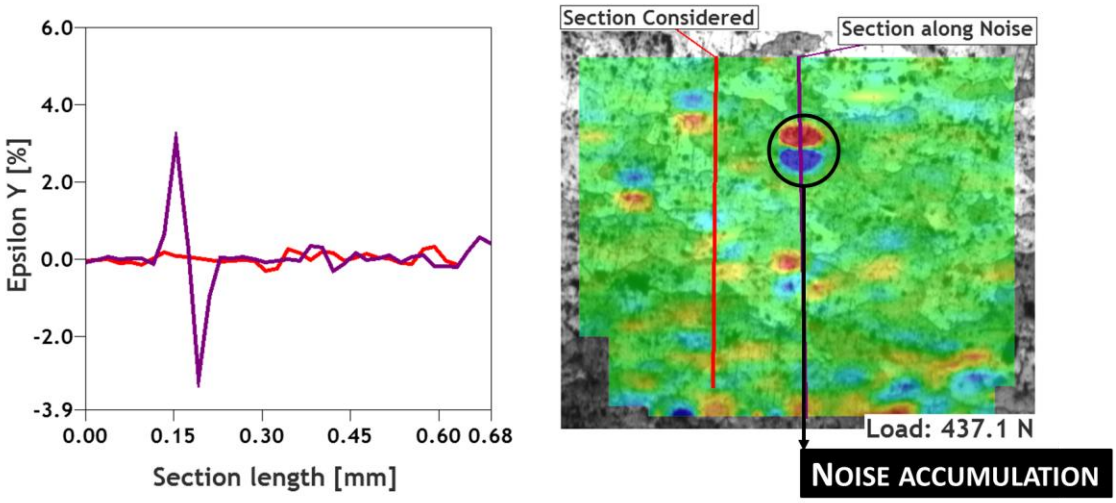

Figure 72: Strain along a section and strain noise spots

Figure 72 shows the strain plots along two sections considered. Some parts of the image show localizations of very high strain even at very low load being applied. One section in Figure 72 is positioned across these zones and the plot in the left corresponding to this section shows high strain magnitude. This clearly is noise in the measurement. These noise zones are persistent until higher strains develop in the material at a much later stage. One such stage is shown in Figure 73.

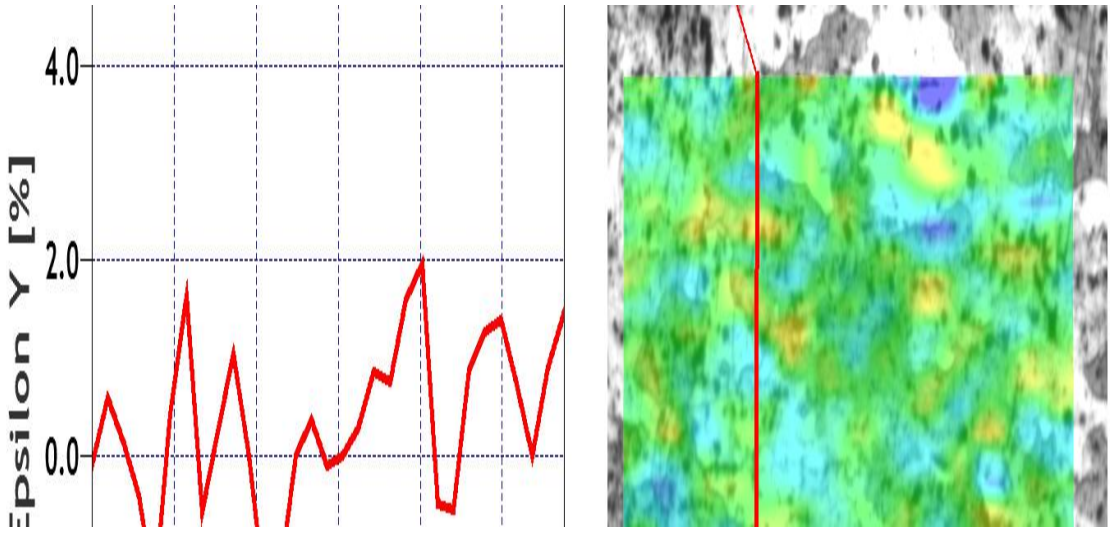

Figure 73: Strain heterogeneity along a considered section

In Figure 73, the strain plot in the left shows the distribution of strain in the section considered on the material in the right. The considered strain is in the direction of loading and it is seen that along this section, the strain does not vary smoothly. The gradients of strain are non-uniform and the distribution of the strain is heterogeneous. Compressive as well as tensile strain is seen alternating along the section considered in Figure 73.

COMPARISON WITH MACROSCALE DIC

In the macro scale CT Mode I loading done prior to the measurements reported in this thesis, crack opening was observed at around 7000 N as seen in Figure 74. The strain distribution at tip of notch can also be seen here. In this experiment, however, we were able to see cracking readily at a load of ~1200 N (Figure 70). It should be noted that the displacement/strain/crack tip motion capabilities in the macroscale experiments was not as advanced as in the procedure described in this thesis. With this current test setup having a micron level field of view, we were able to see the pre crack tip at early stages that could be associated with the initial stretching of the previously formed crack faces due to fatigue. In the experiments described in this thesis, reliable strain and displacement measurements in fields of view of ~900μm, were successfully accomplished in addition to observing crack growth around grains in an Al 2024 CT specimen.

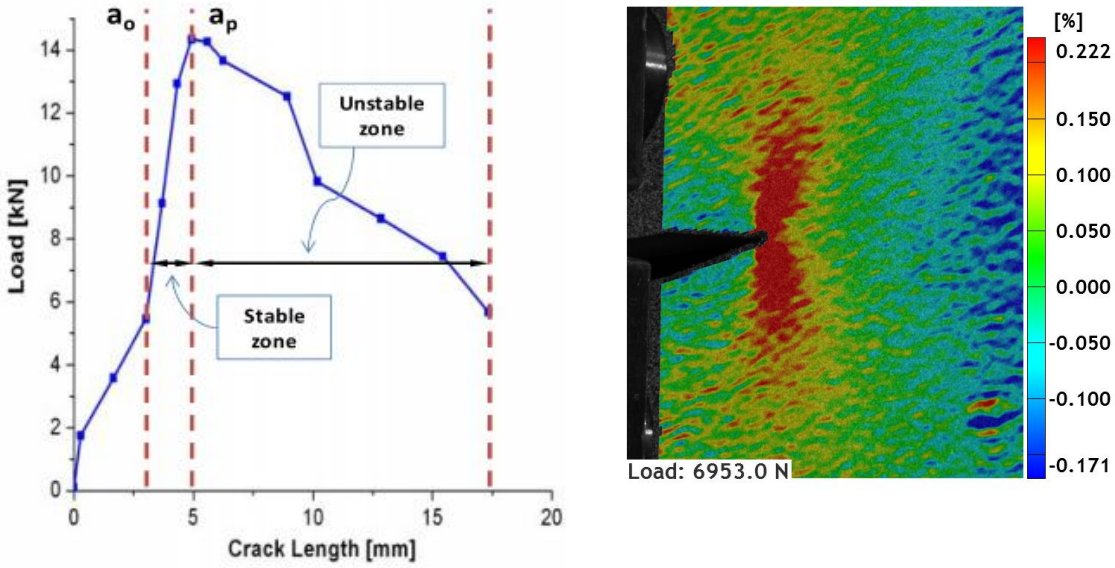

Figure 74: Left - Onset of stable cracking at ~7 kN; Right – Distribution of strain in the loading direction at crack initiation

CHAPTER 6: SEM DIC

6.1 IN-SITU SEM TESTING MOTIVATION

Loading frames such as the ones used in Chapter 5 are generally appropriate for macroscale material testing. In the previous approaches mentioned in the thesis, loading is done using an MTS servo-hydraulic load frame. During loading, grain behavior at the microscale was imaged *in-situ* using cameras with extended lenses and long distance microscopes. These methods, however, are not without their shortcomings. The extension tubes cannot be consistently applied to specimen of varying grains. Illumination needs case-specific adaptations for grain scale measurements using extension tubes as even different samples from the same batch have grains in different directions. In addition, long distance microscope lenses are extremely bulky and unstable,, while they are also very sensitive to mechanical vibrations. Furthermore, extra care must be taken to have the lens perfectly stable as even small mechanical perturbations can affect the measurements microscopic fields of view are monitored.. Moreover, the length scale difference between macroscopic loading and microscopic observation causes sampling problems. This was particularly seen in chapter 5, where loading had to be imposed in steps and the load-holds between steps were used adjust the field of view based on the crack tip motion

To further improve and extend the use of DIC for in situ grain scale measurements, state-of-the-art loading procedures combined with electron microscopes can be used to track strain evolution e.g. of polycrystalline metals. With the advent of micro tensile stages, such as the one shown in Figure 75, novel methods for material characterization have been developed. This kind of *in-situ* material tests inside an electron microscope are advantageous in many ways and bypass the difficulties faced in performing *similar* measurements using a standard servo-hydraulic loading frame.

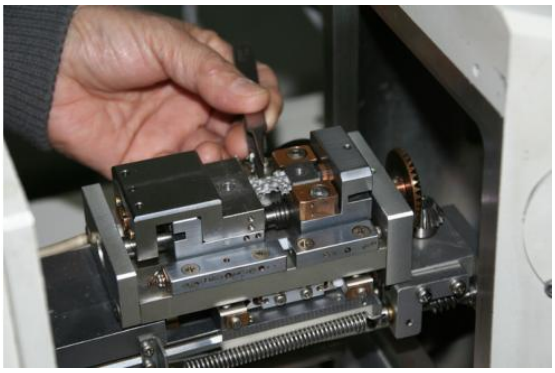

Figure 75: Loading device with sample mounted inside the observation room of an SEM [89]

The use of state-of-the-art electron microscopes can be an invaluable extension to the DIC process to track strain evolution in the grains of polycrystalline metals. With the advent of micro tensile stages, novel methods have been developed for material characterization involving the use of these micro tensile stages inside of electron microscope. *In-situ* material tests inside an electron microscope are advantageous in many ways and bypass the difficulties faced in performing *in-situ* measurements in front of a macroscopic loading frame.

6.2 Background and Development

Widespread applications of microscale thin films and nanoscale carbon fibers necessitated material characterization procedures at micrometer and nanometer length scales, since material properties obtained at the macroscale do not prove to be reliable properties at this level [90]. The techniques that previously existed did not provide the necessary combination of force control, displacement control and full field imaging for thorough in-situ measurements. This led to the development of microscopic electromechanical testing systems. In 2001, Haique and Saif [90] presented for the first time the use of Micro Electro-Mechanical Systems (MEMS) for load and displacement controlled uniaxial tensile and bending tests for aluminum thin films inside of an SEM. They fabricated a lateral comb-drive actuator to generate a maximum force of 382 µN with maximum allowable axial displacement of 10 µm and calibrated it with a calibration beam of 517 µm x 1 µm x 20 µm dimensions.

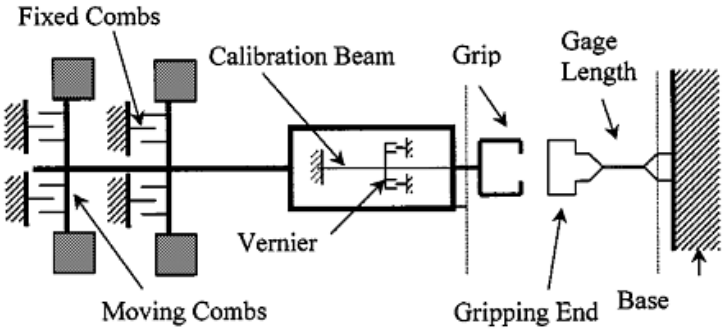

Figure 76: Schematic of a comb-drive load cell [90]

In 2005, Zhu and Espinosa [91] report the application of in-situ mechanical testing devices within an SEM and a TEM for material characterization of poly-silicon thin films, metallic nanowires and carbon nanotubes. Two MEMS based load cells

were fabricated: comb drive electrostatic actuator for load controlled tests and in-plane actuator for displacement controlled tests. They had variable nN load resolution and it was calibrated with reference to features in the SEM's movable shuttle. In 2008, Song et al. [89] reported an *in-situ* displacement controlled compressive test of aluminum foams in a region of interest of 4 mm x 6 mm x 4.5 mm inside an SEM. In the same year, Kolluri et al. reported characterization of delamination by *in-situ* SEM observations. A mixed mode bending apparatus which would fit in the SEM was fabricated and used in testing of a multilayered polymer to observe delamination in bilayer of brass.

In 2007, Sutton et al. studied in great detail [92, 93] the performance of Scanning Electron Microscope and its applicability for *in-situ* Digital image Correlation. An intensive study for image quality, distortion of lens systems in the SEM and drift in images at high magnifications was performed and a calibration model for 2D DIC from SEM image was put forth. A miniaturized load cell mounted inside an SEM was used to quantify the strains in Al2024 – T4 alloy.

The applicability of SEM image DIC and the microscale load frames was realized to quantify strain localizations and inhomogeneities in polycrystalline material .In 2009, Tschopp et al. [1] used the *in-situ* SEM DIC combination to obtain strain maps in a forged polycrystalline Nickel based superalloy using a screw driven 1000 lb. under tension. In 2011, Jin et al. [74] used in-situ SEM DIC methods to obtain strains on the microstructure at the tip of crack in Al6061 alloy in a three point bend test.

6.3 EQUIPMENT SETUP

SCANNING ELECTRON MICROSCOPE

A scanning electron microscope (Figure 77) has a source of electron radiation which radiates electron onto a region of interest in a specimen placed on the stage. This incident beam of electrons interacts with the atomic structure of the specimen and it may be absorbed or scattered. Other radiations such as x-rays are also emitted. There are two types of scattered electrons that pertain to obtaining imaging for Digital Image Correlation. They are secondary electrons, which are electrons ejected from the electron cloud in the specimen, and backscattered electrons, [92] which are the incident electrons scattered due to elastic collision with the atoms of the specimen. There are separate detectors for both kinds of electron rays as seen in Figure 77.

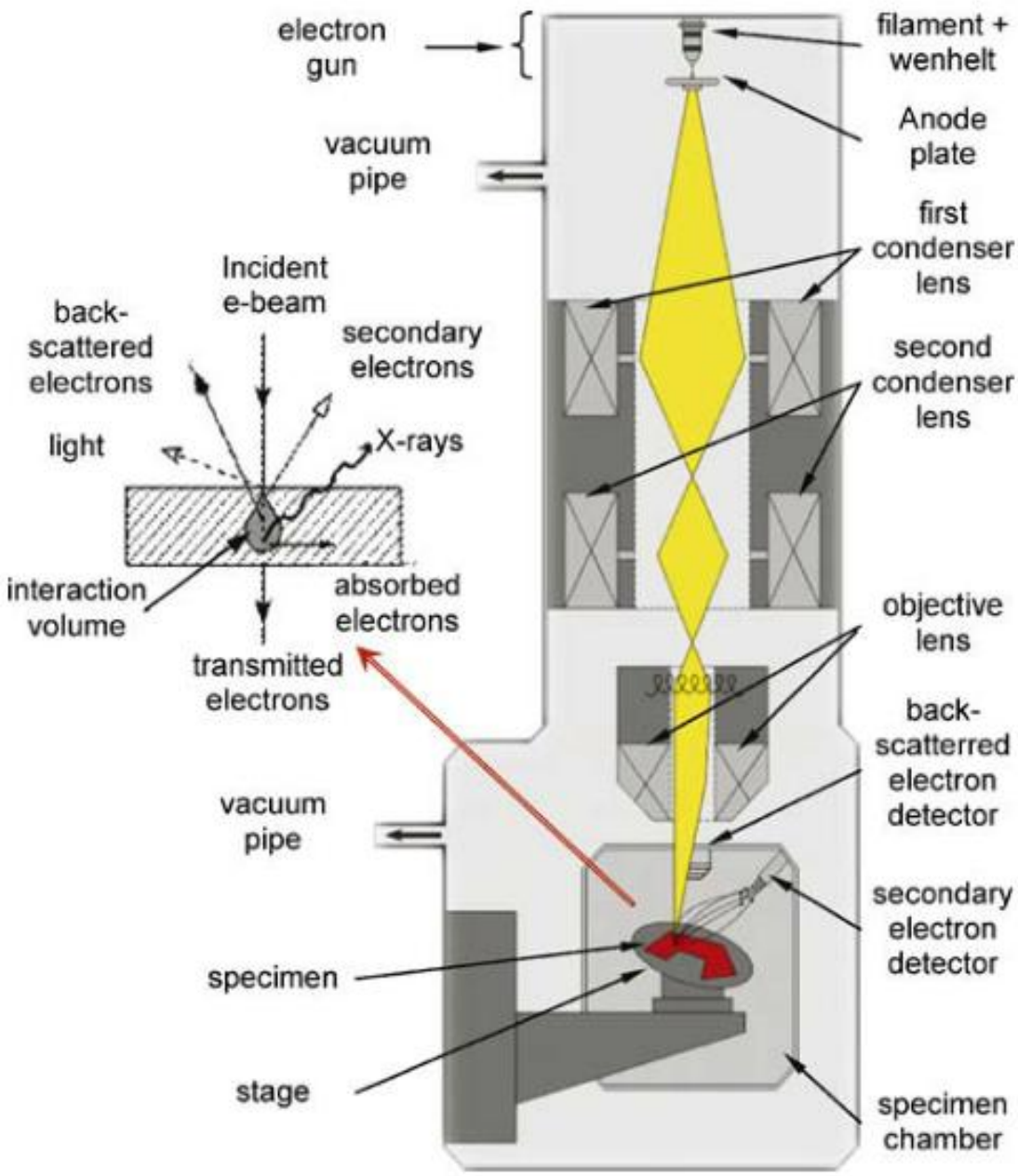

Figure 77: Structure of a scanning electron microscope [92]

An SEM has various operational parameters associated with imaging the specimen. A single line type scanning was employed by [92] who studied the parameters from three different SEMs. Table 9 lists the image parameters associated with the three SEMs for single line scans.

Table 9: SEM settings for single line scans

Imaging properties	FEI Quanta-200	FEI Quanta-200	JEOL JSM-6300	Hitachi S-4300
Magnification	200X	5,000X	5,000X	5,000X
Electron detector	BSE	BSE	BSE	BSE
Detector mode	Compositional	Compositional	Compositional	Compositional
Working distance (mm)	14	14	13	12.7
Vacuum mode	High vacuum	High vacuum	High vacuum	High vacuum
Accelerating voltage (kV)	30	30	10	20
E-beam spot size	3 (4 nm)	3 (4 nm)	13 (6 nm)	5 nm
Dwell time (μs)	100	100	153	100
Image size	1,024×884	1,024×884	1,024×768	1,280×960
Object magnification	1.25 μm/pixel	50 nm/pixel	50 nm/pixel	40 nm/pixel
Recording pixel shape	Square	Square	Square	Square
Image quantization (bits)	8	8	8	8

CALIBRATION: Images acquired in an SEM are affected by drift and spatial distortion. Two images of the specimen were obtained without any load applied with 300 s, 400 s, 600 s and 900 s time delay and various digital image sizes were used. Shifts were observed in the all of these images when the magnification used was 5,000X and 10,000X, however, such shifts were not seen in low magnification [92]. The drift in the acquired images greatly affect the strain maps obtained. Spatial distortion is caused by lens aberrations, misalignment of optical elements, non-parallelism between image plane and sensor plane, and lens curvature imperfections. [92]

To account for these distortions, parametric and non-parametric models of the SEM are implemented and the values of the parameters are computed from acquiring several images through time to account for the drift and know motions of the specimen for distortion. [92]

SURFACE PATTERNING: The micro patterning techniques employed by researchers mentioned in Table 7 can be implemented for SEM DIC. [1, 74, 76]. Sutton et al. in [92] use lithographically applied gold particles on an Al2024-t4 alloy.

MEMS LOADING DEVICE

Comb drive actuators are fabricated using single crystal reactive ion etching and metallization (SCREAM) process as mentioned in [90]. Thermal actuators are fabricated in a foundry with sensors and actuators arranged in a grid on a chip (Figure 78). Gold pads are used for electrical connects on the chip and the chip is glued to a ceramic pin grid. The gold pads are then connected to the leads in the ceramic cavity. [91]

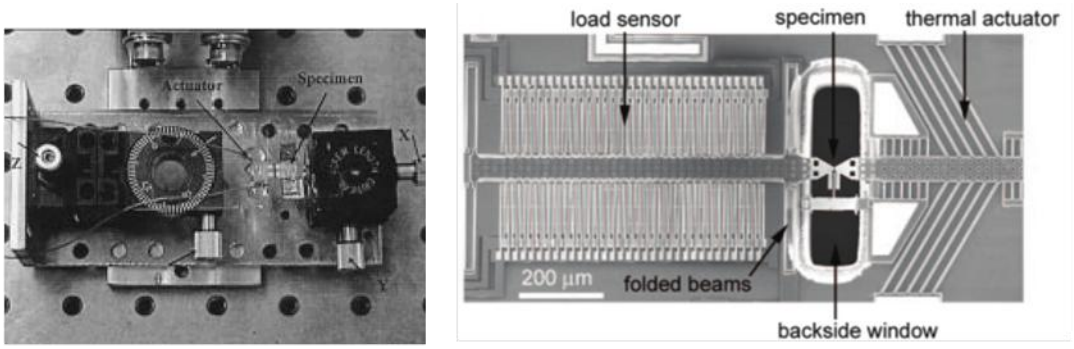

Figure 78: Micro load actuators; Left – SEM stage containing the comb drive actuators and the specimen [90]; Right – Thermal micro load cell sensor actuator system [91]

LOADING AND IMAGE ACQUISITION

Image acquisition for the purpose of strain measurement follows the same principles as mentioned in the previous chapters. The region of interest in picked on the visible surface in the viewport of the scanning electron microscope. A reference image is first acquired. For *in-situ* testing inside the SEM with a micro load machine, load controlled or displacement controlled loading is applied. Depending on this rate, an image acquisition rate is picked such that the small deformation assumptions hold good in two consequent images acquired. Once the images are acquired, image correlation algorithms are implemented to obtain displacement fields and further differentiation gives strain fields. This post processing approaches can be varied as seen in chapter 2.

6.4 APPROACH IN THIS WORK

An image series was acquired in-situ using a Scanning Electron Microscope while a steel specimen was being loaded in a micro tensile stage mounted inside the SEM in monotonic tension until failure. Images were simply recorded to observe the material with no previous intention of performing DIC.

The material in consideration was annealed 304L stainless steel in the form of a tensile test dog bone shaped sample. The gage dimensions are 1.67 mm (width) by 12 mm (length). At the gage section, the thickness was 1.68mm. The average grain diameter was 50 µm. diameter was 50 µm. The images were acquired as the specimen was being loaded until failure. No grain exposure or surface contrast techniques were applied to the material itself. Figure 79 shows the progression of material deformation.

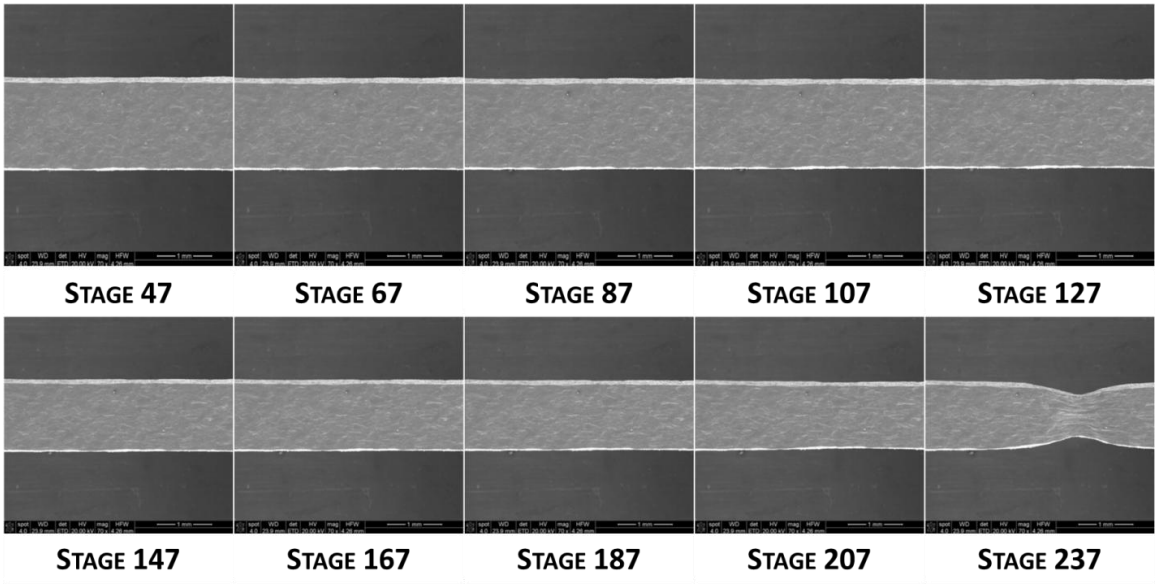

Figure 79: SEM images acquired in-situ for steel specimen loading

6.5 EX-SITU APPLICATION OF DIC

1022 x 940 pixel images acquired from the SEM were imported into the DIC software (ARAMIS). An attempt was made to correlate the grayscale values captured in the image series from the SEM and obtain strains. An area of 2.309 mm x 0.924 mm was observed on the specimen and thus the DIC measurement turned out to have a resolution of 3.71 µm/pixel. A subset field with 75 pixels and 10 pixel step was used. The 75 pixel subsets are used to capture sufficient information in every subset keeping in mind that the natural contrast of the material surface was used for correlation without any special patterning technique. A zoomed portion of the subset is shown in Figure 80.

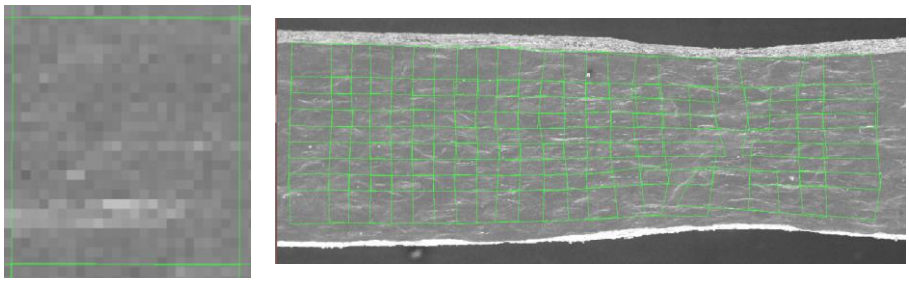

Figure 80: (left) 75 pixel facet; (right) subset field at necking

The 10 pixel step was used between the centers of adjacent subsets because the material undergoes necking and strains up to 50%. A closely spaced grid of subsets helps in keeping together the subset field even at high strains. The stretched subset field is shown in Figure 80. The convergence requirement for accuracy was set to 0.1 pixels.

6.6 RESULTS

Displacement and strain was successfully obtained from the image series. The strain gage at necking gave a reading of 50%. The strain mapping obtained from image correlation at necking was in good agreement with the strain gage of the tensile loading machine. Figure 81 shows a plot of the displacement at the onset of necking and Figure 82 shows the strains at the the necking zone.

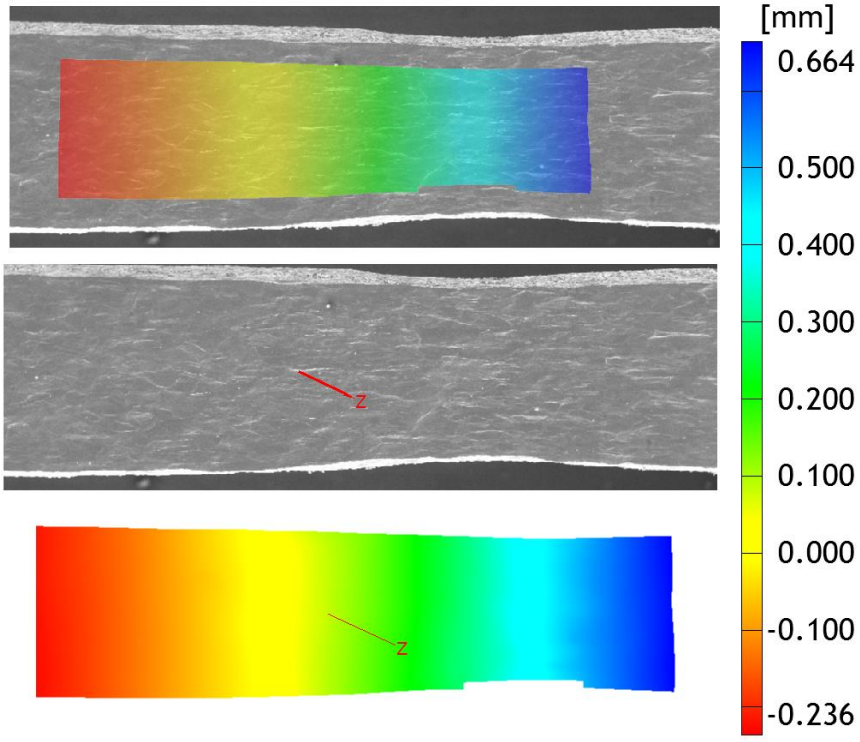

Figure 81: Full field DIC displacement mapping at onset of necking in specimen

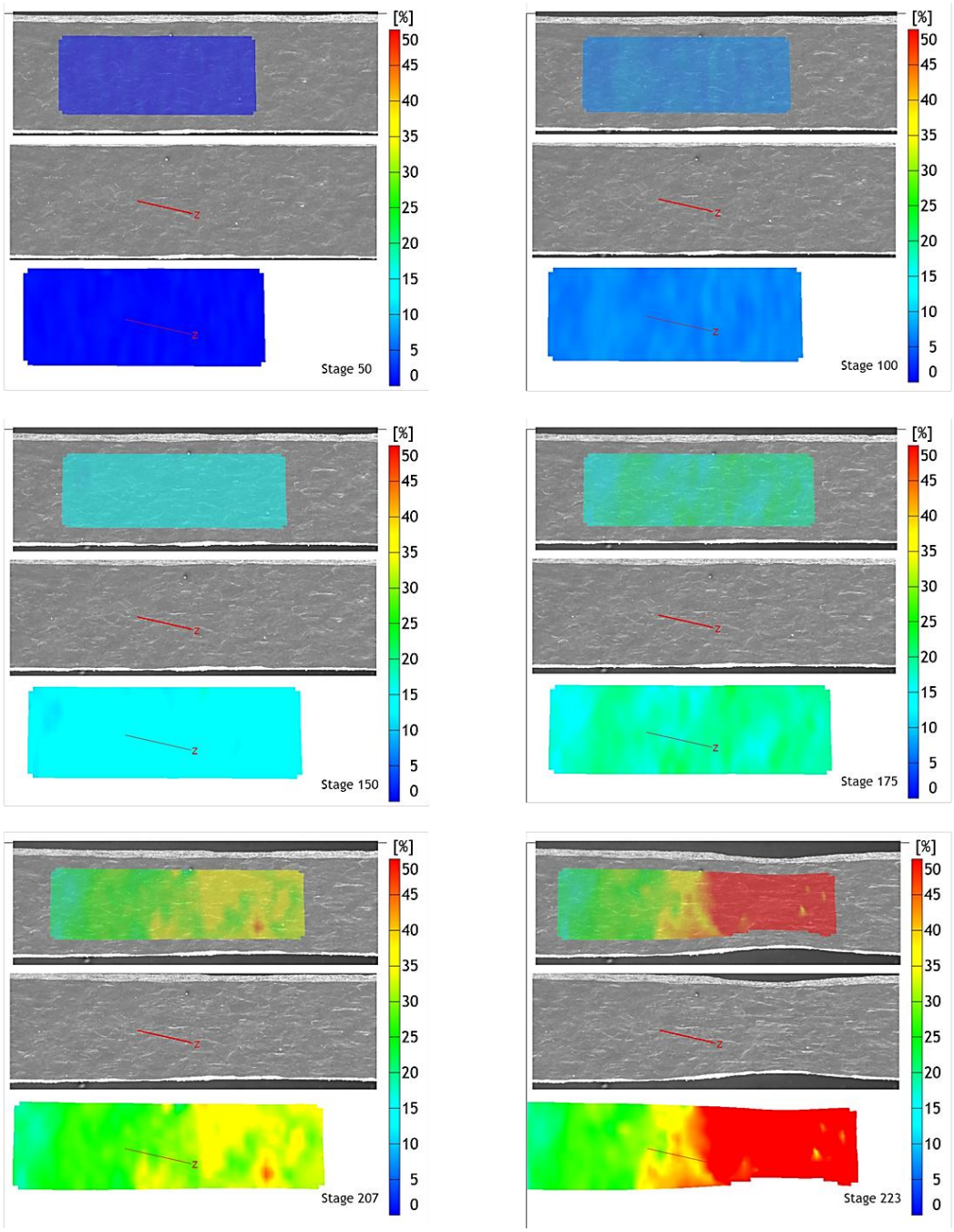

Figure 82: Evolution of strain on specimen

6.5 DISCUSSION

This approach of using the secondary electron images from a scanning electron microscope to determine strain has been used byTschopp et al. [1]. The in-situ SEM images they acquired were 16-bit 4096 x 3773 pixels covering a region of interest

equal to 274 x 230 μm^2. This gives a resolution of 0.066 µm/pixel. In DIC processing, they used square subsets of 99 pixels with a 5 pixel step. Laser irradiated Platinum nanoparticles for patterning the specimen. The effort in this chapter involves DIC using SEM images at a resolution of 3.71 µm/pixel. There is a huge gap in the resolutions of the two measurements. However, the correlation was performed here was without any patterning applied and makes use of the natural contrast of the specimen. In both cases, the grain boundaries were not exposed. In the work by Tschopp et al. however, the strains obtained from DIC are correlated visually with EBSD maps from the same region of interest.

An extremely obvious next step in SEM DIC method is to expose grain structure in the material such that the grain boundaries are distinctly visible in the in-situ images acquired when the material is tested. Therefore, strain evolution associated with a particular grain in the chosen field of view could be directly tracked *in-situ*.

CHAPTER 7: CONCLUSIONS AND FUTURE WORK

In this thesis, three approaches to perform grain scale measurements using Digital image Correlation have been put forth:

1. A commercially available Digital Image Correlation system was adapted to become capable of achieving grain-scale strain measurements in polycrystalline metals using only off-the-shelf products.

2. A long distance microscope was used with a commercial DIC system for *in-situ* grain strain measurements. This setup can be used directly when applying mechanical loads using a conventional servo-hydraulic testing frame and therefore its advantage is that it can be used to test material specimen that adhere to ASTM standards.

3. images acquired during testing with a mechanical loading stage inside a Scanning Electron Microscope were used *ex-situ* by the available DIC software to quantify strains on the materials surface without relying to any special surface patterning method.

The three methods mentioned above demonstrated the unique capabilities of DIC to perform accurate and repeatable measurements of deformation and strain at the grain-scale typically requiring fields of view in the order of a few millimeters. It should be noted here as well that all three methods described in this thesis have room for further advancement in terms of both robustness and reliability. Specifically, more thorough research needs to be done in the direct adaptation of the commercial DIC system using extension tubes. In particular, the precise amount of etching that is needed must be determined to allow for direct grain-scale measurements. In addition, the procedure to choose a light source also needs to be more systematically addressed, given that a single source of high intensity diffused light source might enhance reliability of such measurements. However, the application of this method will still be fairly limited in terms of grain size since only grains of size comparable to the field of view can be monitored with this approach.

Another alternative that would bypass the shortcomings of the simple adaptation discussed in chapter 4 is the use of a digital microscopic imaging system equipped with six degrees of freedom. In this context, the method presented in chapter 5 offered valuable feedback. Specifically, the K2 lens, which is a long distance microscopy system, was used to monitor small fields of view (in the range of 2mm to ~0.5mm) and proved free of spatial distortions. In this thesis, the K2 lens was mounted onto a 5 megapixel camera to monitor the microstructure behavior at the tip of a propagating crack. The specimen itself was loaded using a conventional macroscale loading frame. However, there was a trade off in monitoring strains at the tip of a

crack that had been created using fatigue loading while observing directly grains. As a result, loading had to be held multiple times through the test to adjust the field of view of the microscope to see the crack tip in the chosen field of view. This procedure, however, is possible to cause relaxation and creep effects. In addition moving manually the lens system is not desirable grain-scale measurements using an optical lens are sensitive to small vibrations that can cause false strains readings. These shortcomings can be circumvented by the use of motor driven motion actuators that could move the microscope sufficiently fast to allow monitoring the tip of the crack in a given region of interest. This procedure would require customized scripts that control the application of the K2 lens and motor actuators. In addition, ways to automatically adjust the focus of the system would have to be found for more efficient monitoring. In this context, self-focus modules [88] can be utilized within the K2 lens, such that it automatically keeps the region being monitored in sharp focus. Moreover, stabilization modules are recommended such that the lens-camera system becomes more insensitive to mechanical vibrations.

Grains in polycrystalline materials are generally in the order of a few millimeters to nanometers. Observing material in this length scale is the strength of electron microscopes. With this foundation, Chapter 6 shows how an image series acquired from *in-situ* SEM loading of a stainless steel specimen is used as stages for DIC post-processing. A micro tensile stage was used inside an SEM to perform loading and the strains computed using DIC at necking were accurately matched with the strain measured from the strain gage of the micro load cell. The SEM line of approach gives rise to new possibilities. Sutton et al. [92] in their detailed review of SEM DIC provide the methods for calibrating an SEM to account for distortion effects at high magnification. This leads to applicability of DIC at various magnifications with great accuracy.

As discussed in chapter 6, a scanning electron microscope has two kinds of detectors including secondary electron and back scattered electron detectors. An SEM system equipped with both kinds of detectors could offer a great solution to track strain evolution in microstructures and observe grain-scale changes at the same time. In this setup, the secondary electron images could provide the necessary images for performing digital image correlation at the grain-scale, while the backscattered electron beams could record information related to grain orientation. Effective integration of these two modules in a monitoring system that simultaneously monitors *in-situ* strain evolution and grain orientation combined with the use of micro tensile stage mounted within the SEM chamber can prove to powerful and promising method for addressing important issues related to deformation and failure of materials.

LIST OF REFERENCES

1. Tschopp, M.a., et al., *Microstructure-Dependent Local Strain Behavior in Polycrystals through In-Situ Scanning Electron Microscope Tensile Experiments.* Metallurgical and Materials Transactions A, 2009. **40**(10): p. 2363-2368.

2. Callister, W.D. and D.G. Rethwisch, *Fundamentals of materials science and engineering: an integrated approach*2011: Wiley.

3. Ritchie, R. and A. Thompson, *On macroscopic and microscopic analyses for crack initiation and crack growth toughness in ductile alloys.* Metallurgical and Materials Transactions A, 1985. **16**(1): p. 233-248.

4. Peirce, D., R.J. Asaro, and A. Needleman, *Material rate dependence and localized deformation in crystalline solids.* Acta Metallurgica, 1983. **31**(12): p. 1951-1976.

5. Choi, S.H., et al., *3-D simulation of spatial stress distribution in an AZ31 Mg alloy sheet under in-plane compression.* International Journal of Plasticity, 2011. **27**(10): p. 1702-1720.

6. Carroll, J., et al., *An experimental methodology to relate local strain to microstructural texture.* The Review of scientific instruments, 2010. **81**(8): p. 083703-083703.

7. Cofaru, C., W. Philips, and W. Van Paepegem, *A novel speckle pattern—Adaptive digital image correlation approach with robust strain calculation.* Optics and Lasers in Engineering, 2012. **50**(2): p. 187-198.

8. Sutton, M., et al., *Determination of displacements using an improved digital correlation method.* Image and Vision Computing, 1983. **1**(3): p. 133-139.

9. Chu, T.C., et al., *Applications of digital-image-correlation techniques to experimental mechanics.* Experimental mechanics, 1985(September): p. 232-244.

10. Sutton, M.A., J.J. Orteu, and H.W. Schreier, *Image Correlation for Shape, Motion and Deformation Measurements: Basic Concepts, Theory and Applications*2009: Springer.

11. Gates, M., J. Lambros, and M.T. Heath, *Towards High Performance Digital Volume Correlation.* Experimental Mechanics, 2010. **51**(4): p. 491-507.

12. Hung, P.C. and A.S. Voloshin, *In-plane strain measurement by digital image correlation.* Journal of the Brazilian Society of Mechanical Sciences and Engineering, 2003. **25**(3): p. 215-221.

13. Pan, B., et al., *Two-dimensional digital image correlation for in-plane displacement and strain measurement: a review.* Measurement Science and Technology, 2009. **20**(6): p. 062001-062001.

14. Lu, H. and P.D. Cary, *Deformation measurements by digital image correlation: Implementation of a second-order displacement gradient.* Experimental Mechanics, 2000. **40**(4): p. 393-400.

15. Chu, T.C. and W.F. Ranson, *Applications of digital-image-correlation techniques to experimental mechanics.* Experimental Mechanics, 1985(September): p. 232-244.

16. Luo, P., et al., *Accurate measurement of three-dimensional deformations in deformable and rigid bodies using computer vision.* Experimental Mechanics, 1993. **33**(2): p. 123-132.

17. Garcia, D. and J.J. Orteu, *Accurate calibration of a stereovision sensor: comparison of different approaches.* 5th Workshop on Vision Modeling, 2000.

18. Orteu, J.J., *3-D computer vision in experimental mechanics.* Optics and Lasers in Engineering, 2009.

19. Garcia, D., J.J. Orteu, and M. Devy. *Accurate calibration of a stereovision sensor: comparison of different approaches*. 2000.

20. Hartley, R.I. and P. Sturm, *Triangulation.* Computer vision and image understanding, 1997. **68**(2): p. 146-157.

21. Schreier, H.W., *Advances in Light Microscope Stereo Vision.* Experimental Mechanics, 2004. **44**(3): p. 278-288.

22. Litwiller, D., *CCD vs. CMOS.* Photonics Spectra, 2001.

23. Schmidt, T.E., et al. *Full-field dynamic deformation and strain measurements using high-speed digital cameras*. 2005.

24. GOM-mbH, *ARAMIS User Information - Hardware*, GOM-mbH, Editor 2011, GOM-mbH: Braunschweig, Germany.

25. Jonnalagadda, K.N., et al., *Experimental Investigation of Strain Rate Dependence of Nanocrystalline Pt Films.* Experimental Mechanics, 2009. **50**(1): p. 25-35.

26. Pan, B., Z. Lu, and H. Xie, *Mean intensity gradient: an effective global parameter for quality assessment of the speckle patterns used in digital image correlation.* Optics and Lasers in Engineering, 2010. **48**(4): p. 469-477.

27. Triconnet, K., et al., *Parameter choice for optimized digital image correlation.* Optics and Lasers in Engineering, 2009. **47**(6): p. 728-737.

28. Pan, B., *Recent Progress in Digital Image Correlation.* Experimental Mechanics, 2010. **51**(7): p. 1223-1235.

29. Pan, B., et al., *Study on subset size selection in digital image correlation for speckle patterns.* Optics express, 2008. **16**(10): p. 7037-48.

30. GOM-mbH, *ARAMIS User Manual - Software*, GOM-mbH, Editor 2009, GOM-mbH: Braunschweig, Germany.

31. Lecompte, D., et al., *Quality assessment of speckle patterns for digital image correlation.* Optics and Lasers in Engineering, 2006. **44**(11): p. 1132-1145.

32. Pan, B., Z. Wang, and Z. Lu, *Genuine full-field deformation measurement of an object with complex shape using reliability-guided digital image correlation.* Optics express, 2010. **18**(2): p. 1011-23.

33. Zhang, J., et al., *On the use of the digital image correlation method for heterogeneous deformation measurement of porous solids.* Optics and Lasers in Engineering, 2011. **49**(2): p. 200-209.

34. Shen, B. and G.H. Paulino, *Direct Extraction of Cohesive Fracture Properties from Digital Image Correlation: A Hybrid Inverse Technique.* Experimental Mechanics, 2010. **51**(2): p. 143-163.

35. Sun, Y., et al., *Finite element formulation for a digital image correlation method.* Applied optics, 2005. **44**(34): p. 7357-7363.

36. Vendroux, G., *Submicron deformation field measurements: Part 2. Improved digital image correlation.* Experimental Mechanics, 1998.

37. Schreier, H. and M.A. Sutton, *Systematic Errors in Digital Image Correlation Due to Undermatched Subset Shape Functions.* Experimental Mechanics, 2002. **42**(3): p. 303-310.

38. Pan, B., H. Xie, and Z. Wang, *Equivalence of digital image correlation criteria for pattern matching.* Applied optics, 2010. **49**(28): p. 5501-9.

39. Cofaru, C., W. Philips, and W. Van Paepegem, *Improved Newton-Raphson digital image correlation method for full-field displacement and strain calculation.* Applied optics, 2010. **49**(33): p. 6472-84.

40. Bing, P., et al., *Performance of sub-pixel registration algorithms in digital image correlation.* Measurement Science and Technology, 2006. **17**(6): p. 1615-1621.

41. Schreier, H.W., J.R. Braasch, and M.A. Sutton, *Systematic errors in digital image correlation caused by intensity interpolation.* Optical Engineering, 2000. **39**: p. 2915-2915.

42. Luu, L., et al., *Accuracy enhancement of digital image correlation with B-spline interpolation.* Optics letters, 2011. **36**(16): p. 3070-2.

43. Bruck, H., et al., *Digital image correlation using Newton-Raphson method of partial differential correction.* Experimental Mechanics, 1989. **29**(3): p. 261-267.

44. Zhou, P. and K.E. Goodson, *Subpixel displacement and deformation gradient measurement using digital image/speckle correlation (DISC).* Optical Engineering, 2001. **40**(8): p. 1613-1613.

45. Xiong, L., et al., *Evaluation of sub-pixel displacement measurement algorithms in digital image correlation.* 2011 International Conference on Mechatronic Science, Electric Engineering and Computer (MEC), 2011: p. 1066-1069.

46. Meng, L.B., G.C. Jin, and X.F. Yao, *Application of iteration and finite element smoothing technique for displacement and strain measurement of digital speckle correlation.* Optics and Lasers in Engineering, 2007. **45**(1): p. 57-63.

47. Pitter, M., C.W. See, and M. Somekh, *Subpixel microscopic deformation analysis using correlation and artificial neural networks.* Opt. Express, 2001. **8**(6): p. 322-327.

48. Pilch, A., A. Mahajan, and T. Chu, *Measurement of whole-field surface displacements and strain using a genetic algorithm based intelligent image correlation method.* Journal of Dynamic Systems, Measurement, and Control, 2004. **126**: p. 479.

49. Lin, Y. and Z. Lan. *Sub-pixel displacement measurement in Digital Image Correlation using Particle Swarm Optimization*. 2010. IEEE.

50. Hild, F., *Digital Image Correlation : from Displacement Measurement to Identification of Elastic Properties – a Review.* Strain, 2006: p. 69-80.

51. Chen, D.J., et al., *Digital speckle-displacement measurement using a complex spectrum method.* Appl. Opt., 1993. **32**(11): p. 1839-1849.

52. Molimard, J., *Implementation of the direct evaluation of strains using a phase analysis code for random patterns.* Optics and Lasers in Engineering, 2011. **49**(9-10): p. 1194-1200.

53. Su, C. and L. Anand, *A new digital image correlation algorithm for whole-field displacement measurement.* 2003.

54. Cheng, P., et al., *Full-field Speckle Pattern Image Correlation with B-Spline Deformation Function.* Experimental Mechanics, 2002. **42**(September).

55. Besnard, G., F. Hild, and S. Roux, *"Finite-Element" Displacement Fields Analysis from Digital Images: Application to Portevin–Le Châtelier Bands.* Experimental Mechanics, 2006. **46**(6): p. 789-803.

56. Rastogi, P., *Principles of holographic interferometry and speckle metrology.* Photomechanics, 2000: p. 103-151.

57. Jacquot, P., *Speckle Interferometry: A Review of the Principal Methods in Use for Experimental Mechanics Applications.* Strain, 2008. **44**(1): p. 57-69.

58. Gerasimov, S. and V. Zhilkin, *Strain analysis of polycrystalline specimens by the method of superimposed holographic interferometry.* Journal of Applied Mechanics and Technical Physics, 2000. **41**(1): p. 200-204.

59. Sciammarella, C., *The moiré method—A review.* Experimental Mechanics, 1982. **22**(11): p. 418-433.

60. Bastawros, A.F. and K.S. Kim, *Experimental analysis of near-crack-tip plastic flow and deformation characteristics (I): Polycrystalline aluminum.* Journal of the Mechanics and Physics of Solids, 2000. **48**(1): p. 67-98.

61. Guo, Z., et al., *Study on Deformation of Polycrystalline Aluminum Alloy Using Moiré Interferometry.* Experimental Mechanics, 2006. **46**(6): p. 699-711.

62. Birkholz, M., P.F. Fewster, and C. Genzel, *Thin film analysis by X-ray scattering*2006: Vch Verlagsgesellschaft Mbh.

63. Maire, E., et al., *On the application of X-ray microtomography in the field of materials science.* Advanced Engineering Materials, 2001. **3**(8): p. 539-546.

64. Oddershede, J., et al., *Measuring the stress field around an evolving crack in tensile deformed Mg AZ31 using three-dimensional X-ray diffraction.* Acta Materialia, 2012. **60**(8): p. 3570-3580.

65. Ganguly, S., M.E. Fitzpatrick, and L. Edwards, *Use of Neutron and Synchrotron X-Ray Diffraction for Evaluation of Residual Stresses in a 2024-T351 Aluminum Alloy Variable-Polarity Plasma-Arc Weld.* Metallurgical and Materials Transactions, 2006. **37A**(2): p. 411-420.

66. Hutchings, M.T. and A.D. Krawitz, *Measurement of residual and applied stress using neutron diffraction*1992: Springer.

67. Agnew, S., et al., *Study of slip mechanisms in a magnesium alloy by neutron diffraction and modeling.* Scripta Materialia, 2003. **48**(8): p. 1003-1008.

68. Stojakovic, D., *Electron backscatter diffraction in materials characterization.* Processing and Application of Ceramics, 2012. **6**.

69. Wilkinson, A.J., G. Meaden, and D.J. Dingley, *High-resolution elastic strain measurement from electron backscatter diffraction patterns: New levels of sensitivity.* Ultramicroscopy, 2006. **106**(4–5): p. 307-313.

70. Kamaya, M., A.J. Wilkinson, and J.M. Titchmarsh, *Measurement of plastic strain of polycrystalline material by electron backscatter diffraction.* Nuclear engineering and design, 2005. **235**(6): p. 713-725.

71. Badulescu, C., et al., *Applying the grid method and infrared thermography to investigate plastic deformation in aluminium multicrystal.* Mechanics of Materials, 2011. **43**(1): p. 36-53.

72. Zhu, G., et al., *Deformation inhomogeneity in large-grained AA5754 sheets.* Materials Science and Engineering: A, 2011. **528**(12): p. 4187-4198.

73. Niendorf, T., et al., *Monitoring the fatigue-induced damage evolution in ultrafine-grained interstitial-free steel utilizing digital image correlation.* Materials Science and Engineering: A, 2009. **517**(1-2): p. 225-234.

74. Jin, H., et al., *Microscale characterization of granular deformation near a crack tip.* Journal of Materials Science, 2011. **46**(20): p. 6596-6602.

75. Abuzaid, W.Z., et al., *Slip transfer and plastic strain accumulation across grain boundaries in Hastelloy X.* Journal of the Mechanics and Physics of Solids, 2012. **60**(6): p. 1201-1220.

76. Rehrl, C., et al., *A methodology to study crystal plasticity inside a compression test sample based on image correlation and EBSD.* Materials Characterization, 2011. **62**(8): p. 793-800.

77. Padilla, H.A., et al., *Relating inhomogeneous deformation to local texture in zirconium through grain-scale digital image correlation strain mapping experiments.* International Journal of Solids and Structures, 2012. **49**(1): p. 18-31.

78. Ahn, B. and S.R. Nutt, *Strain Mapping of Al–Mg Alloy with Multi-scale Grain Structure using Digital Image Correlation Method.* Experimental Mechanics, 2009. **50**(1): p. 117-123.

79. Bartali, A.E., V. Aubin, and S. Degallaix, *Surface observation and measurement techniques to study the fatigue damage micromechanisms in a duplex stainless steel.* International Journal of Fatigue, 2009. **31**(11-12): p. 2049-2055.

80. El Bartali, A., et al., *Strain heterogeneities between phases in a duplex stainless steel. Comparison between measures and simulation.* Procedia Engineering, 2010. **2**(1): p. 2229-2237.

81. Renard, K., S. Ryelandt, and P.J. Jacques, *Characterisation of the Portevin-Le Châtelier effect affecting an austenitic TWIP steel based on digital image correlation.* Materials Science and Engineering: A, 2010. **527**(12): p. 2969-2977.

82. Lei, D., F. Hou, and X. Gong, *Investigation of Deformation at the Grain Scale in Polycrystalline Materials by Coupling Digital Image Correlation and Digital Microscopy.* Experimental Techniques, 2012. **36**(2): p. 24-31.

83. Hokka, M., et al., *Characterization of the mechanical behavior of ultrafinegrained metals using digital image correlation.* EPJ Web of Conferences, 2010. **6**: p. 05005-05005.

84. Efstathiou, C., H. Sehitoglu, and J. Lambros, *Multiscale strain measurements of plastically deforming polycrystalline titanium: Role of deformation heterogeneities.* International Journal of Plasticity, 2010. **26**(1): p. 93-106.

85. Korsunsky, A.M., M. Sebastiani, and E. Bemporad, *Residual stress evaluation at the micrometer scale: Analysis of thin coatings by FIB milling and digital image correlation.* Surface and Coatings Technology, 2010. **205**(7): p. 2393-2403.

86. Mordike, B.L. and T. Ebert, *Magnesium: Properties — applications — potential.* Materials Science and Engineering: A, 2001. **302**(1): p. 37-45.

87. Bettles, C. and M. Gibson, *Current wrought magnesium alloys: strengths and weaknesses.* JOM Journal of the Minerals, Metals and Materials Society, 2005. **57**(5): p. 46-49.

88. Infinity, *Model K2/SC Long-Distance Microscope System*, 2009, Infinity Photo-Optical Company: Colorado, USA.

89. Song, H.W., et al., *Fracture mechanisms and size effects of brittle metallic foams: in situ compression tests inside SEM.* Composites Science and Technology, 2008. **68**(12): p. 2441-2450.

90. Haque, M. and M. Saif, *Microscale materials testing using MEMS actuators.* Microelectromechanical Systems, Journal of, 2001. **10**(1): p. 146-152.

91. Zhu, Y. and H.D. Espinosa, *An electromechanical material testing system for in situ electron microscopy and applications.* Proceedings of the National Academy of Sciences of the United States of America, 2005. **102**(41): p. 14503.

92. Sutton, M., et al., *Scanning electron microscopy for quantitative small and large deformation measurements Part I: SEM imaging at magnifications from 200 to 10,000.* Experimental Mechanics, 2007. **47**(6): p. 775-787.

93. Sutton, M., et al., *Scanning electron microscopy for quantitative small and large deformation measurements Part II: experimental validation for magnifications from 200 to 10,000.* Experimental Mechanics, 2007. **47**(6): p. 789-804.

ADDENDUM

The author would like to thank Professor M. Taheri and her graduate student Mr. Christopher Barr from the Materials Science and Engineering Department at Drexel University for providing a video from which the images shown in Figure 79 were extracted to perform the ex situ DIC approach described in section 6.5.